Characterization of metal-carbon containing species using a mass-selective multiphoton ionization technique

Inauguraldissertation

zur Erlangung der Würde eines Doktors der Philosophie vorgelegt der
Philosophisch-Naturwissenschaftlichen Fakultät der Universität Basel

vorgelegt von

Cristina Apetrei Bîrză
aus Onești, Rumänien

Basel, 2009

Genehmigt von der Philosophisch-Naturwissenschaftlichen Fakultät

auf Antrag von

Prof. Dr. J. P. Maier und Prof. Dr. Stefan Willitsch

Basel, den 15.09.2009

Prof. Dr. Eberhard Parlow

Dekan

Dedicated to my family and Petre

Do not go where the path may lead; go instead where there is no path and leave a trail.

Ralph Waldo Emerson

Acknowledgements

This research project would not have been possible without the support of many people. I would like to thank Prof. John P. Maier for giving me the opportunity to perform my PhD study in his group in the frame of a Marie Curie Fellowship. His supervision and guidance are greatly appreciated. I would also like to thank Prof. Stefan Willitsch for his courteously agreement to act as co-referee and his advices during the last months of my PhD.

I would like to express my gratitude to Prof. Alan Knight for the great collaboration we had, the good times spent in the lab and for being always there whenever I asked for an advice.

The completion of this PhD would have not been possible without the people that believed in me and introduced me in this field of molecular spectroscopy. My special thanks goes to Dr. Petre Birza for his help, guidance and continuous support from my first day in the group. I owe a great deal of appreciation to Prof. Hongbin Ding for sharing his experience about the experiment and other scientific topics.

I am grateful to my colleagues and good friends, Dr. Zohra Guennoun and Dr. Corey Rice for their support, guidance and advices. The time devoted to my questions and your willingness to share your knowledge with me are greatly appreciated. I really enjoyed the good moments we had discussing about science and not only. I hope the time and circumstances will not make us grow apart.

I can not forget Dr. Evan Jochnowitz and Dr. Ramya Nagarajan with whom I had the pleasure of discussing and working with. The other groups members, past and present, have always been a source of fruitful discussions and enjoyable times.

Many people in the house made my PhD work and life easier by solving the technical problems and helping with the bureaucratic matters. Dieter Wild and Grischa Martin from the mechanical workshop are thanked for their wonderful skills in constructing technical devices; Georg Holderied is thanked for his great help with the electronics;

Jacques Lecoultre is thanked for synthesizing the necessary chemicals; Esther Stalder and Daniela Tischhauser are thanked for taking care of the administrative issues. Thank you for your time and patience.

Two great persons, Dr. Camelia Draghici and Dr. Cornelia Palivan are thanked for believing and trusting me, for their advices and continuous support through the hard times during my studies.

In the end, I would like to express my gratitude to my beloved parents and brothers, for their understanding, endless support, affection and encouragement through the duration of my studies. As vrea sa multumesc parintilor si fratilor mei pentru afectiunea si sprjinul continuu fara de care nu as fi ajuns astazi, cu succes, la finalul acestui doctorat. Multe, multe multumiri!

The Swiss National Science Foundation, Molecular Universe Research Training Program and the City of Basel are thanked for their financial support.

Basel, Switzerland

15 September 2009 Cristina Apetrei Birza

Contents

1 Introduction

The role of metal-containing molecules in chemistry is remarkable. In areas ranging from catalysis to biochemistry, atmospheric to interstellar chemistry, combustion to metal-organic vapor deposition, metal-ligand bonds are formed and broken. Understanding the metal-ligand (M-L, L=CN, OH, CCH, CH_3, C_2H_5) bond and its properties is very important and the basis in many areas of chemistry.

The most common means of probing the metal-ligand bond is through detailed quantum-chemical calculations. Nowadays the methodology is highly developed and a virtually complete picture can be obtained. The equilibrium bond length, the bond dissociation energy, the bond force constant, the charge distribution and the effect of electronic excitation all can be possibly extracted from these calculations. Taking into account the high electron count for metal atoms, the small separation of metal atomic orbitals leading to many near-degeneracies, highly correlated calculations are desirable making *ab initio* calculations for metal-containing species not a trivial task. The simplest consist of a single metal atom bound to a single attached molecule, the ligand. However, although simple from a theoretical point of view, the study of such entities represent a big challenge to experimentalist because for most of the metals, attaching a single univalent ligand results in a highly reactive species that has only a transient existence in the condensed phase.

To reduce their reaction rate to a negligible level a possible solution is to trap these molecules in rare-gas matrices. The low temperature and rigid environment, characteristic of such matrices, provide a semi-ideal yet effective means for the isolation and study of highly reactive species. However, a drawback of the matrix isolation technique is that the inflexible trapping site tends to quench any rotational motion, thus ruling out rotationally resolved spectroscopy leading to poor structural information. Nevertheless, the infrared (IR) and Raman spectra of matrix isolated molecules[1] have been of a great help and tend to compare with the spectra of the same species in the gas phase. In contrast, the electronic spectra are usually severely perturbed by the surrounding host lattice.

The ideal environment to study reactive intermediates is in the gas phase. Over the years, the exquisite sensitivity of mass spectrometry based techniques has been utilized to study the interaction of metals with organic and inorganic molecules. Most of this gas phase work involves ions.[2] The techniques used include traditional high-pressure mass spectrometry,[3] flowing afterglows,[4] ion beams,[5] and Fourier transform ion cyclotron resonance.[6] While these methods are the benchmark of the gas-phase studies, in order to obtain elaborate structural information different techniques are required to investigate the electronic spectra of such species. Nevertheless, producing metal containing intermediates in the gas phase has been a challenging issue. The most commonly used method for making free radicals in the gas phase involves fragmentation of a precursor molecule, normally by photolysis or by an electrical discharge. Unfortunately, these techniques have limited utility in the production of metal-carbon radicals, since suitable volatile precursors do not usually exist.

Most of the early work on metal containing radicals was carried out using Broida-type oven source,[7] metal atoms being produced by evaporation from a heated crucible and entrained in a flow of inert carrier gas. This source has been extensively employed in the millimeter-wave techniques to obtain pure rotational spectra. Species such as alkali and alkaline earth monohydroxides, monoacetylides and monomethyls have been identified and characterized in their ground electronic states.[8–16] In this type of source the temperature remains a serious disadvantage in many cases. At best rotational temperature of 400 K is attained with a Broida oven, and the vibrational temperature is often considerably higher on account of the much lower efficiency for the collisional cooling of vibrational degrees of freedom.

To eliminate such a problem, supersonic cooling is necessary. The developments in supersonic jet expansion technology have made areas like molecular spectroscopy to advance rapidly. Supersonic nozzles can be combined with hot oven evaporation upstream of the nozzle, but the technology is quite difficult to implement and these sources have not seen widespread use.[17,18] More common, and of more general use, are pulsed ablation sources, developed almost simultaneously by Smalley *et al.*[19] and Bondybey *et al.*[20] in the early 1980s. Using this source, metal containing molecules with rotational temperatures below 50 K are frequently obtained. It is important to admit that laser ablation is rarely a clean source of a particular species. A multitude of processes can take place in the laser ablation region. In addition to metal atoms which can be formed in both their ground and their excited states, metal clusters and metal ions can also be generated. The bombardment by intense laser radiation, and the subsequent production of light, heat and a whole host of charged particle within the ablation plasma, can lead to extensive fragmentation of molecular precursors. Laser ablation source has been extensively used in conjunction with the laser induced fluorescence (LIF) spectrometer.[21–26] A drawback of the LIF rechnique is the lack of species discrimination. This can be overcome using a mass-selective technique such as resonant-enhanced multiphoton ionization (REMPI). The implementation of the laser ablation source in the REMPI spectrometer will be described in the Experimental section.

1.1 Metal-containing carbon chains and their terrestrial applications

Metal complexes with conjugated hydrocarbon bridges (double and triple bonds) or with donor and acceptor ligands are candidates for electrically conducting materials and for materials with second- and third- nonlinear optical properties. These compounds are also interesting as model systems for surface carbides in heterogeneous catalysis.[27–29] They are models for intermediates in the polymerization process of alkenes and alkynes,[30] and for unsaturated hydrocarbons chemisorbed on metal surfaces[31] - a first step during heterogenous catalysis.

Hydrocarbon on metals are of practical importance in surface chemistry. The first experiments were performed on metallic particles generally supported on oxides, materials used in catalytic reactions. Nevertheless, the shape of the metallic aggregates studied is of tremendous importance and it was difficult and tedious requirement to bring under control the surface structure on atomic scale. Moreover, the electronic properties of metal may in such cases be modified by interactions with the support. The purpose of studying hydrocarbon absorption on metals is to determine the chemical nature, the location relative to the surface, and the geometry of the adsorbed species, which reflects the hybridization of carbon atoms. This would enable to obtain a fundamental understanding of the different properties of different metal substrates with varied exposed sites and their relative properties towards breaking or rearrangement of C-C and C-H bonds.

Different techniques have been employed to study such interactions. The contribution of infrared spectroscopy[32–34] because of the relative ease with which infrared spectra can be monitored for all states of matter. From vibrational energies, force constants can be determined and in this way additional information regarding the bond strengths iwithin the adsorbate or that with respect to the substrate can be obtained. Following the recent progress in ultrahigh-vacuum techniques allowing experiments to be conducted over a long time with controlled atmospheres and surfaces, recent years have seen a great development in the electronic and geometrical structure determination of hydrocarbon-metal systems.

Convenient understanding of adsorption process requires some information about the electronic properties of the adsorbate-substrate pair. Spectral information on the orbitals of adsorbed species may be obtained using photoelectron spectroscopy. Despite the general similarities in the relative ionization levels of chemisorbed hydrocarbons and their gas-phase counterparts,[35] the latter would provide a better understanding of the metal-carbon bonding properties. Because of the large differences in the behavior of bare metals with respect to their reactivity towards C-H or C-C bond breaking, the gas-phase studies including electronic spectroscopy, reaction kinetics and dynamics, would give an insight into the formation of metal-carbon bonds, accurate ionization potentials, electron affinities, bond dissociation energies and branching ratios. The applicability of these results is not only for understanding the heterogeneous catalytic processes but also are of tremendous importance from a fundamental point of view.

The simplest molecular unit of carbon, C_2, existing as a small part of the linear polyenes [-$(C\equiv C)_n$-] (also named "carbynes"), is extremely reactive and has only been characterized by spectroscopic methods. One method of stabilizing the C_2 unit is by end-capping through the derivatization of both ends forming organic acetylenes, acetylide complexes or acetylide bridges between two metal centers. In organometallic polymers, unsaturated hydrocarbons, C_n units, can act as electronic bridges[36] ("molecular wires"[37]) between metal atoms.

The ultimate computational system would consist of logic devices that are ultra dense, ultra fast, and molecular-sized.[38,39] Even though state-of-the-art nanopattering techniques allow lithographic probe assemblies to be engineered down to 100 Å gap regime,[40] the possibility of electronic conduction based upon single or small packets of molecules has not been extensively addressed. The simplest electronic device, the one-dimensional wire, thus one-dimensional carbon chains, has the basic motif of a π-bonding system, allowing the conduction of electricity[41] as an electrical field mixes the ground and excited states of the molecule. Thus the promotion of an electron across the band-gap of the free molecule plays an important role, and it is this fundamental parameter (band-gap energy) that is essential to describe the behavior of molecular devices. Optical spectroscopy offers a straightforward method to measure this band-gap[42,43] as well as the ionization potentials and electron affinities of the wires, in addition to their bonding and physical structures. The ends of these carbon chains should be easily functionalized and may serve as "molecular clips" for making surface contacts with metal probes for molecular electronics studies.[44]

1.2 Astrophysical relevance

Molecules can exist in a wide range of astrophysical environments, from the extremely cold regions between stars to the atmospheres of stars themselves. Interstellar molecules can be identified through their electronic, vibrational and rotational spectrum. Typically, electronic transitions of simple molecules arise in the ultraviolet (UV) or visible portion of the spectrum; vibrational bands lie at infrared (IR) wavelengths; and rotational lines are seen at radio wavelengths. Hence, the study of interstellar molecules necessarily involves a wide range of observational techniques and instruments.

To date, around 150 molecular species have been tentatively or definitively identified in interstellar or circumstellar clouds, while about 50 have been identified in studies of comets in our solar system. One should define these astrophysical environments before exemplifying the specific regions where these molecules have been observed.

The interstellar medium (ISM) consists of gas and dust between stars, which accounts for 20-30% of the mass of our galaxy. Much of this material has been ejected by old and dying stars. The ISM contains different environments showing large ranges in temperature (10-10^4 K) and densities (100-10^8 H atoms/cm^3). It is filled with hydrogen gas, about 10% helium atoms, and $\sim$ 1% of atoms such as C, N, and O. Other elements are even less abundant. Roughly 1% of the mass is contained in microscopic (micron-sized) dust grains. The interstellar medium represents the raw material for forming future generations of stars, which may develop into planetary systems like our own. The ISM appears to contain a variety of cloud types, spanning a wide range of physical and chemical conditions: diffuse atomic and molecular clouds, translucent clouds, dense molecular clouds and dark molecular clouds. Interstellar clouds are neither uniform nor dynamically passive on long timescales. They display "clumpy" structures, are continually evolving as new stars form, and are enriched by material ejected from dying stars that was formed during stellar nucleosynthesis.

1.2.1 Diffuse atomic and molecular clouds

Diffuse atomic clouds represent the regime in the ISM that is fully unsheltered from the interstellar radiation field, and consequently nearly all molecules are quickly destroyed by photodissociation. Hydrogen is mainly in neutral atomic form, and atoms with ionization potential less than that of hydrogen (most notably carbon) are almost fully ionized, providing abundant electrons. Diffuse atomic clouds typically have a fairly low density ($\sim$ 10-100/cm^3), and temperatures of 30-100 K.

Diffuse molecular clouds represent the regime where the interstellar radiation field is sufficiently attenuated, at least at the individual wavelengths that dissociate H_2. However, enough interstellar radiation is still present to photoionize any atomic carbon, or to photodissociate CO, such that carbon is predominantly still in the form of C^+. In order to provide the shielding of radiation, in steady state, diffuse molecular clouds must necessarily be surrounded by diffuse atomic gas. This means that most radiations that cross a diffuse molecular cloud will also cross diffuse atomic gas.

The presence of abundant H_2 in diffuse molecular clouds permits the starting of the chemical processes. Molecules are observed in these clouds in absorption in the UV/visible (e.g., CO, CH, CN, C_2, C_3),[45] in the infrared (CO, H_3^+),[46] and at millimeter wavelengths (e.g., HCO^+, OH, C_2H). These clouds typically have densities on the order of 100-500/cm^3, and temperatures that range from 30-100 K.

1.2.2 Translucent clouds

The main characteristics of such clouds are relatively low temperatures (20-50 K) and densities of 500-5000/cm^3. VIS-IR absorption and millimeter absorption/emission are the observational techniques used to identify the molecules present in this environment. With sufficient shielding from interstellar radiation, carbon begins its transition from ionized atomic form into neutral atomic (C) or molecular (CO) form. The chemistry in this regime is qualitatively different than in the diffuse molecular clouds, both because of the decreasing electron fraction and because of the abundance of the highly reactive C atoms.[47]

In many ways, the translucent cloud regime is the least well understood of all cloud types. This is partly because of a relative lack of observational data, but also because theoretical models do not all agree on the chemical behavior in this transition region.

1.2.3 Dense clouds

These clouds are characterized by very low temperatures (10-30 K) and high densities (10^{4-8}/cm^3). The cold gas phase chemistry taking place in this environment can efficiently lead to the formation of simple species such as CO, N_2, O_2, C_2H_2, C_2H_4 and HCN, and simple carbon chains (Herbst 1995). Efficient accretion of atoms and molecules in such environments and subsequent reactions on the grain surface can easily induce the formation of molecules such as CO_2 and CH_3OH, which are later returned to the interstellar gas.[48] These clouds are the nascence sites of stars of all masses and their planetary systems. The building blocks for protostellar disks, from which planets, comets, asteroids, and other macroscopic bodies eventually form are the interstellar molecules and dust present in this environment.[49,50] Observations at infrared, radio, millimeter, and submillimeter frequencies show that a large variety of gas phase organic molecules are present in the dense interstellar medium.[51,52] These include organic classes such as nitriles, aldehydes, alcohols, acids, ethers, ketones, amines, and amides, as well as many long-chain hydrocarbon compounds.

1.2.4 Cold dark clouds

Stars and planets form within dark molecular clouds. The internal structure of these clouds, and consequently the initial conditions that give rise to star and planet formation is partially understood. The clouds are primarily composed of molecular hydrogen, which is virtually inaccessible to direct observation. But the clouds also contain dust, which is well mixed with the gas and which has well explained effects on the transmission of light. The hydrogen molecule possesses no dipole moment because of its symmetric structure and cannot produce an easily detectable signal under the conditions present in the cold, dark clouds. However, traditional methods used to derive the basic physical properties of such molecular clouds are making use of the observations of trace H_2 surrogates, the rare molecules with sufficient dipole moments to be simply detected by radio spectroscopic techniques, and interstellar dust.

Dust grains effectively shield molecules from interstellar UV photons, prior to the beginning of star formation. However, cosmic rays can pass through and drive a rich ion-molecule chemistry, enhanced by neutral-neutral processes, in which many complex organic species may be produced.[53] These reactions, along with grain surface processes, account for the high observed D/H ratios in interstellar molecules.[54]

The low temperature ($\sim$ 10 K) and lack of high-luminosity sources make these regions ideal testing grounds for models of gas-phase ion-molecule chemistry. The cold, dark clouds offer a rather mild environment; temperatures appear to be typically around $\sim 10\,\mathrm{K}$, with densities ranging up to 10^4-$10^5/\mathrm{cm}^3$. Nonetheless, an important fraction of the known interstellar molecules has been identified in such dark clouds. In fact, a number of these species, including the heavier cyanopolyynes and related molecules, have been found only in such regions.[55]

The dark cloud TMC-1 contains a special series of many unsaturated carbon chain molecules.[51] These include the cyanopolyynes ($HC_{2n+1}N$, n=1 - 5), various cumulene carbenes (H_2C_n, n=3,4,6), and chain radicals (HC_n, n=1-8, C_nN, n=1,3,5), as well as some methylated molecules such as methylcyanoacetylene (CH_3CCCN) and methyldiacetylene (CH_3CCCCH). Various small molecules (CCO, CCCO, CCS, CCCS) are observed; their higher homologues and new homologous series may also be present.[56–59]

1.2.5 Circumstellar envelopes

The massive circumstellar envelopes (CSEs) of late-type, post-AGB stars are decisive to the evolution of the ISM because they provide the dust and refractory species for the diffuse medium, and yet require the existence of the dense medium to generate the stars.

Substantial amounts of interstellar dust are known to be formed in the inner regions of the circumstellar envelopes of asymptotic stars. These grains are closely linked to the mass-loss process as they absorb stellar radiation and drag the gas away from the stellar surface, initiating in this way a mass-loss which leads to a the creation of a circumstellar envelope (CSE) which might contain up to a solar mass of gas. These CSEs incorporate a wide range of physical conditions, from very dense ($n(H_2) \sim 10^{15}/cm^3$), hot ($T \sim 2000\,K$) molecular gas just above the photosphere, to gas with properties similar to that found in dark molecular clouds, to diffuse regions dominated by the external UV radiation field which produces atomic gas far from the central star.[60]

Outflowing circumstellar envelopes[61] are, in a sense, chemical laboratories, where atoms created through stellar nucleosynthesis can react for the first time to form long-lived chemical bonds. Via radioastronomical measurements, the molecular distributions within such astrophysical environments could be traced. These information has provided insights into several aspects of chemical evolution, one if which is the involvement of metal-containing molecules. Among carbon-rich circumstellar outflows,[62] the representative source IRC+10216[63] has been found to contain several different metal-containing molecules, including NaCl, KCl, AlF, AlCl,[64] AlNC,[65] and the isomeric pair MgNC[66] and MgCN.[67] A group of these molecules has been found also in another object, the protoplanetary nebulae CRL 2688,[68] which represents a more advanced stage of stellar decomposition. While the molecules identified to date do not all appear to share a common origin, their most obvious characteristic is that all are halides or cynides of the lighter (and more cosmically abundant) main-group metal atoms.

Bibliography

[1] M. E. Jacox, Chem. Phys. **189**, 149 (1994).

[2] D. H. Russell, *Gas Phase Inorganic Chemistry*, Plenum, New York, 1989.

[3] P. Kebarle, Annu. Rev. Phys. Chem. **28**, 445 (1977).

[4] M. T. Bowers, *Gas Phase Ion Chemistry*, volume 1, Academic Press, New York, 1979.

[5] P. B. Armentrout, Science **251**, 175 (1991).

[6] M. V. Buchanan, *Fourier Transform Mass Spectrometry*, volume 359, American Chemical Society, Washington, DC, 1987.

[7] J. B. West, R. S. Bradford, J. D. Eversole, and C. R. Jones, Rev. Scient. Instrum. **46**, 164 (1975).

[8] J. M. Thompsen, P. M. Sheridan, and L. M. Ziurys, Chem. Phys. Lett. **330**, 373 (2000).

[9] M. A. Brewster and L. M. Ziurys, J. Chem. Phys. **113**, 3141 (2000).

[10] A. J. Apponi, M. A. Brewster, and L. M. Ziurys, Chem. Phys. Lett. **298**, 161 (1998).

[11] J. Xin and L. M. Ziurys, Astrophys. J. **501**, L151 (1998).

[12] J. S. Robinson, A. J. Apponi, and L. M. Ziurys, Chem. Phys. Lett. **278**, 1 (1997).

[13] M. A. Anderson and L. M. Ziurys, Astrophys. J. **460**, L77 (1996).

[14] M. A. Anderson, T. C. Steimle, and L. M. Ziurys, Astrophys. J. **429**, L41 (1994).

[15] B. P. Nuccio, A. J. Apponi, and L. M. Ziurys, Chem. Phys. Lett. **247**, 283 (1995).

[16] M. A. Anderson and L. M. Ziurys, Astrophys. J. **439**, L25 (1995).

[17] F. J. Grieman, S. H. Ashworth, J. M. Brown, and I. R. Beattie, J. Chem. Phys. **92**, 6365 (1990).

[18] J. R. Woodward, S. H. Cobb, and J. L. Gole, J. Phys. Chem. **92**, 1404 (1988).

[19] T. G. Dietz, M. A. Duncan, D. E. Powers, and R. E. Smalley, J. Chem. Phys. **74**, 6511 (1981).

[20] J. L. Gole, J. H. English, and V. E. Bondybey, J. Phys. Chem. **86**, 2560 (1982).

[21] G. K. Corlett, A. M. Little, and A. M. Ellis, Chem. Phys. Lett. **249**, 53 (1996).

[22] A. Bopegedera, C. R. Brazier, and P. F. Bernath, J. Mol. Spectrosc. **129**, 268 (1988).

[23] M. G. Li and J. A. Coxon, J. Mol. Spectrosc. **180**, 287 (1996).

[24] M. G. Li and J. A. Coxon, J. Mol. Spectrosc. **183**, 250 (1997).

[25] M. G. Li and J. A. Coxon, J. Mol. Spectrosc. **196**, 14 (1999).

[26] M. Elhanine, R. Lawruszczuk, and B. Soep, Chem. Phys. Lett. **288**, 785 (1998).

[27] H. Pines, *The Chemistry of Catalytic Hydrocarbon Conversions*, Academic Press, London, 1981.

[28] C. Masters, Adv. Organomet. Chem. **17**, 61 (1979).

[29] W. Beck, B. Niemer, and M. Wieser, Angew. Chem. Int. Ed. Engl. **32**, 923 (1993).

[30] G. Wilse, Angew. Chem. Int. Ed. Engl. **27**, 185 (1988).

[31] H. Wadepohl, Angew. Chem. Int. Ed. Engl. **31**, 247 (1992).

[32] W. A. Pliskin and R. P. Eischens, J. Chem. Phys. **24**, 482 (1956).

[33] N. Sheppard et al., Mol. Spectrosc. **97** (1968).

[34] J. Erkelens and J. T. Liefkens, J. Catal. **8**, 36 (1967).

[35] J. E. Demuth and D. E. Eastman, Phys. Rev. Lett. **32**, 1123 (1974).

[36] J. Li et al., Organometallics **11**, 3050 (1992).

[37] J.-M. Lehn, Angew. Chem. Int. Ed. Engl. **27**, 89 (1988).

[38] J. S. Miller, Adv. Mater. **2**, 378 (1990).

[39] D. H. Waldeck and D. N. Beratan, Science **261**, 576 (1993).

[40] W. P. Kirk and M. A. Reed, *Nanostructures and mesoscopic systems*, Academic Press, San Diego, 1992.

[41] http://www.nobel.se/chemistry/laureates/2000/index.html.

[42] J. Hsu et al., J. Phys. Chem. B **106**, 8582 (2002).

[43] P. Loubeyze, F. Occelli, and R. LeToullec, Nature **416**, 613 (2002).

[44] N. L. Abbott, J. P. Folkers, and G. M. Whitesides, Science **257**, 1380 (1992).

[45] E. B. Jenkins et al., Astrophys. J. **181**, L122 (1973).

[46] B. J. McCall, T. R. Geballe, K. H. Hinkle, and T. Oka, Science **279**, 1910 (1998).

[47] E. F. Van Dishoeck and J. H. Black, Astrophys. J. **334**, 771 (1988).

[48] A. G. G. M. Tielens and W. Hagen, Astron. Astrophys. **114**, 245 (1982).

[49] H. A. Weaver and L. Danly, *The Formation and Evolution of Planetary Systems*, Cambridge University Press, Cambridge, 1989.

[50] E. H. Levy and J. I. Lunine, *Protostars and Planets III*, volume 1596, University Arizona Press, 1993.

[51] M. Ohishi and N. Kaifu, Faraday Discussions **109**, 205 (1998).

[52] G. Winnewisser and C. Kramer, Space Science Reviews **90**, 181 (1999).

[53] T. J. Millar, P. R. A. Farquhar, and K. Willacy, Astron. Astrophys. **121**, 139 (1997).

[54] A. G. G. M. Tielens, Astron. Astrophys. **119**, 177 (1983).

[55] W. M. Irvine, M. Ohishi, and N. Kaifu, Icarus **91**, 2 (1991).

[56] M. C. McCarthy, M. J. Travers, A. Kovacs, C. A. Gottlieb, and P. Thaddeus, Astrophys. J. Suppl. Ser. **113**, 105 (1997).

[57] M. B. Bell et al., Astrophys. J. **518**, 740 (1999).

[58] P. Thaddeus, M. C. McCarthy, M. J. Travers, C. A. Gottlieb, and W. Chen, Faraday Discussions **109**, 121 (1998).

[59] M. Guélin et al., Astron. Astrophys. **317**, L1 (1997).

[60] L. M. Ziurys, PNAS **103**, 12274 (2006).

[61] M. Busso, R. Gallino, and G. J. Wasserburg, Ann. Rev. Astron. Astrophys. **37**, 239 (1999).

[62] G. Wallerstein and G. R. Knapp, Ann. Rev. Astron. Astrophys. **36**, 369 (1998).

[63] A. E. Glassgold, Ann. Rev. Astron. Astrophys. **34**, 241 (1996).

[64] J. Cernicharo and M. Guélin, Astron. Astrophys. **183**, L10 (1987).

[65] L. M. Ziurys et al., Astrophys. J. **564**, L45 (2002).

[66] K. Kawaguchi, E. Kagi, T. Hirano, S. Takano, and S. Saito, Astrophys. J. **406**, L39 (1993).

[67] L. M. Ziurys, A. J. Apponi, M. Guélin, and J. Cernicharo, Astrophys. J. **445**, L47 (1995).

[68] J. L. Highberger, C. Savage, J. H. Bieging, and L. M. Ziurys, Astrophys. J. **562**, 790 (2001).

2 Multiphoton ionization spectroscopy

2.1 Overview

Most of what is known about the interaction of light with matter comes from the study of single photon events. The laser has now made possible the observation of many novel and even exotic phenomena involving multiple photon processes. From the examination of these new nonlinear processes information can be gained on all aspects of laser excitation of atoms and molecules. In particular, one such process -multiphoton ionization of molecules- is one of the most interesting fields of research made possible by the development of powerful lasers. Multiphoton spectroscopy has been widely used in biology, chemistry, material science, physics, and other disciplines.

Multiphoton spectroscopy has made a great contribution to molecular spectroscopy. When a molecule is subjected to an intense radiation field, multiphoton ionization occurs with relative ease. A ground state electron is excited into the ionization continuum by simultaneous or sequential absorption of a number of photons. If an excited electronic state lies at the energy sum of two or three of these photons the ionization cross section can be greatly enhanced, resulting in a simultaneous two- or three-photon transition if symmetry and spin allowed. New vibronic and electronically excited states, which are not found in ordinary single-photon spectroscopy because of their different selection rules, can be observed in a wide range from lower excited states to continua. As mentioned above the possibility of simultaneous two-photon absorption or emission in molecules was made possible only after lasers were developed as an intense light source, especially when tunable dye lasers appeared after the late 1960s. In fact, compared with one-photon cross section for a typical molecule ($\sim 10^{-17}$ cm^2),[1] the cross sections of multiphoton transitions are extremely low at the intensity of conventional light sources: for example, $\sim 10^{-51}$ cm^{4}s and $\sim 10^{-82}$ cm^{6}s^2,[2] for two- and three-photon transitions, respectively.

Very high light intensities I [photons/cm^{2}s] are needed in order to achieve a significant transition probability, σI^N, therefore lasers are the only real option to use as light sources. Typical modern pulsed dye lasers have powers of around 1 mJ/10 ns pulse (10^5 watts in 10^{-8} s, or about 10^{23} photons/s or 10^{16} photons/pulse). These powers within a 1 mm^2 spot will give only $\sim 10^{-8}$ Einstein factor in each laser pulse for two-photon resonance. In turn, focusing to a radius of about 100 μm increases the probability of a two photon absorption to 10^{-2} in each laser pulse, whereas a typical one photon transition is already saturated by two orders of magnitude.

Such intensities are normally achieved by focussing the output of conventional (nanosecond pulse duration) tunable dye lasers. Side effect of it is the localization of the multiphoton excitation events in small space region (i.e. the focal volume) which makes the technique ideally suited to be used with molecular beams.

The field of multiphoton ionization spectroscopy, namely resonant enhanced multiphoton ionization (REMPI), on free radicals has seen a lot of developments in the past twenty years. In 1975 the first REMPI spectroscopic results where reported, studies on a stable radical, NO,[3] and soon afterwards the I_2 spectrum was recorded using this technique.[4] The first REMPI detection of a transient molecular free radical was reported in 1978, when NH (a $^1\Delta$) radicals were produced by multiphoton dissociation of NH_3.[5] Two years later another group reported REMPI spectra of vibrationally excited NH_2 ($\tilde{X}$ $^2B_1$) and bands of NH (a $^1\Delta$) radical produced by UV/visible multiphoton photolysis of NH_3.[6] Soon afterwards, the studies of methyl and trifluoromethyl radicals demonstrated that REMPI spectroscopy could conveniently and very sensitively detect nonfluorescent free radicals.[7,8] Since 1983 the REMPI spectroscopic data of free radicals have greatly expanded, revealing new spectroscopic knowledge leading to discovery of new electronic states of many transient species.

2.2 Characteristic properties of multiphoton transitions

Visible/UV multiphoton transitions have several characteristic features such as laser intensity dependence, resonance enhancement, and polarization dependence. The intensity dependence and resonance effect on molecular multiphoton spectroscopy are briefly outlined as follows.

2.2.1 Intensity dependence

The multiphoton probability is formulated according to time-dependent perturbation theory. As an example, a two-photon absorption from states a to n, as shown in Figure 2.1 is considered.

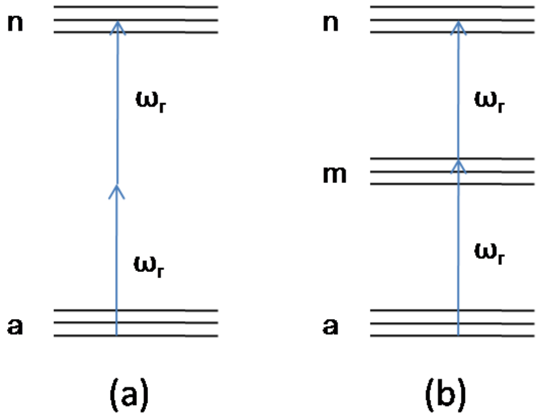

Figure 2.1: The two-photon absorption processes of a molecule:(a) nonresonant, (b) resonant.

The transition probability $W^{(2)}$, taking into account only the lowest order term of the radiation-molecule interaction, is given as

$$W^{(2)} \propto I^2 \mid \sum_m \frac{\langle n|\mu|m\rangle\langle m|\mu|a\rangle}{\Delta E_{ma} - \hbar\omega_r} \mid^2 \tag{2.1}$$

where I is the intensity of the laser, m the virtual intermediate states, ΔE_{ma} the energy difference between intermediate and initial states, μ the dipole moment, and ω_r the laser frequency. Equation (2.1) shows that the two-photon probability is proportional to the square of the laser intensity. Moreover, n-photon transition probability is proportional to I^n. This is called the formal intensity law for the multiphoton transition. If no saturation occurs, one can determine the order of the multiphoton transition from the log-log plot of the transition probability as a function of laser intensity,

$$\ln W^{(n)} = n \ln I + C \tag{2.2}$$

The transition rate constant for the n-photon process is proportional to the nth order of laser intensity: $k^{(n)} = (\sigma^{(n)} \cdot I^{(n)})/(\hbar\omega_r)^n$, where $\sigma^{(n)}$, I, and ω_r are the nth order transition cross section (strength) in units of cm^2, the laser intensity in units of photons $\mathrm{cm}^{-2}\mathrm{s}^{-1}$, and the laser frequency, respectively. The formal intensity law is found to hold well for nonresonant multiphoton processes and to hold sometimes for the resonant processes. The intensity law holds for multiphoton transitions of molecules irradiated just above the detection threshold by light from moderately high-power lasers. In multiphoton experiments in which a strong laser beam brings about the saturation of the population between the relevant states, one can often see a deviation from the intensity law and also in the case of multiphoton processes via resonant states. In a following section, using the rate equation approach, it will be shown that the deviation is interpreted by means of saturation between initial and resonant states.

2.2.1.1 The formal intensity law

The formal intensity law, I^n-intensity dependence of the observed quantities, has been utilized to determine the orders of multiphoton processes such as excitation, ionization and/or dissociation of molecules. Figure 2.2 shows log-log plots of the ion yield versus laser intensity for two-photon ionization of aniline observed by Brophy and Rettner (1979). The laser pulse with a 293.9 nm wavelength and a pulse duration $t_p \sim 1\mu s$ excites the first singlet state $^1B_2$ of aniline. In Figure 2.2b the I^2-intensity dependence of the ion yield can be seen at the lowest intensities corresponding to the unfocused Nd^{3+}-YAG pumped laser.

The estimated values of the cross sections are $\sigma_1 = (1.0 \pm 0.2) \times 10^{-17}\,\mathrm{cm}^2$ and $\sigma_2 = (3.5 \pm 0.8) \times 10^{-17}\,\mathrm{cm}^2$ for the absorption from the $^1A_1$ to the $^1B_2$ resonant state and that from the resonant to the ionized state, respectively. Assuming a

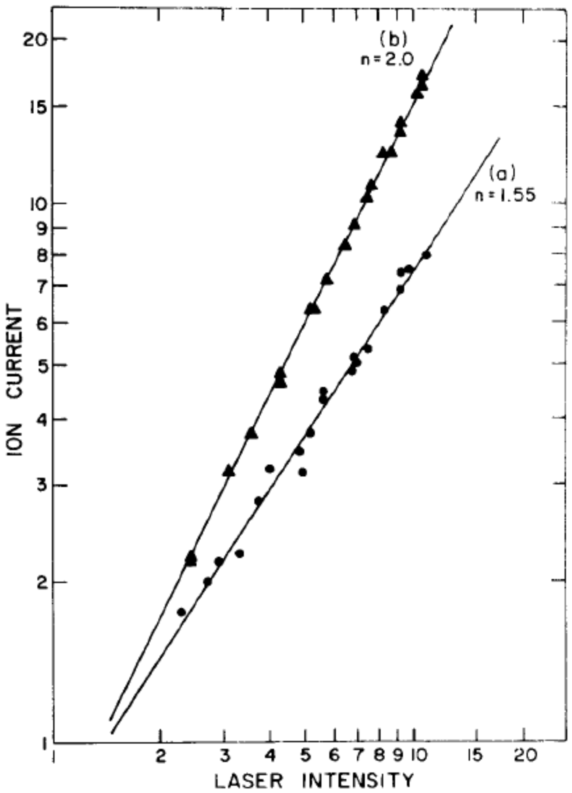

Figure 2.2: Intensity dependence of the ion yield produced by resonant two-photon ionization via the $^1B_2$ state of aniline: (a) with a focused high-power laser, (b) with an unfocused laser.[9]

1-kW laser pulse, the absorption rate constants $\mathrm{k}^{(1)}_{B_2A_1}$ and $\mathrm{k}^{(1)}_{fB_2}$ are found to be $10^5\,\mathrm{s}^{-1}$, and the condition $\mathrm{k}^{(1)}_{B_2A_1}\mathrm{t_p}$ and $\mathrm{k}^{(1)}_{fB_2}\mathrm{t_p}\simeq 10^{-1}<1$ is satisfied. Under this condition, the ion yield $R_\mathrm{f}(\mathrm{t_p})$ can be safely expressed as

$$R_\mathrm{f}(\mathrm{t_p}) = \sigma^{(1)}_{\mathrm{f}B_2}\sigma^{(1)}_{B_2A_1}\mathrm{t_p^2}I^2/2(\hbar\omega_r)^2 \tag{2.3}$$

which represents the formal intensity law for n=2 and has been derived by using a simple kinetic equation (see section 2.2.1.3). The linear plot of the ion yield with a slope of 1.5 (Figure 2.2) has been measured by using a high-power, strongly focused laser beam.

2.2.1.2 Saturation phenomena

The I^n dependence generally holds for cases of low-intensity laser experiments, long-lived intermediate states for short pulse times, and before the steady-state condition is satisfied for resonant multiphoton processes. The use of high-intensity lasers may result in saturation of the population between the resonant and ground states and make it easy to reach a steady-state condition. Boesl *et al.* reported the REMPI spectrum of benzene, via the resonant 6^1 vibronic state of S_1. The intensity dependence of the ion number has been monitored for different laser intensities with an unfocused parallel light beam and focused laser light, respectively. A pure quadratic intensity dependence that obeys the formal intensity law is observed for laser intensities below $10^7\,\mathrm{W\ cm^{-2}}$. Above this threshold value of ion number changes from quadratic to roughly linear intensity dependence.[10] Theoretical considerations for the deviations of transition probability, ion current, and yield from I^n-dependence have been reported by several authors.[11–13]

2.2.1.3 The rate equation approach

One of the methods used to study the deviation from I^n-dependence is the rate equation approach.[13] For simplicity the resonant two-photon ionization approach is considered as shown in Figure 2.3.

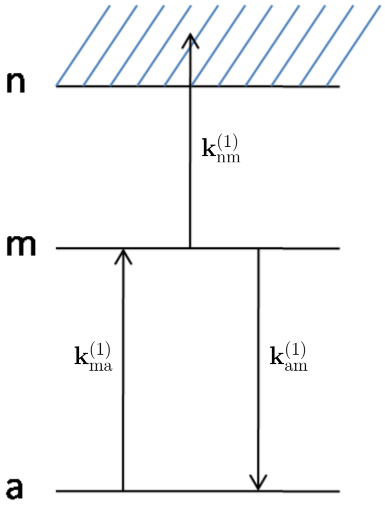

Figure 2.3: A simple model for two-photon ionization.

The rate equations associated with two-photon ionization for states a and n through a resonant state m can be expressed as:

$$d\rho_a(t)/dt = -k^{(1)}_{aa}\rho_a(t) + k^{(1)}_{am}\rho_m(t), \tag{2.4}$$

$$d\rho_m(t)/dt = -k^{(1)}_{mm}\rho_m(t) + k^{(1)}_{ma}\rho_a(t), \tag{2.5}$$

$$d\rho_n(t)/dt = k^{(1)}_{mm}\rho_m(t), \tag{2.6}$$

where $\rho_a(t) \equiv \rho_{aa}(t)$ is the density matrix element for the initial state, and $k^{(1)}_{am}$= $k^{(1)}_{aa:mm}$ the radiative rate constant associated with the transition from states m to a. The rate constants satisfy $\mathrm{k}^{(1)}_{mm}$=$\mathrm{k}^{(1)}_{am}$+$\mathrm{k}^{(1)}_{nm}$ and $\mathrm{k}^{(1)}_{aa}$=$\mathrm{k}^{(1)}_{ma}$. In this treatment effects of the simultaneous two-photon process, specified by $\mathrm{k}^{(2)}_{na}$ and $\mathrm{k}^{(2)}_{aa}$, and the relaxation have been omitted. The Laplace transformation of Eqs. (2.4) and (2.5) yields:

$$[p + k^{(1)}_{aa}]\rho_a(p) = N_0 + k^{(1)}_{am}\rho_m(p), \tag{2.7}$$

$$[p + k^{(1)}_{mm}]\rho_m(p) = k^{(1)}_{ma}\rho_a(p), \tag{2.8}$$

where

$$\rho(p) = \int_0^\infty dt\rho(t)e^{-pt}. \tag{2.9}$$

The initial conditions have been assumed ρ_a(t=0)=N$_0$ and ρ_m(t=0)=ρ_n(t=0)=0. The solution is written as:[14]

$$\rho_m(p) = \frac{k^{(1)}_{ma}N_0}{(p-\alpha_1)(p-\alpha_2)}, \tag{2.10}$$

$$\rho_a(p) = \frac{N_0}{\alpha_1-\alpha_2}\left[\frac{(k^{(1)}_{mm}+\alpha_1)}{p-\alpha_1} - \frac{(k^{(1)}_{mm}+\alpha_2)}{p-\alpha_2}\right], \tag{2.11}$$

where α_1 and α_2 are the solution for the equation:

$$[p + k_{aa}^{(1)}][p + k_{mm}^{(1)}] - k_{am}^{(1)} k_{ma}^{(1)} = 0, \tag{2.12}$$

The ionization rate is proportional to dρ_n(t)/dt, which is given by:

$$\frac{d\rho_n(t)}{dt} = \frac{k_{nm}^{(1)} k_{ma}^{(1)} N_0}{\alpha_1 - \alpha_2} (e^{\alpha_1 t} - e^{\alpha_2 t}) \tag{2.13}$$

The ion yield in the case of a square laser pulse can be obtained by integrating Eq. (2.13) over t and dividing the resulting expression by N$_0$ as

$$R_n(t_p) = \frac{\rho_n(t_p)}{N_0}, \tag{2.14}$$

where t$_p$ is the pulse duration.

In the case of a weak laser intensity, the effect of stimulated emission is negligible and the contribution of k$_{am}^{(1)}$ to the intensity dependence may be neglected. In this case α_1 and α_2 can be approximated with α_1=-k$_{nm}^{(1)}$ and α_2=-k$_{ma}^{(1)}$. The ionization rate can be then approximated as:

$$\frac{d\rho_n(t)}{dt} \simeq k_{nm}^{(1)} k_{ma}^{(1)} N_0 t e^{-k_{ma}^{(1)} t} \simeq k_{nm}^{(1)} k_{ma}^{(1)} N_0 t = \frac{\sigma_{nm}^{(1)} \sigma_{ma}^{(1)}}{(\hbar\omega_r)^2} N_0 I^2 t. \tag{2.15}$$

The ion yield R$_n$(t$_p$) is expressed as:

$$R_n(t_p) = \frac{\rho_n(t_p)}{N_0} = \frac{\sigma_{nm}^{(1)} \sigma_{ma}^{(1)}}{2(\hbar\omega_r)^2} I^2 t_p^2, \tag{2.16}$$

In the case of k$_{ma}^{(1)}$$\simeq$k$_{nm}^{(1)}$, the quadratic intensity dependence can be also derived as:

$$\frac{d\rho_n(t)}{dt} \simeq 1/2(k_{nm}^{(1)} k_{ma}^{(1)}) N_0 t). \tag{2.17}$$

In other words in case of weak laser field, in which laser pulse duration satisfies k$_{ma}^{(1)}$t$_p$<1, the formal intensity law holds for the ion current and yield.

In the case of a strong laser intensity the stimulated emission can no longer be neglected and the spontaneous emission can be safely omitted, k$_{am}^{(1)}$=k$_{ma}^{(1)}$. The α_1 and α_2 solutions would include now the stimulated emission term and the ionization rate is redefined as:[14]

$$\frac{d\rho_n(t)}{dt} = \frac{k_{nm}^{(1)}k_{ma}^{(1)}N_0}{\alpha_1 - \alpha_2}e^{\alpha_1 t}[1 - e^{-(\alpha_1-\alpha_2)t}]. \tag{2.18}$$

Here α_1 and α_2 are linear functions of the laser intensity. For the time scale $t<(\alpha_1-\alpha_2)^{-1}=[4(k_{ma}^{(1)})^2+(k_{nm}^{(1)})^2]^{-1/2}$,

$$\frac{d\rho_n(t)}{dt} \simeq k_{nm}^{(1)}k_{ma}^{(1)}N_0 t, \tag{2.19}$$

and for time scale $t>(\alpha_1-\alpha_2)^{-1}$,

$$\frac{d\rho_n(t)}{dt} \simeq \frac{k_{nm}^{(1)}k_{ma}^{(1)}N_0}{[4(k_{ma}^{(1)})^2 + (k_{nm}^{(1)})^2]^{-1/2}}, \tag{2.20}$$

The two equations above indicate quadratic and linear intensity dependencies, respectively. The deviation of the intensity from the I^2 dependence takes place at $t>(\alpha_1-\alpha_2)^{-1}$, and

$$\frac{d\rho_n(t)}{dt} \simeq \frac{k_{nm}^{(1)}N_0}{2}, \tag{2.21}$$

for $k_{ma}^{(1)}=k_{am}^{(1)}>k_{nm}^{(1)}$

$$\frac{d\rho_n(t)}{dt} \simeq k_{ma}^{(1)}N_0, \tag{2.22}$$

for $k_{am}^{(1)}<k_{nm}^{(1)}$.

The absorption rate constants are proportional to the cross section as well as to the laser intensity. Therefore, an appreciable difference between $\sigma_{ma}^{(1)}$ and $\sigma_{nm}^{(1)}$ may change the I^n intensity dependence of multiphoton processes, even in the presence of weak laser field.

The above rate equation treatment of the saturation phenomena treated above is useful in determining if the resonant process is a two or a multiphoton process. The quadratic or linear intensity dependence character of a multiphoton process can be determined by measuring the ion yield and plotting it against the laser's intensity.

In order to determine the saturation intensity of a molecular transition of a given oscillator strength another approach has to be considered. The rate equation is applied for an open two level system, assuming a rotational transition from level

$|1\rangle$ to level $|2\rangle$. Demtröder treats the saturation problem of a molecular transition taking into account also the relaxation processes such as spontaneous emission and other phenomena that depopulate or repopulate a particular level.[15]

The saturation parameter is defined as:

$$S = \frac{B_{12} \cdot I_\nu}{R^* \cdot c}, \tag{2.23}$$

where B_{12} is the Einstein B coefficient, I_ν is the laser intensity and R^* is the mean of relaxation processes. The intensity $I=I_s$ at which the saturation parameter becomes $S=1$ is called the saturation intensity and is defined as:

$$I_s \approx \frac{R^* \cdot c}{B_{12}} \cdot \Delta\nu_L, \tag{2.24}$$

Case study

Saturation of a molecular transition in a molecular beam by a broadband cw laser width $\Delta\nu_L$=4.5×10^9 s^{-1} (=0.15 cm^{-1}). The molecular transition considered here is the rotational excitation from J'=14 to J''=13 in the $A\ ^1\Pi \leftarrow X\ ^1\Sigma^+$ electronic transition of linear AlCCH. The linewidth of this particular transition has been estimated to be 0.3841 cm^{-1}. The mean relaxation rate can not be calculated precisely because the rates of all relaxation processes are not known. Nevertheless, based on the linewidth of the transition mentioned above a relaxation rate R is estimated to be 7.25·10^{10} s^{-1}.

The Einstein A coefficient (spontaneous emission coefficient) is related to the dipole moment μ_{12} by:[16]

$$A_{21} = |\mu_{12}|^2 \cdot \nu_{12}^3 [8\pi^2/(3\hbar\varepsilon_0)], \tag{2.25}$$

The Einstein B coefficient is then related to the spontaneous emission coefficient by:

$$B_{12} = (c^3/8\pi h\nu^3)A_{21}, \tag{2.26}$$

The oscillator strength of the $A\ ^1\Pi \leftarrow X\ ^1\Sigma^+$ electronic transition of linear AlCCH has been calculated to be 1.6×10^{-3}. The dipole moment can be estimated based on the following relation:[16]

$$f_{12} = |\mu_{12}|^2 \cdot \nu_{12}[4\pi m_e c/(3\hbar e^2)], \tag{2.27}$$

where m_e and e are the mass and charge of the electron, ν_{12} is expressed in cm^{-1} and μ_{12} in Debye. Based on the above equation the dipole moment for the electronic transition is calculated to be 0.343 Debye (1 Debye=$3.336\cdot10^{-30}$ Coulomb·m). The dipole moment can be used now to calculate the A_{21} coefficient for the transition located at 347.7 nm. The permittivity of vacuum is $8.854\cdot10^{-12}$ $J^{-1}\cdot$Coulomb$^2\cdot$ m^{-1} and $\hbar$=$1.054\cdot10^{-34}$ J·s. Using all the known parameters mentioned above the A_{21} is calculated to be $8.83\cdot10^5$ s^{-1}.

The saturation intensity can be now estimated considering all the parameters from equation 2.24. The value obtained for cw laser is 4.38×10^{10} W/m^2. For a pulsed dye laser with a pulse width of 10 ns and the beam diameter of $\approx$ 3 mm^2, the saturation intensity is $\approx$1.461 mJ.

2.2.2 Resonant effect

When the laser is tuned and its frequency approaches a real intermediate electronic state (Figure 2.1b), we can see a drastic increase in the two-photon absorption signal (resonance enhancement). This process is called a resonant two-photon transition. If a rigorous resonance condition were satisfied, that is, $\Delta E_{ma}=\hbar\omega_r$ in Equation (2.1), then the magnitude of the transition probability would go to infinity. However, the energy levels of intermediate states are not infinitely sharp but have widths Γ_{ma}, and the divergence of the transition can be avoided. The width originates from intra- and inter-molecular perturbations and from higher order radiation-molecule interaction. In order to take the resonant effect into account phenomenologically, the real energy denominator in Equation (2.1) is replaced by a complex energy denominator with the term $i\Gamma_{ma}$. If the higher order radiation-molecule interaction is neglected, Γ_{ma} is called the dephasing constant -

it describes the rate of phase loss between the m and a states associated with the transition, and it may be expressed as:

$$\Gamma_{ma} = \frac{1}{2}(\Gamma_{mm} + \Gamma_{aa}) + \Gamma_{ma}^{(d)} \tag{2.28}$$

where Γ_{mm} and Γ_{aa} are the population decay constants of state m and a, respectively, and $\Gamma_{ma}^{(d)}$ is the pure dephasing constant that originates from a molecule-perturber elastic scattering process.

It is interesting to note that the vibronic structure appearing in the resonant multiphoton transition is generally different from that in the non-resonant transition: in the former case the vibronic structure reflects the potential differences between the initial, resonant, and final states or between these states, and in the latter case the vibronic structure is mainly determined by the Franck-Condon vibrational overlap integral between the initial and final states, since the energy mismatch to the intermediate states is so large that the vibronic structure of the intermediate state $|m\rangle$ may be neglected in Equation (2.1).

2.3 REMPI mechanism

Multiphoton absorption processes can be classified into two categories: "simultaneous" and "stepwise" processes. In nature the simultaneous absorption of more than one photon is a rare event. But when atoms and molecules are irradiated with extreme intensity of focused laser beam such as those generated by excimer and Nd^{3+}:YAG pulsed dye lasers, simultaneous photon absorption rates become greatly enhanced. A sufficiently intense laser can cause any molecule to simultaneously absorb enough photons to ionize. Under typical laser conditions ionization rates decrease rapidly with photon order, the simultaneous three photon absorption rate is much slower than the simultaneous two photon absorption rate and so forth.

The ionization rate of chemical species is greatly enhanced when the path to ionization is divided into two or more successive absorption steps (resonances) of lower photon order. These absorption steps are provided by stable electronic states that can accumulate a population. In Figure 2.4 the sum of two laser photons is resonant with an excited molecular state. This molecular state accumulates a population by simultaneous two photon absorption. Absorption of one more photon promotes the excited state molecule above its ionization potential and the molecule ionizes. The REMPI signal is detected by measuring the photoelectrons or laser generated cations.

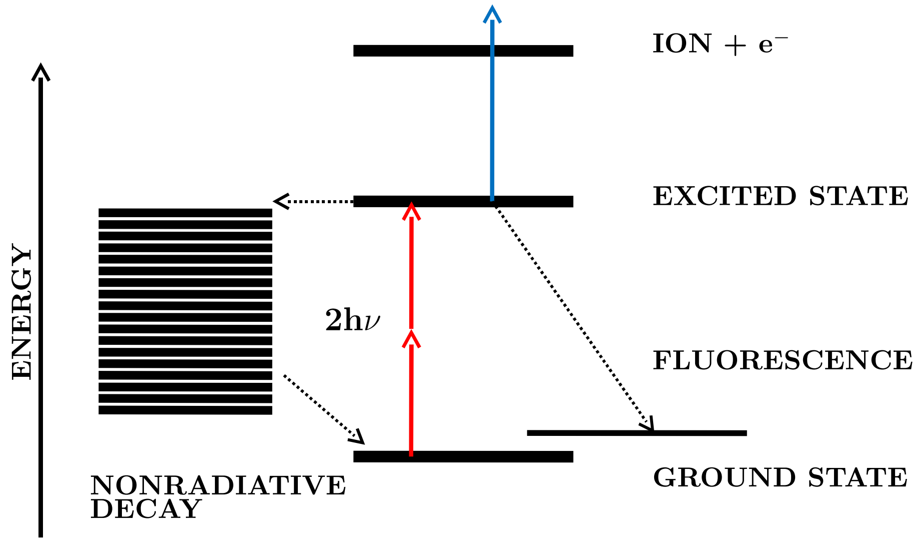

Figure 2.4: Schematic of a [2+1] REMPI process. The competing processes, intramolecular relaxation and fluorescence, which deplete the excited state population and reduce the ion yield are also shown.

The complete excitation process depicted in Figure 2.4 is called a [2+1] REMPI mechanism; two photon absorption populates a stable "resonant" electronic state and an additional one photon absorption step ionizes the molecule. In fact, within any n-photon ionization experiment which involves one stable resonant molecular state and one laser frequency the REMPI signal may arise from at least n-1 possible excitation schemes.

[1+1] scheme

The one-color two-photon [1+1] scheme is one type of REMPI technique. In the [1+1] scheme, the laser is scanned over the rovibronic levels of the electronic excited state of the molecules of interest. An ionizing photon from the same laser promotes the neutral species from the excited state to the ground state of the corresponding ions. In the [1+1] scheme, the energy of one photon must be $\geq 1/2$ of the ionization potential (IP). Because the IP of most hydrocarbon clusters are more than 8 eV, the [1+1] scheme is not suitable to measure their visible electronic spectra. The one-color one-photon scheme proved to be useful for recording the spectrum of the diatomic species like titanium oxide (TiO with an IP of 6.8 eV).

[1+1'] scheme

In the [1+1'] scheme, the first color laser is scanned over the rovibronic level of the electronic excited state and the second color ionizes the species of interest. This scheme requires the sum of the two different photons to equal the IP of the molecule. Thus, the [1+1'] scheme is suitable for measuring the electronic spectra of molecules in a very broad range from UV to visible using different combination of $h\nu_1$ and $h\nu_2$. This scheme has been employed to record the spectra of molecules mentioned in this thesis. The [1+1'] configuration is the most appropriate to record the spectra of the hydrocarbons of astrophysical interest that absorb in the visible region of the electromagnetic spectrum. The combination of a dye laser with an F_2 laser (7.9 eV) has proven to be successful for measuring the gas-phase electronic spectra of most hydrocarbon clusters in the visible region.[17,18]

[2+1] and [2+1'] scheme

When one single photon can not bring the molecule in the excited state then the sum of the two photons will equal the energy required to make the allowed transition. The probability of absorption is greatly increased if further absorption of a third photon is sufficient to ionize the molecule.

Combination of photons of different energies may also be used ([2+1'] scheme). For example, one laser may be tuned to a two-photon absorption in the molecule, and then a second laser used to perform the ionization step. Because the absorption probability greatly increase, higher order processes, such as three photon absorption, are relatively rare. The very low number density of clusters and low signal to noise ratio limit the practical probability of using [2+1] or [2+1'] schemes or other higher order multiphoton schemes. In general, combinations of low order processes, utilizing multiple frequencies (color) are more commonly used.

To date, the REMPI spectra have only reflected the properties of the initial state and of a resonant intermediate excited state. The final absorption step which produces the ion does not appear to influence the spectrum strongly. This fact can be rationalized by recognizing that the ejection of an electron is usually very rapid (10^{-13} - 10^{-15} seconds).

Loss mechanisms which deplete the resonant excited state population before the ionizing photon is absorbed, reduce the ion yield. Figure 2.4 shows some of these signal loss mechanism which include 1) fluorescence from the resonant excited state to lower states, 2) collisionless and colisionally induced nonradiative relaxation of the resonant excited state into the dense background of vibrational levels associated with lower electronic states, and 3) predissociation into smaller neutral species. Because laser ionization occurs in less time than the laser pulse width (10^{-12} - 10^{-8} seconds), loss mechanisms cannot strongly attenuate the ion signal until their rates approach the inverse of the laser pulse duration. For example, evidence indicates that REMPI can overcome moderately rapid predissociation.[19,20]

As a molecule's size and mass increase, dynamical aspect becomes more and more important. Middle sized closed shell stable molecules often possess relatively large energy gaps between their ground and first excited states. Therefore nonradiative decay is slow. Particularly popular systems for study using REMPI techniques were substituted benzenes. Their first excited (S_1) singlet states are generally stable, they have low first IPs - less than twice the S_1-S_0 energy separation (the S_1-S_0 transition is thus well suited to study by [1+1] REMPI) and the S_1-S_0 transition has a large oscillator strength and falls in an experimentally convenient wavelength range. However spectroscopic study of S_2 is restricted in relatively low resolution due to lifetime broadening. The situation generally worsens with every next electronic state. Increasing density of vibronic states, generated by lower lying electronic energy levels, leads to increasingly efficient intramolecular processes by removing the molecule's excitation induced by the tunable laser at the first step of REMPI. In extreme cases this depletion may occur on time scales shorter than delay before arrival of next laser photons.

Using a variable time delay between the excitation step and the subsequent photoionization, it is possible to derive kinetic information about intramolecular vibrational redistribution and vibrational predissociation in selected vibronic levels of the excited state of the molecule. Often, however, the timescale provided by conventional (nanosecond) pulsed lasers is not appropriate. To compete effectively with these ultrafast energy redistribution processes a change from nanosecond to subpicosecond time scales is required.

2.4 Multiphoton selection rules

As molecular symmetry increases, the number of excited states which are inaccessible to one photon spectroscopy also increases. Most of these "forbidden" states are accessible through two or three photon transitions. To help the experimentalist, several papers have listed selection rules, rotational line strengths, and polarization factors for two, three, and four photon absorption experiments on diatomic, symmetric and asymmetric top species.[21–24]

In diatomic molecules governed by Hund's case (a) or (b) the one photon selection rule, $\Delta\Lambda = 0, \pm 1$, becomes $\Delta\Lambda = 0, \pm 1, \pm 2, \ldots \pm n$ for n-photon absorption. As the photon order of the resonant transition increases, new states become accessible. For example, one photon absorptions from Σ states permit the transitions, $\Sigma \leftarrow \Sigma$ and $\Pi \leftarrow \Sigma$. Simultaneous two photon absorption permits the additional transition, $\Delta \leftarrow \Sigma$, and three photon absorption adds the transition, $\Phi \leftarrow \Sigma$.

Multiphoton transitions give rise to more rotational branches. Whereas one photon absorption bands may display P, Q, and R branches ($\Delta J = 0, \pm 1$), two photon bands may show O, P, Q, R, and S branches ($\Delta J = 0, \pm 1, \pm 2$) and three photon bands may show N, O, P, Q, R, S, and T branches ($\Delta J = 0, \pm 1, \pm 2, \pm 3$). The specifics of state symmetries, angular momentum coupling, and rotational line strength factors may greatly simplify the spectrum by attenuating or eliminating branches. Rotational branches often coincide. But in practice additional branches associated with multiphoton transitions often congest REMPI bands sufficiently to preclude an extensive rotational analysis.

During standard deviations of the one photon vibrational selection rules for polyatomic molecules, the Born-Oppenheimer approximation is invoked to separate the electronic and nuclear wavefunctions. This separation permits independent solution of the electronic and vibrational interaction integrals which yield the electronic and vibrational selection rules. In similar fashion the application of the Born-Oppenheimer approximation permits division of the multiphoton interaction integrals into vibrational and electronic parts. With this approximation the vibrational interaction integral becomes identical to the one photon interaction integral. Thus, the same vibrational selection rules govern both one and multiphoton transitions.

The vibrational selection rules for polyatomic species have been described by Herzberg.[25] The strongest of these asserts that totally symmetric (e.g. a_1) vibrational modes follow the selection rule, $\Delta\nu = 0, \pm1, \pm2, \ldots$ and that vibrational modes that are not totally symmetric are governed by the selection rule, $\Delta\nu = 0, \pm2, \pm4, \ldots$.

Rotationally resolved [2+1] REMPI spectrum of HCO radical[26] has been found to confirm the selection rules for multiphoton processes where 2 more branches (O and S) are observed in the spectrum. Vibrationally analyzed [2+1] REMPI spectrum have been reported for few radicals (CH_3,[27] $CHCl_2$[28]) of C_{2v} symmetry or higher. In each band system symmetric and nonsymmetric modes were assigned and found to conform to the vibrational selection rules mentioned above.

Bibliography

[1] M. N. R. Ashfold and J. D. Howe, Annu. Rev. Phys. Chem. **45**, 57 (1994).

[2] P. M. Johnson and C. E. Otis, Annu. Rev. Phys. Chem. **32**, 139 (1981).

[3] P. M. Johnson, M. R. Berman, and D. Zakheim, J. Chem. Phys. **62**, 2500 (1975).

[4] G. Petty, C. Tai, and F. W. Dalby, Phys. Rev. Lett. **34**, 1207 (1975).

[5] G. C. Nieman and S. D. Colson, J. Chem. Phys. **68**, 5656 (1978).

[6] J. H. Glownia, S. J. Riley, S. D. Colson, and G. C. Nieman, J. Chem. Phys. **73**, 4296 (1980).

[7] M. T. Duignan, J. W. Hudgens, and J. R. Wyatt, J. Phys. Chem. **86**, 4156 (1982).

[8] J. W. Hudgens, T. G. DiGiuseppe, and M. C. Lin, J. Chem. Phys. **79**, 571 (1983).

[9] J. H. Brophy and C. T. Rettner, Chem. Phys. Lett. **67**, 351 (1979).

[10] U. Boesl, H. J. Neusser, and E. W. Schlag, Chem. Phys. **55**, 193 (1981).

[11] O. Kafri and S. Kimel, Chem. Phys. **5**, 448 (1974).

[12] P. Lambropoulos, Phys. Rev. A **9**, 1992 (1974).

[13] D. H. Parker, J. O. Berg, and M. A. El-Sayed, Adv. Laser Chem. **3**, 320 (1978).

[14] S. J. Lin, Y. Fujimura, H. J. Neusser, and E. W. Schlag, *Multiphoton Spectroscopy of Molecules*, Academic Press, Orlando, 1984.

[15] W. Demtröder, *Laser spectroscopy: Basic concepts and instrumentation*, Springer-Verlag Berlin, 2003.

[16] H. Lefebvre-Brion and R. Field, *Perturbations in the spectra of diatomic molecules*, Academic Press Inc.,Orlando, FL, 1986.

[17] H. Ding, T. Pino, F. Güthe, and J. P. Maier, J. Chem. Phys. **115**, 43 (2001).

[18] H. Ding, T. Pino, F. Güthe, and J. P. Maier, J. Chem. Phys. **117**, 50 (2002).

[19] J. Danon, H. Zacharias, H. Rottke, and K. H. Welge, J. Chem. Phys. **76**, 2399 (1982).

[20] J. C. Miller and W. C. Cheung, J. Phys. Chem. **89**, 1643 (1985).

[21] G. Placzek and E. Teller, Z. Phys. **81**, 209 (1933).

[22] J. B. Halpern, H. Zacharias, and R. Wallenstein, J. Mol. Spectrosc. **79**, 1 (1980).

[23] R. N. Dixon, J. M. Bayley, and M. N. R. Ashfold, Chem. Phys. **84**, 21 (1984).

[24] M. N. R. Ashfold, R. N. Dixon, J. D. Prince, and B. Tutcher, Mol. Phys. **56**, 1185 (1985).

[25] G. Herzberg, *Molecular Spectra and Molecular Structure. III. Electronic Spectra and Electronic Structure of Polyatomic Molecules*, D. van Nostrand, New York, 1966.

[26] P. J. H. Tjossem, P. M. Goodwin, and T. A. Cool, J. Chem. Phys. **84**, 5334 (1986).

[27] T. G. DiGiuseppe, J. W. Hudgens, and M. C. Lin, J. Phys. Chem. **86**, 36 (1982).

[28] G. R. Long and J. W. Hudgens, J. Phys. Chem. **84**, 5870 (1987).

3 Experimental setup

The experimental setup used in our laboratory is depicted in Figure 3.1 consisting of molecular source, ionization region and detection system. Transient species are produced either by an electrical discharge of a precursor gas diluted in an inert buffer, or through ablation of a solid precursor material (rod or disc), like carbon, boron or a metal target. Two lasers are used and applied in sequence. The first pulse (λ_1) promotes the molecules of interest into an excited electronic state and a second laser pulse (λ_2) ionizes the excited species.

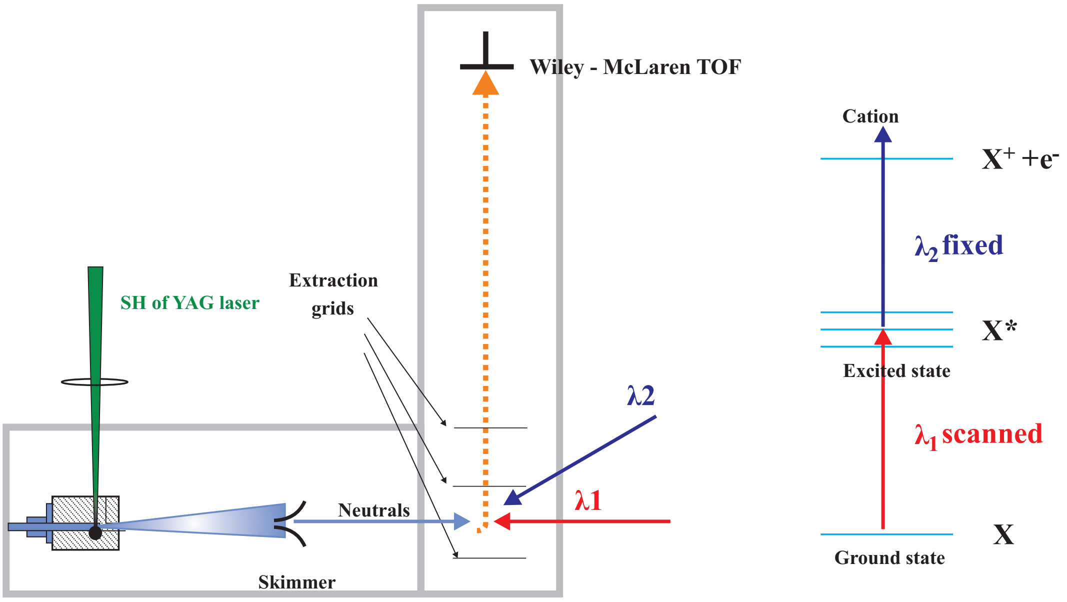

Figure 3.1: REMPI experimental setup.

The resulting ions are analyzed using a Wiley-McLaren[1] time-of-flight (TOF) mass spectrometer equipped with a microchannel plate (MCP) detector. This technique allows the absorption spectra for many different radicals of different masses to be recorded all at once. However, only neutral species with suitable excited electronic states can be detected. Its greatest advantage lies in its mass-selectivity, which allows one to make an unambiguous assignment of the absorption features.

3.1 Molecular sources

3.1.1 Discharge source

The discharge source, a universal synthesizer of carbon species, is depicted in Figure 3.2. Based on the design of Ohshima and Endo[2] it is indispensable for producing a great variety of both neutral and ionic hydrocarbon radicals. Nearly all carbon-chain-related spectroscopic gas phase studies in the J.P. Maier group in Basel have been done using this "pinhole" discharge source or its slit modification.[3,4] A precursor diluted with buffer gas (Ar, Ne, He, N_2,etc.) down to 0.15-3% is expanded under 5-10 bar backing pressure into vacuum through the ceramic body. The precursors used are hydrocarbons such as CH_4, C_2H_2 or C_4H_2, and recently used are the organometallic precursors such as iron-pentacarbonyl ($Fe(CO)_5$) or tetramethyl-aluminum ($Al(CH_3)_4$). The gas burst generated by an electromagnetic valve (General Valve 106, ø0.7 nm) is computer controlled.

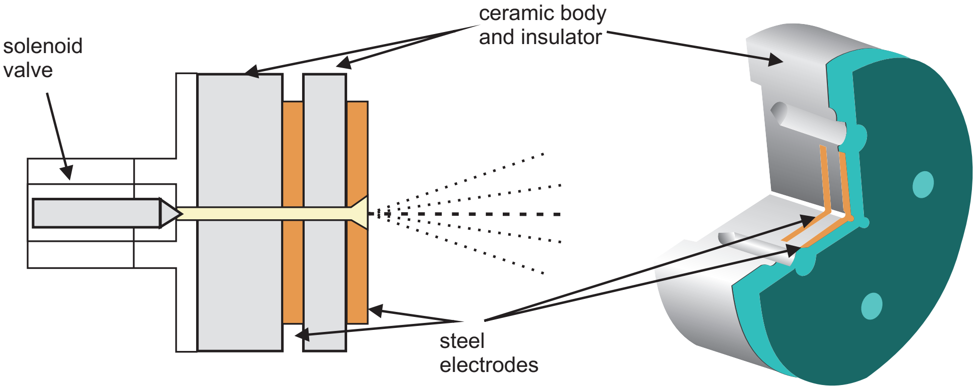

Figure 3.2: Discharge source

The amount of gas released is varied by manipulating the width of the valve opening pulse. This parameter directly relates with the pressure in the source chamber and allows one to keep the latter constant and thus ensuring stable source conditions. A 100-200 μs long high voltage pulse (-700-900 V) from a home-built power supply is applied between the stainless steel electrodes placed on either side of the 10-20 mm thick insulating spacer. The stainless steel electrodes were often replaced with silver electrodes to eliminate the generation of atomic species from the electrodes, which would otherwise overlap in mass with the species of interest. The channel is 1-1.2 mm thick all the way through the source, except for the insulator section where it is enlarged to 2 mm in order to create a localized plasma region. The inner electrode is simply a 1 mm thick disk with a 1 mm hole, and the outer one is 3.4 mm and possess a divergent conical exit channel through which plasma is expanded to the vacuum chamber. The mass distribution of the clusters can be influenced by increasing the thickness of the outer electrode. A lengthened electrode allows more time for "clustering" and generally results in a higher relative abundance of larger species. Source stability is better when the outer electrode is grounded while the inner one is negatively pulsed. The source is mounted on an XYZ translation system, which allows one to vary the solid angle sampled by the skimmer and thus a means to adjust the tolerance to the perpendicular velocity of the species in the beam. This gives control over the concentrations of species (both cold and hot) and their temperature characteristics during experiment. The typical distance was 50-70 mm. A typical mass distribution of the ionized species generated using the plasma discharge source is depicted in Figure 3.3. To be noted that in the mass spectrum only species with an ionization potential (IP) lower or equal to the energy of the ionizing laser are present.

3.1.2 Ablation source

This source (Figure 3.4) was designed specifically to produce large pure-carbon chains. It relies on conventional laser vaporization of graphite.[5–9] For the studies described in this thesis the graphite rod is replaced with a metal rod such as aluminium, magnesium and titanium. The rod is rotated and translated so that a fresh surface is continuously exposed to the laser (25 mJ/5 ns pulse of 532 nm Nd^{3+}:YAG, focused into 0.3 mm spot) which is fired to coincide with an inert gas or a gas mixture flow over the target area.

Depending on the metal target used or the stability of the vaporization source, the ablation wavelength was changed to 1064 nm (50 mJ/5 ns pulse) produced by

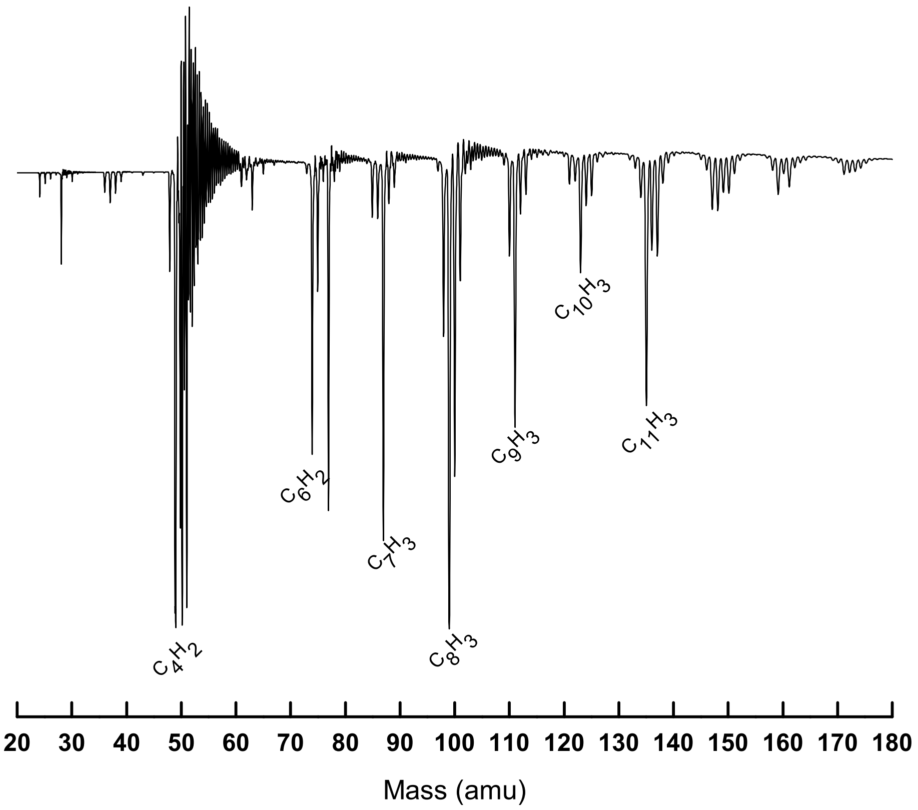

Figure 3.3: Mass spectrum of the species obtained in the discharge of a diacetylene/He mixture and ionized with 7.9 eV.

the Nd^{3+}:YAG laser. Vaporized metal atoms or clusters are swept through a 15 mm long and 3 mm diameter tube by a buffer gas maintained under 3-10 bar backing pressure and expanded into a vacuum chamber. At the laser spot on the metal rod the plasma is constricted at high buffer gas pressure. This makes clustering reactions in the plume of the metal vapor rapid compared with the diffusion speed resulting in the production of large molecules.[10] The distribution can be shifted down to smaller masses by shortening or removing the extender (effectively changing the length of the interaction region from 20 to 5 mm). This reduces the time available for clustering, and smaller masses generally are pro-

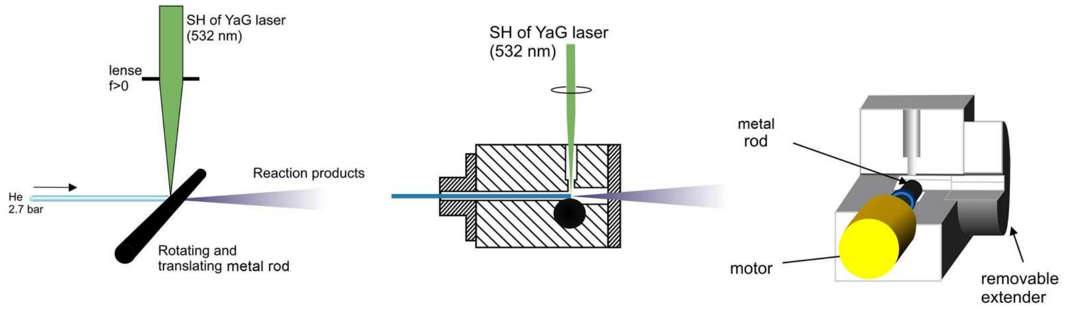

Figure 3.4: Rod ablation source

duced. Typically mixtures of CH_4, C_2H_2 or C_4H_2 in He, or Ne are used as a buffer gas. The pressure can be varied from 10 to 3.5 bar in order to optimize production of a specific molecule. However, this will also affect the reaction products cooling efficiency, which should be kept in mind when doing such optimizations. The mass distribution of metal-containing species (Al containing species) is depicted in Figure 3.5.

3.2 Vacuum system

The vacuum system of the experimental apparatus consisted of two differentially pumped chambers - a source chamber and a TOF mass spectrometry chamber, which are separated by a 2 mm diameter skimmer (Beam Dynamics). First, the source chamber consisted of a large stainless-steel cross-piece (25 cm in diameter and about 15 dm^3 capacity) evacuated by a large diffusion pump (Edwards, EO6K, 2000 l/s with a baffle cooled by water) being backed with a 80 m^3/h two-stage mechanical pump (Edwards E2M80). The pressure obtained in the chamber without operating the molecular source was at the level of $\sim 10^{-6}$ mbar, and typically $\sim 1.5x10^{-4}$ mbar when operating the source at 20 Hz with a backing pressure of 8 bar. The second chamber hosted the TOF mass spectrometer and ion detector, and required vacuum on the order of 10^{-6} mbar during operation. This requirement is achieved through the use of the turbo-molecular pumps: 210 l/s Pfeiffer TMU261 (backed by a 12 m^3/h mechanical pump Edwards RV12) is located near the region where the lasers interact with the molecules (extraction plates of TOF) and the second, smaller pump (Balzers TPH190, 190 l/s backed by 10 m^3/h mechanical

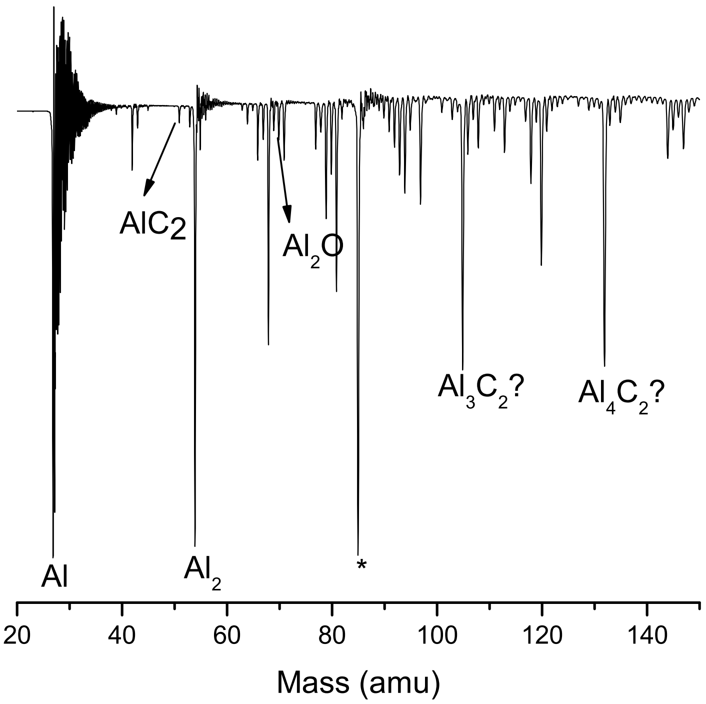

Figure 3.5: Products of aluminium ablation in the presence of an acetylene/He mixture and 7.9 eV ionization energy. *Impurity coming from the Al rod.

pump Pfeiffer DUO10) secures the MCP detector. A set of gauges are employed to indicate vacuum levels in the machine. Low vacuum, 1 bar-10^{-3} mbar, is monitored by Pirani-type gauges (Balzers TPR) whereas high vacuum in the range 10^{-3}-10^{-7} mbar is diagnosed by Penning ionization gauges (Balzers IKR251). The pressure readings of the gauge in the source chamber are sent via RS232 port to a computer for feedback control of the valve driver program[11] to keep the pressure constant during the experiment.

3.3 Light sources

The coherent light sources used in this experiment and the most appropriate combination to meet the energy constraints of the ionizing photons necessary to ionize the molecules of interest from their excited state are presented in Figure 3.6.

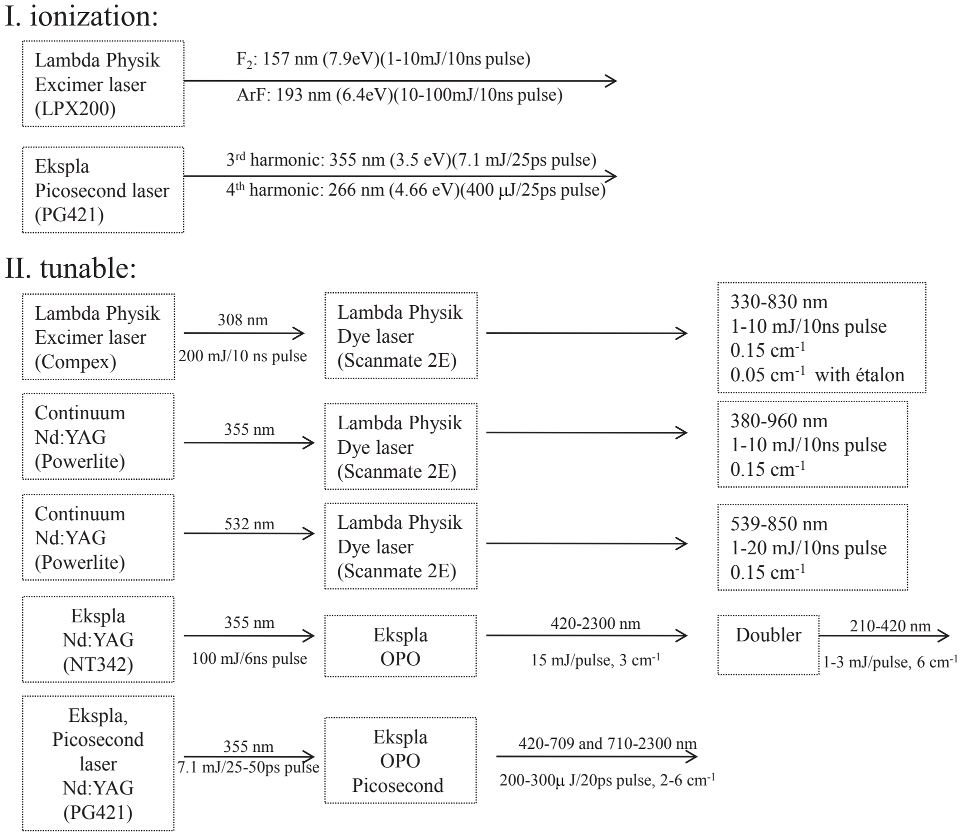

Figure 3.6: Laser systems used in different stages of the experimental work described in the thesis.

The tunable laser systems that provide the excitation photons include two dye lasers systems (Lambda Physik, Scanmate - 0.15 cm^{-1} bandwidth and 0.05 cm^{-1} with an intracavity étalon) for high resolution scans pumped by an excimer laser (Lamda Physik, COMPeX, operating at 308 nm) and the second/third harmonic of an Nd^{3+}:YAG laser (Continuum, Powerlite), respectively. The laser system used for a broad band (∼5 cm^{-1} bandwidth) survey is an optical parameter oscillator

(OPO, Ekspla, NT 342) pumped by the third harmonic generated from a build-in Nd^{3+}:YAG rod. The light from the dye laser covers the region 330-850 nm with typical output powers of a few mJ. The tunable UV radiation from 210-350 nm is obtained by doubling the output of a dye laser using a BBO crystal. The OPO systems provides photons from 210 up to 2100 nm with output powers between few mJ up to tens of mJ in the visible region. The photons for the ionizing step are delivered from an excimer laser (Lamda Physik, LPX200, operating at F_2 with 157 nm (7.9 eV) or ArF with 193 nm (6.4 eV)).

A picosecond laser system (Ekspla PL2143 Series/PG421) has been proposed as a photon source for both excitation and ionization steps. The laser system was first tested as an ionization source and mass spectra showing products of graphite ablation as well as other metal targets were successfully recorded. In the case of graphite ablation, fragmentation products of larger C_n clusters were observed using ionization energies of 4.7 eV (266 nm) and 3.5 eV (355 nm). In addition the electronic spectrum of AlO was successfully reproduced using the picosecond pump-probe setup.

3.4 Time of flight mass spectrometer

Mass spectrometers use the difference in mass-to-charge ratio (m/e) of ionized atoms or molecules to separate them from each other. Mass spectrometry is therefore useful for quantization of atoms or molecules and also for determining chemical and structural information about molecules. Molecules have distinctive fragmentation patterns that provide structural information to identify structural components.

The general operation of a mass spectrometer is:

1. create gas-phase ions
2. separate the ions in space or time based on their mass-to-charge ratio
3. measure the quantity of ions of each mass-to-charge ratio

A time-of-flight (TOF) mass spectrometer uses the difference in transit time through a drift region to separate ions of different masses and is the simplest form of mass analysis.

In Figure 3.7, a schematic diagram for a two-stage accelerating linear TOF mass spectrometer[1] used in the apparatus is given.

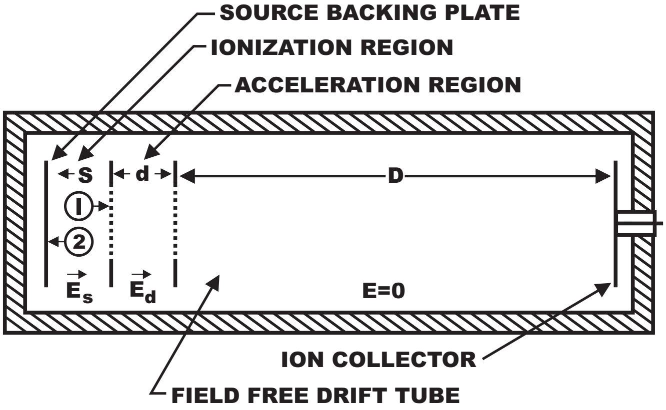

Figure 3.7: Basic geometry of a Wiley-McLaren time-of-flight mass spectrometer.[1]

The region between the first two grids of length (s) is the first accelerating stage with an electric field $E_s=U_s/s$. The region of length d is the second accelerating stage with an electric field $E_d=U_d/d$. The region between last grid and the ion collector is a free-field region (D). Let a charged particle (ion) with mass=m, charge=q and velocity v=0 be located at a distance s_0 from the second grid in the first acceleration stage. The force applied to the ion is F, while a_1 and a_2 are the accelerations of the ion in electric fields E_s and E_d, respectively.

$$F = ma_1 = qE_s \tag{3.1}$$

$$a_1 = \frac{qE_s}{m} \tag{3.2}$$

After time t_1, the ion travels a distance s_0 and moves into the second accelerating electric field E_d, then

$$v_2 - v_1 = a_2(t_2 - t_1) \Longrightarrow t_2 = t_1 + \frac{v_2 - v_1}{a_2} = t_1 + \frac{(v_2 - v_1)md}{qU_d} \tag{3.3}$$

From the law of energy conservation,

$$1/2mv_1^2 = qU_{s_0} \tag{3.4}$$

and

$$U_{s_0} = U_s \frac{s_0}{s} \tag{3.5}$$

$$s_0 = \frac{1}{2} a_1 t_1^2 \tag{3.6}$$

Using the three equations above the time t_1 that the ion travels in the first acceleration stage can be defined:

$$t_1 = \sqrt{\frac{2s_0}{a_1}} = \sqrt{\frac{2m}{q}} \cdot \sqrt{\frac{s_0 s}{U_s}} \tag{3.7}$$

In order to determine the total time-of-flight t, the time t_2 and t_3, defined as the time in the second acceleration stage and in the drift tube, respectively need to be evaluated. The ion speed in the first and second acceleration stage id defined:

$$v_1 = \sqrt{\frac{2qU_{s_0}}{m}} \tag{3.8}$$

Energy conservation law for the second stage gives:

$$v_2 = \sqrt{\frac{2q(U_{s_0} + U_d)}{m}} \tag{3.9}$$

When the ions arrive at the ion collector after a flight distance D in the free-field region, in the time $t_3=\frac{D}{v_2}$, the total time-of-flight t is:

$$t = t_2 + t_3 = t_2 + \frac{D}{\sqrt{U_{s_0} + U_d}} \cdot \sqrt{\frac{m}{2q}} \tag{3.10}$$

where,

$$t_2 = t_1 + \frac{mU_d}{qd} \cdot \sqrt{\frac{2q}{m}} \cdot (\sqrt{U_{s_0} + U_d} - \sqrt{U_{s_0}}) \tag{3.11}$$

Thus, the final time-of-flight until ions reach the collector is:

$$t = \sqrt{\frac{2m}{q}} \cdot \sqrt{\frac{s_0 s}{U_s}} + \sqrt{\frac{2m}{q}} \cdot \frac{d}{U_d} \cdot (\sqrt{U_{s_0} + U_d} - \sqrt{U_{s_0}}) + \sqrt{\frac{2m}{q}} \cdot \frac{D/2}{\sqrt{U_{s_0} + U_d}} \tag{3.12}$$

and may be written as:

$$t = const \cdot \sqrt{\frac{m}{q}}, \tag{3.13}$$

The *const* is dependent on s_0, s, d and D as well as on the electric potentials applied to the grids. If the initial velocity of the ion is not zero, t will not be strictly linear dependent on $(m/q)^{1/2}$. The ions may have non-zero initial velocity along the flight tube and the ions are not at all formed at the same point. Both of these factors will lead to a loss of TOF mass spectrometer resolution. The two-stage accelerating field compensates for the space focusing. The position of the space focus is a function of the ratio between extraction and acceleration fields. Keeping the total voltage fixed by powering all grids via a potential divider and varying the ratio allows one to match the space focus with the position of the detector without changing the flight times and hence, the mass calibration. Higher order space focusing can be achieved by using more then two field regions.

The double stage acceleration scheme can not compensate for the initial kinetic energy distribution of ions. A double field system brings the ions to their maximum energies in about 5% of the flight time compared with 50% in the single field. To further improve the resolution of the mass spectrometer by energy focusing a reflectron can be introduced in route of ions to the detector. The reflectron, originally implemented by Karataev *et al.*, is an ion focusing device used to both lengthen the flight time and decrease the temporal spread of ions with the same mass reaching the detector. It is composed of two turning electric fields located at the vertex of an acute angle (18°) in the flight tube. For a given mass, the ions with greater velocity penetrate further into the reflectron electric field before stopping, and reversing their motion, moving down the second flight tube, oriented at 18 degrees from normal. Because they penetrate more deeply into the reflectron field, these faster ions spend more time turning around than the slower ions. In the end the faster ions catch up once again with the slower ones, coming to a spatial focus at the detector.

In the apparatus used in this thesis the introduction of reflectron was not necessary because the mass resolution of the TOF-MS is ~ 900, enough to separate ions different by 1 mass unit. The ion optics of the TOF mass spectrometer consists of three parts. The first part is the ion repeller and extractor. It must be noted that the neutrals prior to ionize are traveling with the beam velocity of the carrier gas. If this velocity component is left unchecked, then the ions will drift away from the flight tube, most likely collide against the walls and go undetected. An additional feature is required to neutralize the original velocity due to supersonic expansion, which is perpendicular to the flight tube. The added feature is a pair of deflector plates to steer the ion beam in the x and y directions.

3.5 Ion detection

The ion detector used in the experiment is a microchannel plate (MCP) detector. A microchannel plate (Figure 3.8) consists of an array of glass capillaries (10-25 μm inner diameter) that are coated on the inside with a electron-emissive material. The capillaries are biased at a high voltage and like the channeltron, an ion that strikes the inside wall one of the capillaries creates an avalanche of secondary electrons. This cascading effect creates a gain of 10^3 to 10^4 and produces a current pulse at the output. Two plate are stacked and connected in series (so-called Chevron configuration) so that the overall gain is 10^6-10^7. The MCP detectors provide high temporal resolution, direct conversion, high physical charge amplification, low noise, and pulse-counting capabilities. The fast response time (in the 100 ps range) and flat geometry (effective area diameter of 25 mm) are particularly important for TOF mass spectrometric applications.

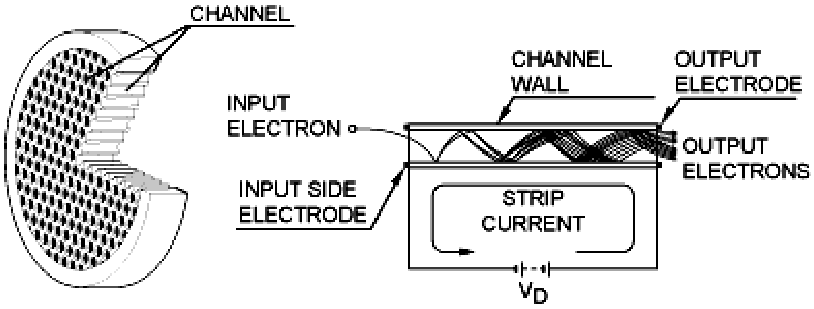

Figure 3.8: Schematic of microchannel plate detector.[12]

The detector is operated for positive ion detection (for the electrical arrangement see Figure 3.9). Following impact by the positive ion the first plate produces an electron output which is subsequently amplified to more electrons to provide a gain on the ion signal. The detector gain is governed by the potential applied to the plates (0.1 kV per plate). The gain selected is determined by the intensity of the ion signal observed on the oscilloscope and signal saturation is avoided by lowering the detector voltage when necessary.

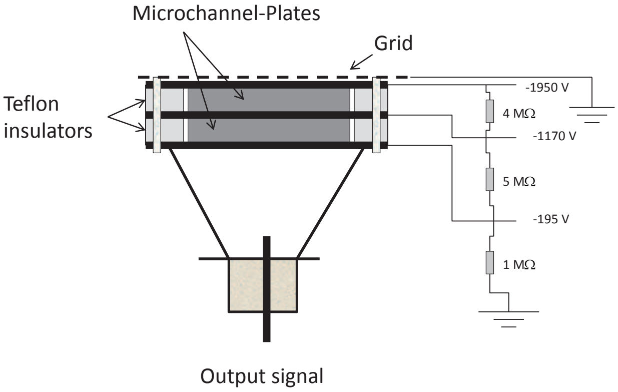

Figure 3.9: Schematic of microchannel plate detector for positive ions.

The detection efficiency [1] of the MCP varies considerably based on the velocity of the impinging ions. For positive ions with acceleration potential of $\sim 3\,\mathrm{kV}$ the efficiency is approximately 40%.[13] The output of the detector is an electron current that is amplified by a fast, low-noise pre-amplifier (Ortec) and transmitted through a BNC cable to the oscilloscope (LeCroy LT342, 500 MHz, 2 channels) where the accumulation and digitalization of the data takes place.

3.6 Electrical arrangement and synchronization of the REMPI setup

As seen in the Figure 3.1 the REMPI setup consist of a source, extraction and detection chambers. The experiment is operated at 10 or 20 Hz controlled by the

---

[1] detection efficiency is defined as a measure of the ability of an incident particle to induce secondary electrons in a MCP detector.

central computer which generates an initial trigger TTL signal at time T_0. The computer uses T_0 to trigger the pulsed valve and a digital delay/pulse generator system via a parallel port. The opening of the pulsed valve is automatically adjusted by the central computer ($250+\Delta t\,\mu s$) based on the feedback signal from the pressure reader that gives the pressure in the source chamber. The central computer reads this pressure via a RS232 port. The central computer and the digital delay/pulse generator (Stanford Research Inc.,DG 535, 4-channels) provide the synchronization of all systems as described in Figure 3.10.

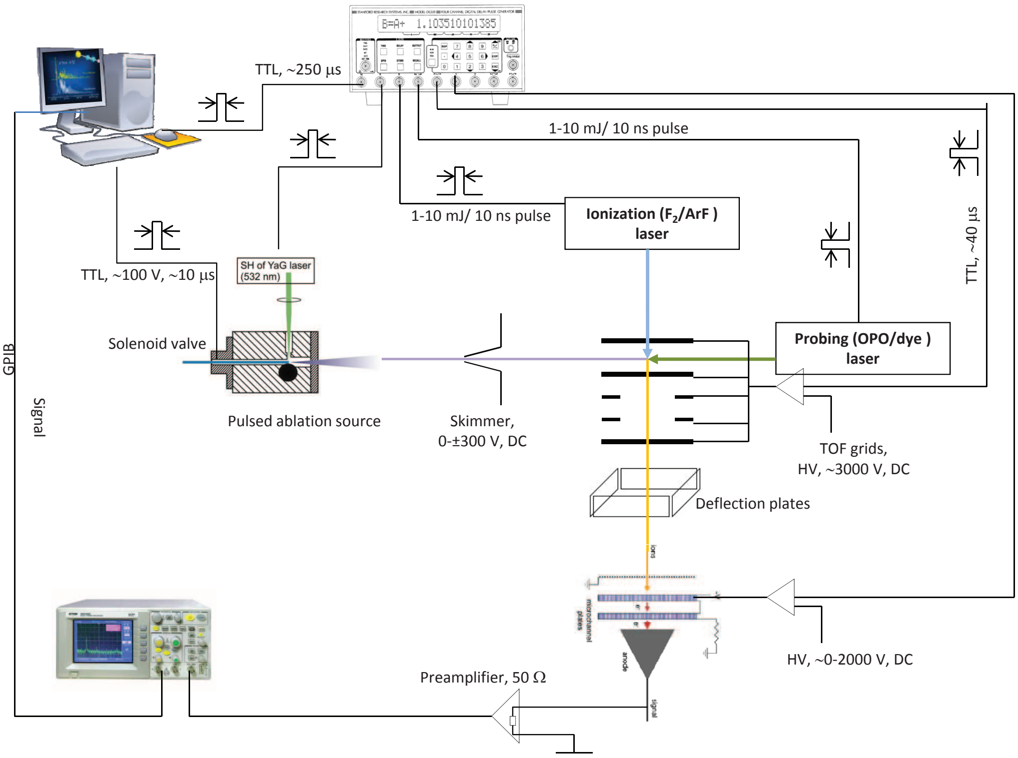

Figure 3.10: Electrical arrangement of the experiment.

The gas pulse with a width of $\sim 250\,\mu s$ is generated at T_0. After a delay of $\sim 500\,\mu s$, the pulse of carrier gas arrives in the vaporization region and the ablation laser is fired. After a $\sim 200\,\mu s$ delay, the beam of neutral molecules moves into the photoionization region where the two lasers are fired, the probing laser few nanoseconds before the ionization laser. After a $\sim 2\,\mu$s delay, the ions are extracted by a pulsed electric field ($\sim 40\,\mu$s duration). The electric field is pulsed to reduce the background noise on the MCP from photoelectrons produced by mainly secondary processes. The oscilloscope is triggered at the same time as the extraction pulse of the TOF.

3.7 Data handling

Typically 30 laser shots were averaged by the oscilloscope before being transmitted via a GPIB interface to a PC computer. The whole data acquisition process is controlled by a programm written in LabView. The program can work in two main modes: mass spectrometer and REMPI spectrometer. The first mode allows the user to monitor the evolution of the mass spectrum in near real-time. The computer that controls the whole experiment interrogates the oscilloscope in cycle, requesting it to digitize and average a set number of laser shots, each of which is followed by a complete TOF cycle. The resulting waveform can replace the previous one on the screen of the PC or can be added to it when further signal accumulation is required. The mass calibration is defined by the operator through an empirical assignment of two time delays to the two masses. The calibration entered can be used immediately to convert the mass spectrum's abscissa axis to mass-to-charge (m/q) units. Assessment of a correct calibration is usually done when all observable mass-peaks are of integer value.

The peak of interest can be marked and "gated" manually or automatically, based on the $M_0+i*M_1+j*M_2$ template (expression). This is especially convenient when a certain family of molecules (for example like $C_{2n}H$) is the focus of the study. In the "REMPI spectrometer" mode the program records the dependence of the mass-spectrum on the laser wavelength. The master computer drives the scanning laser to the next wavelength, programs the oscilloscope on certain given number of accumulation cycles, and downloads the acquired waveform. The integrated intensities of the gated peaks are calculated and stored. The cycle is looped and the laser is tuned to the next wavelength. The mass-peak area is proportional to the ion current of the ions with a specific mass, and, in turn, to the ionization efficiency of the corresponding neutral species. The variation of the peak area versus laser wavelength provides the REMPI spectrum of the molecule.

Bibliography

[1] W. C. Wiley and I. H. McLaren, Rev. Sci. Instrum. **26**, 1150 (1955).

[2] Y. Ohshima and Y. Endo, J. Mol. Spectrosc. **153**, 627 (1992).

[3] K. R. Comer and S. C. Foster, Chem. Phys. Lett. **202**, 216 (1993).

[4] J. Remy, L. Biennier, and F. Salama, IEEE Transactions On Plasma Science **33**, 554 (2005).

[5] D. E. Powers et al., J. Phys. Chem. **86**, 2556 (1982).

[6] P.Milani and W. A. Deheer, Rev. Sci. Instrum. **61**, 1835 (1990).

[7] T. G. Dietz, M. A. Duncan, D. E. Powers, and R. E. Smalley, J. Chem. Phys. **74**, 6511 (1981).

[8] K. Laihing, R. G. Wheeler, W. L. Wilson, and M. A. Duncan, Rev. Sci. Instrum. **87**, 3401 (1987).

[9] E. F. Rexer, M. P. Joshi, R. L. DeLeon, P. N. Prasad, and J. F. Garvey, Rev. Sci. Instrum. **69**, 3028 (1998).

[10] J. R. Heath et al., J. Am. Chem. Soc. **109**, 359 (1987).

[11] T. Motylewski, *Cavity ringdown spectroscopy of transient species.*, PhD thesis, Basel University, 2001.

[12] DelMarVentures, Microchannel Plates and Microchannel Plates Detectors, http://www.sciner.com/MCP/MCP.htm.

[13] Burle Industries Inc., Scientific detectors products: Technical Brief no2 - Detection Efficiency, http://www.burle.com/dettechbrief2.htm.

4 Gas phase $1^1\Sigma_u^+ \leftarrow X^1\Sigma_g^+$ Electronic Spectra of Polyacetylenes $HC_{2n}H$, n=5-7

4.1 Abstract

The $1^1\Sigma_u^+ \leftarrow X^1\Sigma_g^+$ system in polyacetylenes $HC_{2n}H$ (n=5-7) has been observed for the first time in the gas phase. The UV absorption spectra of these chains were recorded using the resonant two-color two-photon ionization technique. A strong vibrational progression corresponding to the acetylenic stretching mode in the excited state has been observed. The absorption energy showed an inverse dependence on the chain length. The relaxation process of the $1^1\Sigma_u^+$ excited state has been discussed.

4.2 Introduction

The atmosphere of Saturn's moon, Titan, is mainly composed of N_2 and CH_4.[1–3] The complex chemistry initiated by the photolysis of these gases has attracted substantial interest in the last two decades.[4–6] Titan is the only other object in the solar system with an atmosphere resembling that of the early earth. This similarity has intrigued scientists to better understand the chemical processes that eventually led to the origin of life on earth.[7] The other interesting feature of Titan is the thick organic haze layer that appears as an orange fog obscuring its surface. Several photochemical models[8–10] have been developed to gain insight into the various pathways leading to the formation of haze particles. It has been understood that these aerosol particles are the end products of the aggregation of small molecules such as, C_2H_2, C_2H_4, C_4H_2, C_6H_6, and HCN, which have been detected on Titan. Polyacetylenes, cyanopolyacetylenes, and polycyclic aromatic hydrocarbons (PAHs) are considered as precursors to the formation of aerosols. In the case of polyacetylenes, C_4H_2 is the only member to be detected on Titan thus far. However, the presence of longer members cannot be ruled out. In terms of laboratory measurements, UV absorption spectra of known polyynes have been helpful in obtaining absorption cross sections, which were then used to calculate photolysis rates and deduce relative abundances of longer members in the series.[11]

In this chapter the electronic spectra corresponding to the $1^1\Sigma_u^+ \leftarrow X^1\Sigma_g^+$ band system in the polyacetylene chains $HC_{10}H$, $HC_{12}H$, and $HC_{14}H$, observed for the first time in the gas phase, is presented. The spectra were recorded using the resonant two-color two-photon ionization (R2C2PI) technique. Gas phase studies of the above band system in the lower and higher homologues $HC_{2n}H$ (n=1-4)[12] and $HC_{2n}H$ (n=8-13)[13] are available. They also have been measured in solution (n=5-10,12)[14] and in neon matrices (n=6-12).[15] However for n=5, 6 and 7 only the forbidden $A^1\Delta_u^+ \leftarrow X^1\Sigma_g^+$ band system has been observed thus far in the gas phase.[16]

4.3 Experimental

Details of the experimental setup can be found in the experimental section of this thesis. In brief, an electric discharge of a gas mixture pulse (1% diacetylene in He) followed by a supersonic expansion into vacuum produced $HC_{2n}H$ in sufficient yield. The contents of the jet-cooled molecular beam were collimated by a 2 mm skimmer and allowed to enter the extraction region of a pulsed time-of-flight mass spectrometer. The R2C2PI spectroscopy exposing the molecular beam to the output of a tunable OPO ($\sim 5\,\mathrm{cm}^{-1}$ bandwidth) and subsequently to an F_2 (157 nm) excimer laser. The resulting ions were extracted in a two stage acceleration setup and detected using a microchannel plate detector. Excited state lifetimes were measured by recording the ion signal as a function of the delay between the excitation and ionization lasers and fitting resulting decay curves to an exponential function.

4.4 Results and discussion

The even membered polyacetylenes, $HC_{2n}H$, are closed shell species with a $^1\Sigma_g^+$ ground state, which is derived from either a π_g^4 or a π_u^4 electronic configuration. Promotion of an electron $\pi_g \rightarrow \pi_u^*$ or $\pi_u \rightarrow \pi_g^*$ gives rise to the $^{1,3}\Sigma_u^+$, $^{1,3}\Sigma_u^-$, and $^{1,3}\Delta_u$ excited states. According to the dipole selection rules, a $^1\Sigma_u^+$ excited state can be accessed from a $^1\Sigma_g^+$ ground state and will therefore carry most of the oscillator strength. Figure 4.1 displays the electronic spectra assigned to the $1^1\Sigma_u^+ \leftarrow X^1\Sigma_g^+$ transition in linear polyacetylenes, $HC_{2n}H$ (n=5,6 and 7). Each spectrum is dominated by a strong vibrational progression corresponding to the excitation of the $-C \equiv C-$ stretching mode in the excited state. Table 4.1 provides a list of the band positions along with the known experimental (neon matrix and solution)[14,15] and theoretical[17] absorption wavelength of this band system.

As seen in Figure 4.1, the $1^1\Sigma_u^+ \leftarrow X^1\Sigma_g^+$ band system shifts to the red with increasing chain length. Previous studies have shown that a plot of the wavelength vs the number of carbon atoms, exhibits a sublinear dependence.[13] This has been attributed to the localization of the π electron cloud in linear polyyenes. DFT calculations on the $^1\Sigma_g^+$ ground state shown that these molecules possess a linear geometry and exhibit a single-triple bond length alternation.[18,19] It can be inferred, on the basis of the spectral analysis of the $^1\Sigma_u^+$ excited state that the acetylenic stretching frequency decreases with increasing chain length, suggesting greater delocalization of the π electron cloud and therefore a less pronounced bond length alternation in the excited state. Theoretical investigation on the $^1\Sigma_u^+$ excited-state geometries in the longer chains have not been reported thus far. However, a CASSCF study[19] on the smaller members HC_4H, HC_6H, and HC_8H indicates that the bond length equalizes in the middle of the chain and therefore a cumulenic structure for the excited state.

The oscillator strength (f) of the $1^1\Sigma_u^+ \leftarrow X^1\Sigma_g^+$ transition in $HC_{2n}H$ increases with the chain length. For n=5, 6, and 7 the theoretical f value around 6, 7, and 8, respectively.[17] This corresponds to $\sim$0.1 ns lifetime of the $^1\Sigma_u^+$ state, assuming that the fluorescence quantum yield is unity. However, the width of the observed bands indicates a much shorter lifetime. The width obtained from a Lorentzian fit of the recorded peaks is in the range of 300-500 cm^{-1}. This corresponds to

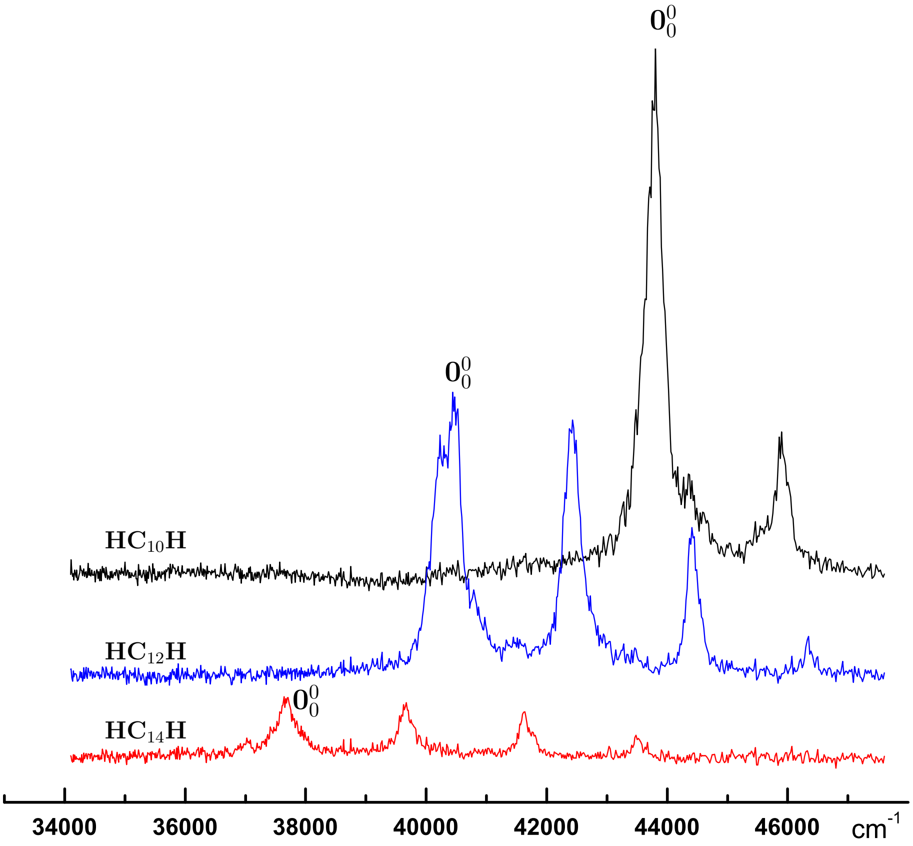

Figure 4.1: $1^1\Sigma_u^+ \leftarrow X^1\Sigma_g^+$ electronic absorption band system of polyacetenes, $HC_{2n}H$ (n=5-7).

a lifetime in the sub picosecond time scale. Thus intersystem crossing is the dominant decay pathway of the excited electronic state. The decay characteristics of the excitation-ionization process were measured by varying the pump-probe delay. The exponential decay gave a time constant in the range of 0.2-4 μs. This long lifetime corresponds to the slowest step in the excitation-ionization scheme. The prepared $^1\Sigma_u^+$ excited state undergoes rapid internal conversion to higher vibrational levels of the $^1\Sigma_g^+$ ground state or gets trapped in a long-lived excited state, which could be a $^3\Sigma_u$ or a $^3\Delta_u$ state arising from the same excited state configuration. The molecule then absorbs a second photon from this intermediate state producing ions which are detected. The microsecond time constants appear to be the lifetime of this latter state.

	$\tilde{\nu}$ (cm^{-1})				$\Delta\nu$	
	gas phase[a]	neon matrix[b]	solution[c]	theory[d]	(cm^{-1})	assignment
$HC_{14}H$	37667	36377	33898	38098	0	0^0_0
	39644				1977	$\nu_{C\equiv C}$
	41622				3954	$2\nu_{C\equiv C}$
	43485				5818	$3\nu_{C\equiv C}$
$HC_{12}H$	40371	38971	36563	40876	0	0^0_0
	42406				2036	$\nu_{C\equiv C}$
	44426				4055	$2\nu_{C\equiv C}$
	46350				5979	$3\nu_{C\equiv C}$
$HC_{14}H$	43784		39920	44345	0	0^0_0
	45906				2122	$\nu_{C\equiv C}$

Table 4.1: Observed band positions in the $^1\Sigma_u^+ \leftarrow X^1\Sigma_g^+$ electronic transition of $HC_{2n}H$ (n=5-7). [a] This work. [b] Reference 15. [c] Reference 14. [d] Reference 18.

4.5 Conclusion

The gas phase spectrum of longer polyacetylenes, $HC_{2n}H$ (n=5-7) presented here provides the means to identify these molecules remotely by UV spectroscopy in environments such as the atmosphere of Titan. It is generally understood that the formation of polyacetylenes on Titan is initiated by the photodissociation of C_2H_2 creating a C_2H radical that reacts with another C_2H_2 molecule, producing C_4H_2. The longer chains also photodissociate, forming $C_{2n}H$ radicals that once again react with acetylene, creating $HC_{2n}H$ chains. In a recent review on polyynes,[11] the authors calculated synthetic absorption cross sections using analytical expressions for the origin and the acetylenic stretching frequencies of the $^1\Sigma_u^+ \leftarrow X^1\Sigma_g^+$ system in these chains. The absorption cross section was used to derive photolysis rates and predict relative abundances ($HC_{2n}H/HC_2H$) of longer species. The spectrum presented here provides experimental verification of the UV absorption spectral region in $HC_{2n}H$ (n=5-7). This information can be used to obtain improved absorption cross sections that can be extended to predict the relative abundances of these species with better accuracy.

Bibliography

[1] G. F. Lindal et al., Icarus **53**, 348 (1983).

[2] G. R. Smith et al., J. Geophys. Res. **87**, 1351 (1982).

[3] J. H. Waite et al., Science **308**, 982 (2005).

[4] C. Sagan, W. R. Thompson, and B. N. Khare, Acc. Chem. Res. **25**, 286 (1992).

[5] D. W. Clarke and J. P. Ferris, Icarus **127**, 158 (1997).

[6] S. Lebonnois, E. L. O. Bakes, and C. P. McKay, Icarus **159**, 505 (2002).

[7] D. W. Clarke and J. P. Ferris, Origins Life Evol. Biosphere **27**, 225 (1997).

[8] Y. L. Yung, M. Allen, and J. P. Pinto, Astrophys. J. Suppl. Ser. **55**, 465 (1984).

[9] D. Toublanc et al., Icarus **113**, 2 (1995).

[10] E. H. Wilson, S. K. Atreya, and A. Coustems, J. Geophys. Res. **108**, 8 (2003).

[11] A. Jolly et al., J. Quant. Spectrosc. Radiat. Transfer **109**, 2846 (2008).

[12] J. E. Kloster, H. J. Haink, and H. Christen, Helv. Chim. Acta **57**, 1731 (1974).

[13] T. Pino, H. B. Ding, F. Güthe, and J. P. Maier, J. Chem. Phys. **114**, 2208 (2001).

[14] R. Eastmond, D. R. M. Walton, and T. R. Johnson, Tetrahedron **28**, 4601 (1972).

[15] M. Grutter, M. Wyss, J. Fulara, and J. P. Maier, J. Chem. Phys. A **102**, 9785 (1998).

[16] H. Ding, T. W. Schmidt, T. Pino, F. Güthe, and J. P. Maier, Phys. Chem. Chem. Phys. **5**, 4772 (2003).

[17] A. Scemama, P. Chaquin, M. C. Gazeau, and Y. Benilan, Chem. Phys. Lett. **361**, 520 (2002).

[18] A. Scemama, P. Chaquin, M. C. Gazeau, and Y. Benilan, J. Phys. Chem. A **106**, 3828 (2002).

[19] C. J. Zhang, Z. X. Cao, H. S. Wu, and Q. R. Zhang, Int. J. Quantum Chem. **98**, 299 (2004).

5 Gas phase electronic spectrum of linear AlCCH

5.1 Abstract

The electronic spectrum of the aluminum containing species AlCCH has been detected in the gas phase in the region 315-355 nm. The experiment used a mass selective resonant two-color two-photon ionization technique coupled to a laser ablation source. Structures of the AlCCH isomers have been optimized using density functional theory and the excitation energies to the low-lying electronic excited states have been calculated. Based on the analysis of the observed rotational structure and the theoretical data, the spectrum is assigned to the $A\ ^1\Pi \leftarrow X\ ^1\Sigma^+$ electronic transition of linear AlCCH. The vibronic band system is complicated by the Renner-Teller effect in the excited state. The assignment yields $\nu_4^{''}$=516.4 cm^{-1} for the stretching mode in the ground state and $\nu_4^{'}$=654.5 cm^{-1} in the $A\ ^1\Pi$ state. Molecular constants determined from the rotational analysis are $B_0^{''}$=0.16487(14), $B_0^{'}$=0.17845(13) and $T_0 = 28755.04$ cm^{-1}. The experimental and theoretical data indicate a shorter Al–C bond in the $A\ ^1\Pi$ excited than the $X\ ^1\Sigma^+$ ground state.

5.2 Introduction

Over the past thirty years of radio astronomy, a great deal has been learned about interstellar molecules and their chemistry. Despite this progress, there are still areas of molecular astrophysics where challenges remain. One of these concerns the chemistry and distribution of molecules containing metals. Identifying the carriers of these elements in the interstellar medium, including circumstellar gas, is crucial for the evaluation of dust grain composition, ionization balance, mass loss and elemental depletions from evolved stars.

To date, nine molecules containing the metals aluminum, magnesium, sodium, and potassium have been discovered toward circumstellar envelopes of carbon-rich stars such as IRC + 10216 and CRL 2688.[1] These species fall into two classes: the cyanides MgNC,[2] MgCN,[3] NaCN,[4] KCN, and AlNC[5] and the halide compounds AlCl, AlF, KCl, and NaCl.[6,7] It seems that the most common metallic element in IRC + 10216 is aluminum.[8] At the same time stable species such as CO, C_2H_2 and HCN have been detected in this carbon-rich object.[9,10] It was postulated that these molecules photodissociate in the star's outershell resulting in the formation of C_2H, C_4H and C_6H radicals.[11] The products could react with Al atoms to form AlCCH, a molecule with potential interest in astrophysics.

However, how metal species bond to hydrocarbon species has not been extensively explored, at least from a spectroscopic point of view. Reaction products of metal atoms and hydrocarbon molecules are important for understanding chemisorption and catalytic processes. A number of metal atom reactions with acetylene have already been studied.[12–15] Aluminum adducts with acetylene have been examined using *ab initio* calculations, and a number of stable Al-C_2H_2 isomers have been predicted.[16–18] The related reaction between laser ablated Al atoms and acetylene has been examined using IR matrix isolation spectroscopy.[19] It was found that Al atom and C_2H_2 form the AlC_2H_2 complex. This relaxes in the matrix to form HAlCCH and under photolysis produces the AlCCH molecule.

Several gas phase studies of the electronic spectra of metal-ligand radicals in the gas phase such as MgCCH, CaCCH and SrCCH have been reported.[20–22] All three radicals exhibit an $A\ ^2\Pi \leftarrow X\ ^2\Sigma^+$ electronic transition in the visible spectral range and it could be concluded that replacing a H atom with a metal atom results in a linear metal-acetylide species.

In this article the electronic spectrum of AlCCH is presented and analyzed for the first time. The experimental technique used is the two-color two-photon laser ionization in a supersonic molecular beam.

5.3 Experiment

The experimental instrument consists of a molecular beam combined with a mass spectrometer.[23] The beam was produced by laser ablation of an aluminum rod in the throat of a pulsed supersonic expansion of 1% acetylene in helium or neon at a backing pressure of ∼ 10 bar using a pulsed Nd:YAG laser for ablation (532 nm, 30 mJ /pulse). The carrier gas and products of ablation flowed through a 15 mm long, 3 mm diameter channel, which then expands into a vacuum chamber. This was skimmed to form a collimated beam of neutral and ionized molecules. Ions were then removed by a perpendicular electric field before entering the ionization region of a Wiley-McLaren time-of-flight mass spectrometer,[24] where the molecules were irradiated with a pulse of tunable ultraviolet-visible radiation. Following a short delay the molecules were exposed to a pulse of 193 nm photons from an ArF excimer laser. The combination of the UV and the 193 nm photons was sufficient to ionize AlCCH. The signal from the microchannel plate ion-detector was sent to a fast oscilloscope followed by data acquisition.

The resonant two-color two-photon (R2C2PI) spectrum of AlCCH was investigated over the 300-700 nm range. Excitation photons were provided from an OPO system (∼ 5 cm^{-1} band-width) for the vibronic survey scans. A pulsed dye laser was used (∼ 0.1cm^{-1} , ∼ 5 mJ /pulse) for the rotationally resolved work. Calibration was accomplished using a wavemeter for the vibronically resolved work. The dye laser was calibrated with optogalvanic spectra obtained from a Fe/Ne hollow cathode lamp.

5.4 Theoretical calculations

Ab initio calculations were carried out with the GAUSSIAN 98 suite of programs.[25] Geometry optimizations and energy calculations for two isomers Fig. 5.1 have been performed at the B3LYP/aug-cc-pvtz level of theory. The calculated harmonic vibrational frequencies, rotational constants and dipole moments in the ground states of linear-AlCCH and cyclic-HAlCC are listed in Tables 5.1 and 5.2.

The results are in agreement with those obtained with the CASSCF method.[19] These show that the linear structure is more stable than the cyclic one by 41.1 kJ mol^{-1}. Calculations for other isomers, such as HAlCC, bent-AlCCH, have

Frequencies	AlCCH ($C_{\infty v}$)	HAlCC (C_{2v})
ν_1	3438 (σ)	2028 (a_1)
ν_2	2065 (σ)	1807 (a_1)
ν_3	733 (π)	754 (a_1)
ν_4	503 (σ)	522 (b_2)
ν_5	132 (π)	459 (b_1)
ν_6		415 (b_2)

Table 5.1: *Ab initio* calculated harmonic vibrational frequencies (cm^{-1}) for linear and cyclic isomers in their ground electronic states at the DFT-B3LYP/aug-cc-pvtz level.

been carried out and indicate that HAlCC is unstable and converges to cyclic-HAlCC, while bent-AlCCH leads to the linear-AlCCH.

	AlCCH ($C_{\infty v}$)	HAlCC (C_{2v})
A/cm^{-1}		1.5571
B/cm^{-1}	0.16385	0.3668
C/cm^{-1}		0.3034
D_e/Debye	0.549^a	4.53^a
E/a.u.	-319.216	-319.153
ΔE/eV	0.0	1.71

Table 5.2: Calculated energies, rotational constants and dipole moments in the ground states for linear and cyclic isomers at the DFT-B3LYP/aug-cc-pvtz level. ^{a} Dipole moment along the C_∞ and C_2 axis, respectively.

The electronic configuration of the ground state linear-AlCCH is $\ldots[8\sigma]^2[3\pi]^4[4\pi]^4[9\sigma]^2$, $X\ ^1\Sigma^+$ and $\ldots[3b_2]^2[2b_1]^2[7a_1]^2[8a_1]^2$, $\tilde{X}\ ^1A_1$ for the cyclic-HAlCC. *Ab initio* calculations of the excited states were undertaken using time-dependent DFT theory.[26] The ground state of linear-AlCCH is dominated by the $\ldots 4\pi^4 9\sigma^2$ electronic configuration. Promotion of the electron from $9\sigma \rightarrow 5\pi$ leads to the $\ldots[8\sigma]^2[3\pi]^4[4\pi]^4[9\sigma]^1[5\pi]^1$ configuration, resulting in the $A\ ^1\Pi$ first electronic excited state. The $8a_1 \rightarrow 4b_2$ excitation for the cyclic-HAlCC leads to the $\ldots[3b_2]^2[2b_1]^2[7a_1]^2[8a_1]^2[4b_2]^1$ configuration, resulting

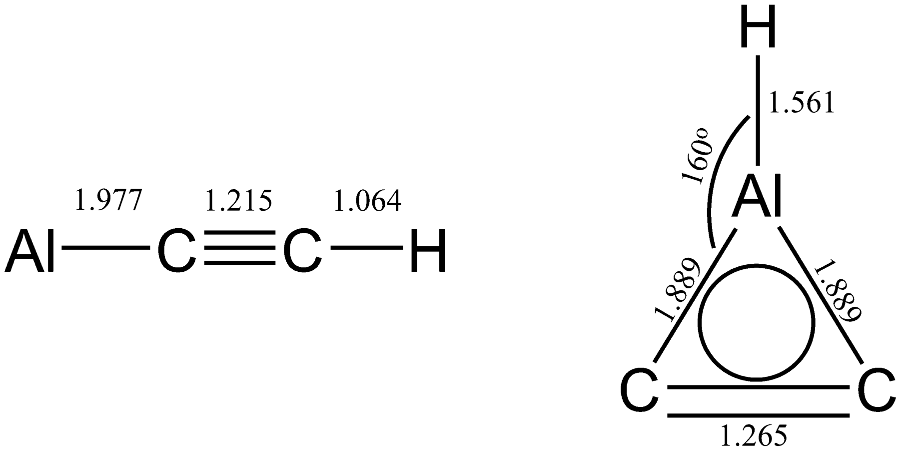

Figure 5.1: Calculated ground state structures of AlCCH using DFT-B3LYP/aug-cc-pvtz level of theory (bond-lengths in Å).

in the $\tilde{A}\ ^1\mathrm{B}_2$ excited state. The calculated vertical electronic excitation energies and oscillator strengths (f) for the linear and cyclic isomers are listed in Table 5.3.

5.5 Results and discussion

5.5.1 Electronic spectrum and the carrier

Figure 5.2 displays the electronic spectra of AlCCH (m/z = 52) and its isotopomer (m/z = 53) obtained by laser ablation of an Al rod in the presence of 1% C_2H_2 in a He gas mixture. The maxima of the vibronic bands are listed in Table 5.4.

The overall appearance of the origin band, measured at $0.1\,\mathrm{cm}^{-1}$ resolution, shows the general PQR pattern expected for a linear $A\ ^1\Pi \leftarrow X\ ^1\Sigma^+$ transition. *Ab initio* calculations predict that linear-AlCCH with $\mathrm{C}_{\infty\mathrm{v}}$ symmetry is the most stable isomer. The second isomer (cyclic-HAlCC) is a local minimum located $\sim$ 1.71 eV higher in energy. Based on this energy difference it could be expected that linear-AlCCH will be the major contributor to the observed spectrum in a supersonic molecular beam. The TD-DFT calculations predict that the vertical transition energy of the $A\ ^1\Pi \leftarrow X\ ^1\Sigma^+$ system of linear-AlCCH is 3.64 eV (Table 5.3). This is in good agreement with the observed transition energy (3.57 eV) of the origin band. The transition energy for the cyclic isomer is also in the range

	AlCCH ($C_{\infty v}$)		HAlCC (C_{2v})		Experiment
State	T_e/eV	f	T_e/eV	f	T_e/eV
X	0.0 ($^1\Sigma^+$)		0.0 ($^1A_1$)		
1	3.64 ($^1\Pi$)	9.9x10^{-2}	3.83 ($^1B_2$)	1.6x10^{-3}	3.57
2	4.70 ($^1\Sigma^-$)	0	4.04 ($^1B_1$)	1.1x10^{-3}	
3	4.77 ($^1\Delta$)	0	4.58 ($^1A_2$)	0	
4	5.62 ($^1\Sigma^+$)	4.1x10^{-2}	4.81 ($^1A_1$)	7.6x10^{-3}	
5	5.78 ($^1\Sigma^+$)	1.5x10^{-1}	5.57 ($^1A_1$)	3.1x10^{-2}	
6	5.85 ($^1\Pi$)	6.8x10^{-2}	5.84 ($^1B_1$)	3.2x10^{-2}	
7	5.87 ($^1\Sigma^+$)	2.1x10^{-1}	6.01 ($^1B_2$)	5.6x10^{-3}	
8	6.25 ($^1\Sigma^+$)	1.1x10^{-1}	6.17 ($^1A_2$)	0	
9	6.84 ($^1\Pi$)	5.1x10^{-2}	6.22 ($^1B_2$)	5.6x10^{-2}	

Table 5.3: Vertical transition energies and oscillator strenghts (f) for linear and cyclic isomers at the optimized ground state geometries calculated using TD-DFT with aug-cc-pvtz basis sets.

of the experimental spectrum but is likely to have a minor contribution due to its weak oscillator strength (Table 5.3). Other predicted high lying transitions for both the linear and cyclic isomers were beyond the range of the probe laser.

5.5.2 Vibronic bands of AlCCH

The observed spectrum is assigned as the $A\ ^1\Pi \leftarrow X\ ^1\Sigma^+$ electronic transition of linear AlCCH. The vibronic bands reveal a complicated structure (Fig. 5.2). Band 1 is assigned as the origin transition because it is the first strong peak in the low energy region and is not sensitive to the experimental conditions (temperature). The determined T_0 of the origin band is 3.57 eV, which is in good agreement with the calculated value (3.64 eV). Band $2'$, located 516.4 cm^{-1} to the red of the origin is assigned as the 4^0_1 transition, the ν_4'' Al–C stretching motion in the ground state. This value is in accord with the calculated (503 cm^{-1}) and matrix (512.8 cm^{-1}) data.[19] Upon deuteration, the band hardly shifts (516.4 cm^{-1} to 513.6 cm^{-1}), indicating that the vibrational motion involves only the Al and C atoms. Band 2 is located 34.4 cm^{-1} to the blue of the origin. Theoretical calculations predict that the lowest vibrational frequency ν_5'', is about 130 cm^{-1}, which is much larger

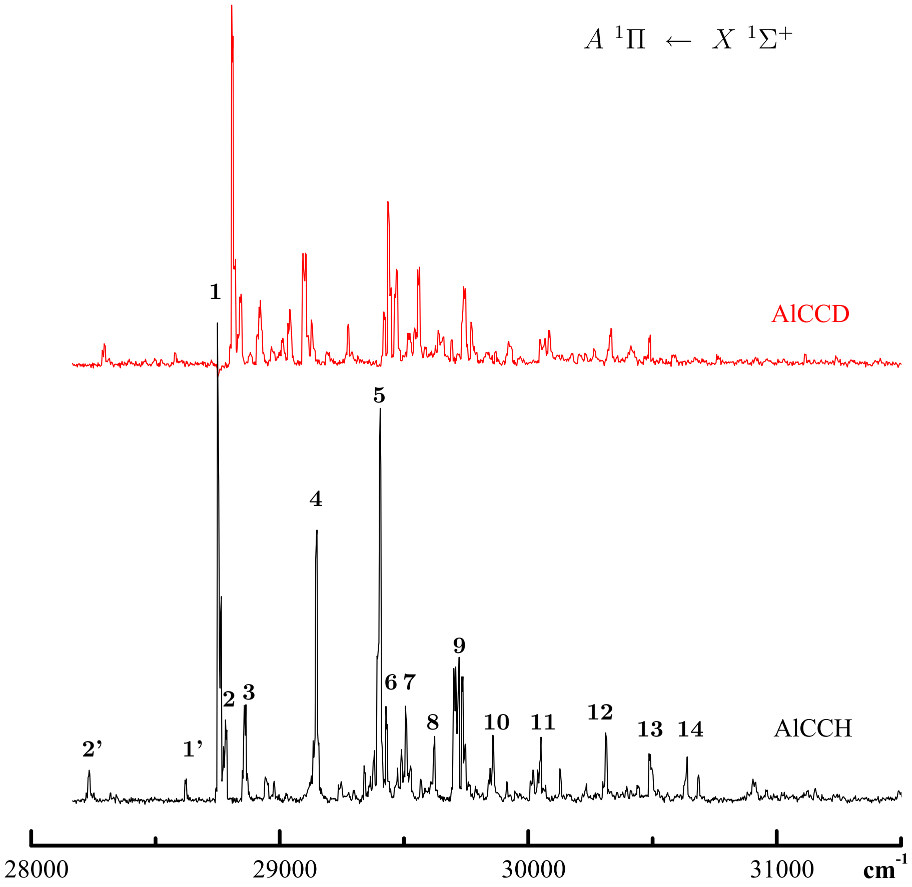

Figure 5.2: Observed $A\ ^1\Pi \leftarrow X\ ^1\Sigma^+$ electronic spectra of AlCCH and AlCCD measured by resonant two-color two-photon ionization technique in a supersonic molecular beam.

than 34.4 cm^{-1}. However, in the degenerate $A\ ^1\Pi$ state, the ν_5' vibrational mode of π-symmetry is subject to a Renner-Teller effect. This causes vibrational levels with $\nu_5' \neq 1$ to split into components. There are two vibrational modes, ν_3' and ν_5' with π-symmetry for linear AlCCH. The observed vibronic pattern indicates that both ν_3' and ν_5' are involved in the Renner-Teller interaction. Bands 2 and 3 can be assigned as the transitions arising from components of ν_5', supported by the small shift upon deuteration. Band 4 shows a large isotopic change and thus is assigned as a component of the CCH bending mode . The calculations give the vibrational frequency of the Al–C stretch mode as 600 cm^{-1} in the $A\ ^1\Pi$ state, leading to the attribution of bands 5 and 11 as the 4_0^1 and 4_0^2 transitions. A clear designation for individual bands is difficult because of the Renner-Teller effect on ν_3' and ν_5' modes. The suggested vibronic assignments are given in Table 5.4.

	$\tilde{\nu}/\mathrm{cm}^{-1}$		$\Delta\tilde{\nu}/\mathrm{cm}^{-1}$		
Label	AlCCH	AlCCD	AlCCH	AlCCD	Assignment
$2'$	28 233.3	28 293.3	-516.4	-513.6	4_1^0 (Al–C stretch)
$1'$	28 624.8	28 577.1	-126.0	-229.7	Hot band
1	28 749.7	28 806.9	0	0	0_0^0 ($A\ ^1\Pi \leftarrow X\ ^1\Sigma^+$)
2	28 784.1	28 843.3	34.4	36.4	ν_5' (AlCC bend)
3	28 864.3	28 921.9	114.5	115	ν_5' (AlCC bend)
4	29 149.6	29 103.7	399.9	296.9	ν_3' (CCH bend)
5	29 404.2	29 435.4	654.5	628.5	4_0^1 (Al–C stretch)
6	29 427.0	29 468.1	677.3	661.2	(AlCC bend)
7	29 505.7	29 563.3	756.0	756.5	(AlCC bend)
8	29 623.8	29 635.9	874.0	829.1	(AlCC bend)
9	29 721.5	29 740.1	971.8	933.2	(AlCC bend)
10	29 857.3	29 921.7	1107.6	1114.8	(AlCC bend)
11	30 051.2	30 081.0	1301.5	1274.1	4_0^2 (Al–C stretch)
12	30 310.8	30 332.9	1561.1	1526.0	
13	30 485.5	30 491.1	1735.8	1684.2	
14	30 640.0		1890.0		

Table 5.4: Vibronic bands in the $A\ ^1\Pi \leftarrow X\ ^1\Sigma^+$ system of AlCCH and AlCCD.

5.5.2.1 Renner-Teller effect

The Renner-Teller effect, the coupling between vibrational and electronic angular momenta, has been extensively studied in the spectra of triatomic molecules, particularly those with $^2\Pi$ electronic states. This coupling would give rise to anomalies in the vibrational bands of the electronic spectra. In linear tetra-atomic molecules, the Renner-Teller effect was less studied due to the complexity arising from the simultaneous angular momentum coupling in two degenerate bending modes.

The AlCCH vibronic spectrum exhibits a complex structure and a preliminary analysis has been attempted taking into consideration the Renner-Teller effect. Clouthier *et al.*[27,28] investigated the effective vibronic Hamiltonian for a linear tetra-atomic molecule in a Π state. The Renner-Teller model includes various vibronic coupling, spin-orbit, Fermi resonance, and anharmonicity terms. The effective vibronic Hamiltonian has been written for AlCCH molecule. The terms in tetra-atomic Hamiltonian are then:[27]

$$H = H_0 + H_{anh} + H_{ev}, \tag{5.1}$$

where,

$$H_0(\Delta\nu_3 = 0; \Delta\nu_5 = 0) = \omega_3(v_3 + 1) + \omega_5(v_5 + 1), \tag{5.2}$$

and the Renner-Teller coupling terms (ϵ_i) with i=3 or i=5:

$$H_{\epsilon_i}(\Delta\Lambda = 2; \Delta v_i = 2, \Delta l_i = -2) = \frac{1}{4}\epsilon_i\omega_i\sqrt{(v_i - l_i + 2)(v_i - l_i + 4)}, \tag{5.3}$$

$$H_{\epsilon_i}(\Delta\Lambda = 2; \Delta v_i = -2, \Delta l_i = -2) = \frac{1}{4}\epsilon_i\omega_i\sqrt{(v_i + l_i)(v_i + l_i - 2)}, \tag{5.4}$$

$$H_{\epsilon_i}(\Delta\Lambda = 2; \Delta v_i = 0, \Delta l_i = -2) = \frac{1}{2}\epsilon_i\omega_i\sqrt{(v_i + l_i)(v_i - l_i + 2)}, \tag{5.5}$$

The basis functions are:

$$|\Lambda\rangle|\Sigma\rangle|v_s\rangle\prod_{i=1}^{N}|v_i, l_i\rangle, \tag{5.6}$$

where $|\Sigma\rangle$ are the spin functions with quantum numbers Σ=$\pm1/2$ and the $|v_s\rangle$ are one-dimensional harmonic-oscillator functions with quantum numbers v_s=0,1,2,...

Using the equations mentioned above the matrix elements have been identified for v_i=0,1 and 2 generating a 22×22 matrix. The cross-coupling, the anharmonicity and Fermi-resonances terms have not been included in the matrix. The Renner-Teller parameters for AlCCH molecules have been estimated based on the values obtained for a similar molecule (CaCCH), ϵ_3=0.003 and ϵ_5=0.035, respectively.[29,30] The harmonic frequencies ω_3=733 cm^{-1} and ω_5=132 cm^{-1} used as starting point in the model were the calculated values for the electronic ground state of AlCCH. The obtained term values don't match the pattern of the experimental vibronic spectrum and new parameters have been considered as shown in Table 5.5.

	Renner-Teller parameters		
ϵ_3	0.009	0.04	0.04
3^1_0 (σ^-, δ, σ^+)/cm^{-1}	396.4/400/403.6	384/400/416	384/400/416
3^2_0 (π^-, ϕ, π^+)/cm^{-1}	794.9/800/805.09	777.3/800/822.7	777.3/800/822.7
ϵ_5	0.035	0.035	0.4
5^1_0 (σ^-, δ, σ^+)/cm^{-1}	110.49/114.5/118.51	110.49/114.5/118.51	68.7/114.5/160.3
5^2_0 (π^-, ϕ, π^+)/cm^{-1}	223.35/229/234.68	223.35/229.0/234.68	167.02/230.0/295.67

Table 5.5: Renner-Teller parameters used in the model. The harmonic frequencies used are: ω_3=400 cm^{-1} and ω_5=114.5 cm^{-1}.

The harmonic frequencies used in the model are the experimental values obtained assuming that the band located at 114.5 cm^{-1} is the σ^+ component in the $\nu_5^{'}$, v$^{'}$=1 and the 399.9 cm^{-1} band as the σ^+ component in the $\nu_3^{'}$, v$^{'}$=1 as seen in Fig. 5.3. The estimated term values indicate a separation of ∼4 cm^{-1} between the σ^-, δ and σ^+ components of the 5^1_0 mode. The same frequency differences was observed for the 3^1_0 components. For the 5^2_0 and 3^2_0 the frequency difference increases to ∼6 cm^{-1}. Considering that the resolution of the Ekspla laser used in obtaining the vibronic spectrum is ∼5 cm^{-1} the individual vibronic bands can not be separated. Increasing the Renner-Teller parameter the separation of different Renner-Teller components increases to ∼6 cm^{-1} for ϵ_3=0.04 and to ∼46 cm^{-1} for ϵ_5=0.4. In the latter case individual vibronic bands can be separated.

Based on the symmetry selection rules, the allowed transitions from the $X^1\Sigma^+$ ground electronic state of AlCCH to different vibronic levels in the $A\ ^1\Pi$ excited state are visualized in the Fig. 5.4. For the $\nu_3^{'}$ mode (ϵ_3=0.04 case), v$^{'}$=1 only one transition is allowed, namely from the v$^{''}$=0 level in the ground state to the σ^+

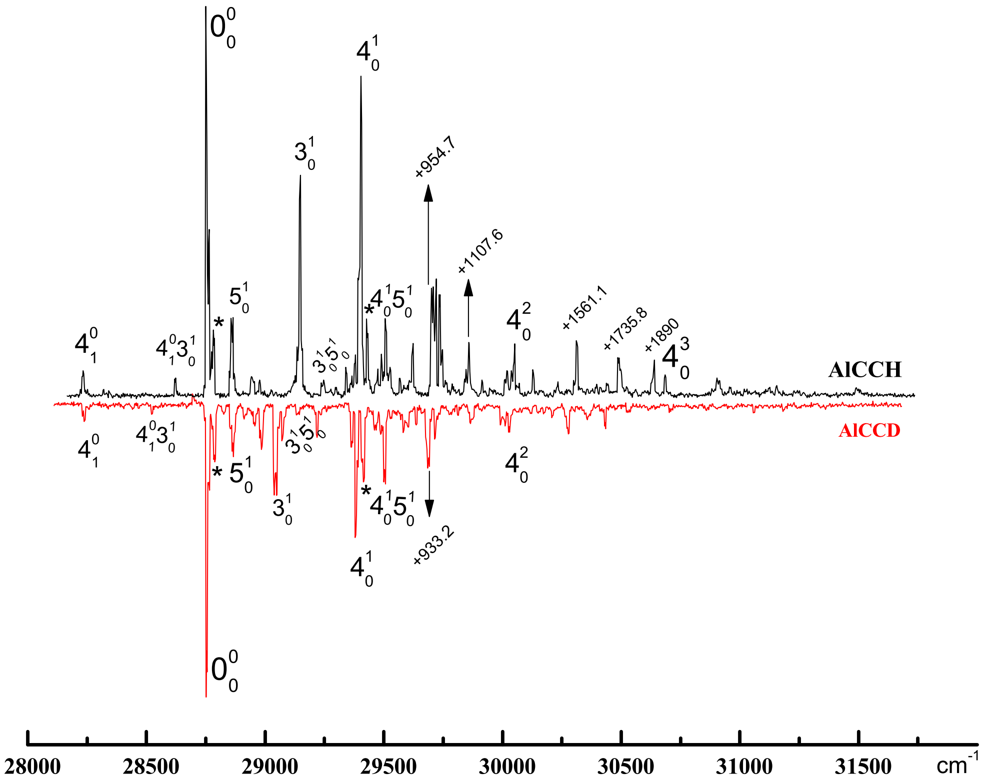

Figure 5.3: Observed $A\ {}^1\Pi \leftarrow X\ {}^1\Sigma^+$ electronic spectra of AlCCH and AlCCD measured by resonant two-color two-photon ionization technique in a supersonic molecular beam and the new Renner-Teller assignment.

component in the excited state. Other allowed transitions to the $v'=1$ level (σ^+ and δ) are from the $v''=1$ in the ground state and would show up in the spectrum as hot bands located ~329.4 cm^{-1}. In the experimental spectrum no band is observed around this value. For $v'=2$, the allowed transition is from the $v''=0$ level in the ground state to the π^+ component in the excited state. More allowed transitions to this vibronic level are the ones originating from the $v''=1$ and 2 levels in the ground state. These bands would be located at ~89.6 cm^{-1} to the blue and ~643.4 cm^{-1} to the red of the origin, respectively. In the experimental spectrum none of the bands mentioned above are present. The 3_0^2 overtone would be located at ~805.9 cm^{-1} based on the Renner-Teller model. Taking into account that no anharmonicity terms were included in the model, the band might be located at a

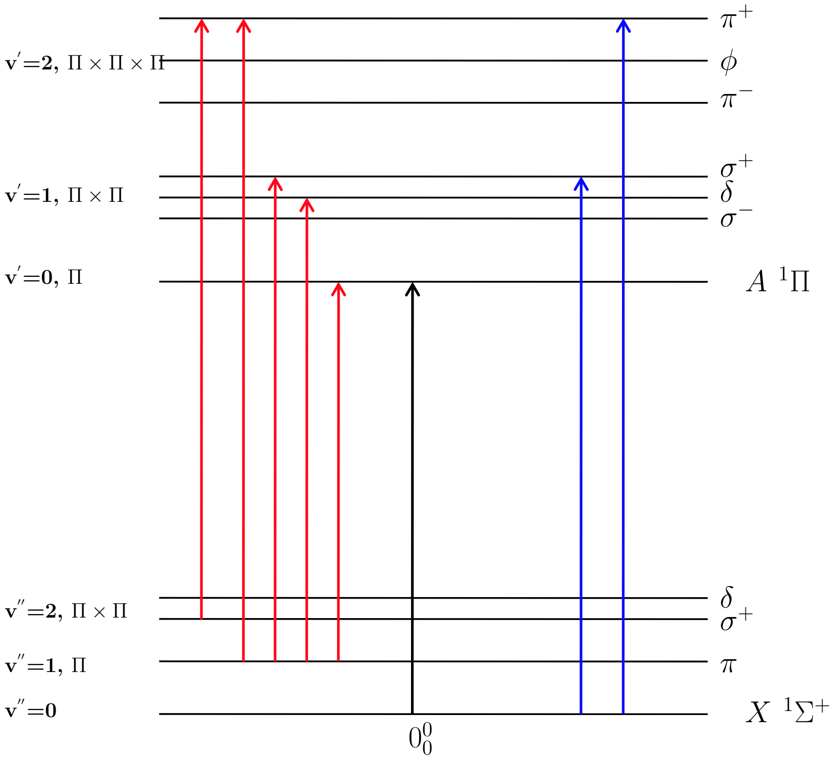

Figure 5.4: Qualitative scheme of the allowed electronic transitions in the $A\,^1\Pi \leftarrow X\,^1\Sigma^+$ electronic spectra of AlCCH. The transitions generated from the level v=0 in the ground state are displayed in blue and the hot bands in red.

shorter frequency. In either of the cases, the presence of the 3_0^2 overtone can not be identified in the experimental spectrum.

The same treatment has been applied to identify the vibronic bands due to the excitation of the ν_5' mode. The allowed transitions would be the same as for the ν_3'. The allowed excitations from the v″=1 to the v′=1 level (σ^+ and δ) would be located at ∼13.7 cm^{-1} and 17.5 cm^{-1} to the red of the origin band. The transition to the π^+ vibronic level would be present to the blue of the origin band at ∼102.7 cm^{-1}. None of these bands are present in the experimental spectrum.

New assigned bands in the vibronic spectrum are the $4_1^0 3_0^1$ located at -126.0 cm^{-1} from the origin, previously assigned as a hot band. Based on the evident isotopic shift upon deuteration the assignment of this band is unambiguous. The band located at 399.9 cm^{-1} to the blue of the origin is now assigned as 3_0^1 transition based again on the isotopic shift upon deuteration. It is to be noted that the excited state frequency obtained in this case from the experimental spectrum is much lower than the calculated value for ν_3 for the ground state (733 cm^{-1}). The 114.5 cm^{-1} band (labeled with 3 in the Fig. 5.2) is now assigned as one excitation of the ν_5 mode, corresponding to the AlCC bending motion. A new band, of weak intensity, located at ~493.8 cm^{-1} is now tentatively assigned as the combination band of the bending modes ($3^1_0 5^1_0$). This band also shifts upon deuteration. The band centered at ~756 cm^{-1} to the blue of the origin band (labeled with 7 in the Fig. 5.2) exhibits no shift upon deuteration and is assigned as another combination band between the AlC stretching mode and the AlCC bending vibration.

Thus far, the unassigned bands in the experimental spectrum could not be accounted for by other allowed transitions. This may be due to the fact that the Renner-Teller model used does not take into account the cross coupling terms between the two bending modes (ϵ_{35}), the anharmonicity terms or transitions to the higher vibronic levels. The model should be improved by adding the above mentioned terms and transitions up to v=4 should be considered. This would increase the matrix size and a routine fitting programm would be required to perform the fitting procedure.

5.5.2.2 Vibrational cooling

An estimate of the cooling efficiency in the molecular beam can be determined from the resolved electronic spectra of the neutral molecules. This spectroscopic approach represents an easy method to evaluate the vibrational temperature. By identifying, on either side of the band origin, a $1 \leftarrow 0$ vibronic transition and the corresponding hot band ($0 \leftarrow 1$), the vibrational temperature can be inferred from the comparison of their relative intensities (assuming a molecular beam at thermal equilibrium described by a Maxwell-Boltzmann distribution). If the Franck-Condon factors for both transitions are similar, their measured intensities should be simply proportional to the populations of the initial states. Hence, the temperature T is obtained from the intensities $I_{1 \leftarrow 0}$ and $I_{0 \leftarrow 1}$ as follows:

$$\frac{I_{1\leftarrow 0}}{I_{0\leftarrow 1}} = e^{\frac{\Delta E}{k_B \cdot T}} \Longrightarrow T = \frac{\Delta E}{k_B \ln\left(\frac{I_{1\leftarrow 0}}{I_{0\leftarrow 1}}\right)} \tag{5.7}$$

ΔE is the energy difference between the initial states, i.e., the difference between the band origin and the hot band. The states taken into consideration for evaluating the vibrational temperature for AlCCH are the bands labeled with $2'$ and 5 in the Figure 5.2, corresponding to 4^0_1 and 4^1_0 transitions. The estimated vibrational temperature is about 750 K.

Using this estimate the intensity of other hot bands corresponding to the bending modes in the ground state can be calculated. The ΔE values are the *ab initio* calculated harmonic vibrational frequencies, 733 cm^{-1} for ν_3'' and 132 cm^{-1} for ν_5'', respectively. The intensity of the ν_3'' band, not observed in the vibronic spectrum, is about half of the 4^0_1 (labeled as $2'$ in Figure 5.2) and that of the ν_5'' band approximately the same intensity as 4^0_1. These estimates should not be taken as accurate due to the fact that the vibrational temperature assumed to be 750 K, has been calculated from the Al–C stretching mode. The vibrational cooling is different for different degrees of freedom. In a supersonic beam the two-body collisions with the carrier gas induce the cooling of the translational and rotational degrees of freedom to reasonable low temperatures. As vibrations cool through rotation and translation the bending modes cool more efficiently than the stretching modes where due to the linear geometry of the molecule the rotational levels are further apart. When the molecule is bent, the rotational K - structure would allow a better cooling.

5.5.3 Rotational structure

The origin band of the $A\ ^1\Pi \leftarrow X\ ^1\Sigma^+$ transition that was rotationally resolved with a modest resolution of 0.1 cm^{-1}, along with the simulation of the spectrum based on the least squares fit of the lines are shown in Figure 5.5. To obtain a fit, the Σ^+ and Π symmetries in the X and A states as predicted by *ab initio* calculations for the linear isomer were used.

The calculated ground state rotational constant (Table 5.2) was used as a reasonable starting point in the simulation. The P-branch band-head shows that the

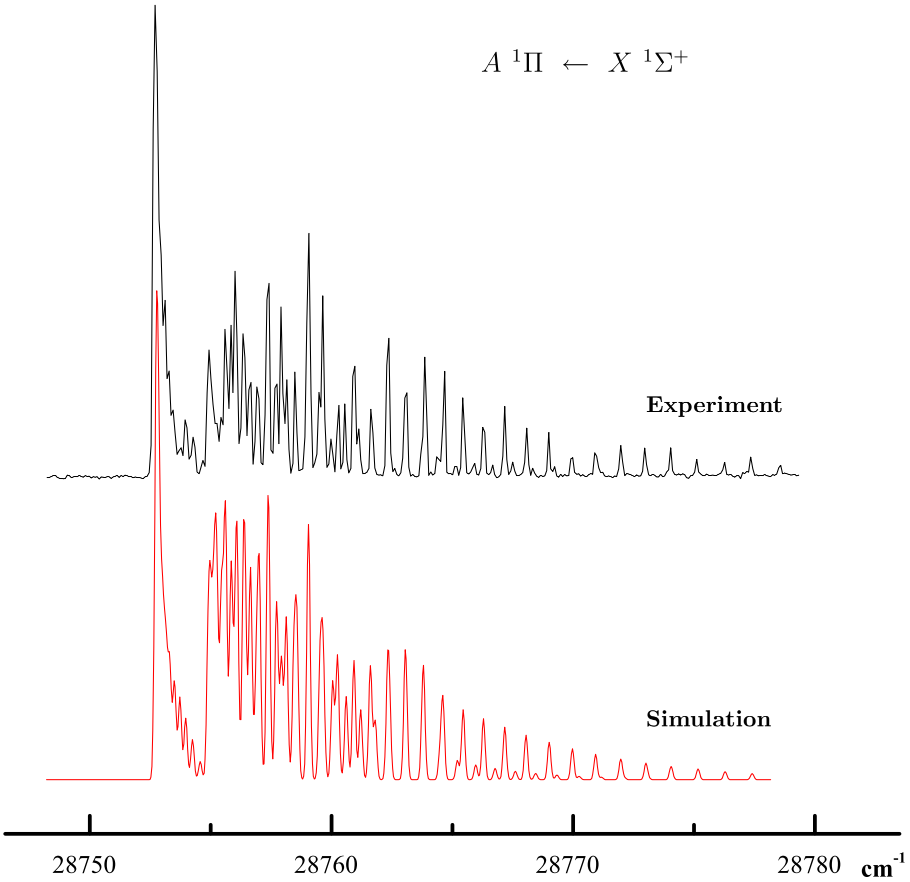

Figure 5.5: The origin band in the $A\ ^1\Pi \leftarrow X\ ^1\Sigma^+$ electronic transition for the AlCCH. The rotational temperature employed in the simulation is 45 K.

rotational constant in the excited state is larger. The simulation[31] was performed by systematically adjusting the rotational constant in the $A\ ^1\Pi$ state, while varying the spectroscopic line-width from 0.1 cm^{-1} to 0.2 cm^{-1} and rotational temperatures from 25 to 50 K. Good agreement between the experiment and simulation was achieved using 0.16 cm^{-1} and 45 K. A higher resolution simulations are presented in **Appendix 1**. Variations in line intensities between the experimental and simulated spectra are mainly due to the ablation source instability.

Rotational line assignments were made by comparing the observed spectral lines with the calculated ones. The linear least square fit was performed using forty rotational lines and floating the rotational constants for ground and excited state.

The derived spectroscopic constants are given in Table 5.6. Higher order terms, such as centrifugal distortion or lambda-doubling parameter, q, were not included in the model as the spectral resolution used was inadequate.

Parameter	$X\ ^1\Sigma^+$	$A\ ^1\Pi$
T_0/cm^{-1}	0	28 755.0455(50)^a
B_0/cm^{-1}	0.16487(14)^a	0.17845(13)^a
$r_{\mathrm{Al-C}}/\mathrm{Å}$	1.96830	1.85235

Table 5.6: Molecular parameters determined from the least square fit of the spectrum for AlCCH. ^{a}Values in parentheses denote one standard deviation and apply to the last digits of the constants.

Table 5.7 lists the frequencies recorded for 20 separate rotational transitions of linear AlCCH. The lines are assigned as part of the R-branch. The analysis indicates that while this branch partially overlaps with Q- and P- ones, the assignment of the R-lines was possible because their intensity is higher. Individual overlapping lines from the Q-branch can not be easily distinguished due to high density of spectral lines. The shape of the P branch is of a band head, thus making individual line assignment difficult. The T_0 line calculated from the simulations is at 28755.04 cm^{-1}.

The derived rotational constant analysis shows that the Al–C bond-length decreases significantly in the $A\ ^1\Pi$ electronic excited state (Table 5.6). This indicates that Al–C is more bonding in the excited than in the ground state. The potential energy curves along the Al–C bond stretching coordinate for the ground and the excited states have been calculated for a better understanding of the bonding changes (Fig. 5.6). These give an Al–C bond-length as 1.977 Å in the $X\ ^1\Sigma^+$ and 1.775 Å in the $A\ ^1\Pi$ state, a $\sim$ 10% decrease. The constants inferred from the rotational analysis yield a decrease of $\sim$ 6%. The calculations indicate that the highest occupied molecular orbital (HOMO), 9σ, is 78% dominated by the 3s orbital of Al atom, antibonding in nature, whilst the lowest unoccupied molecular orbital (LUMO), 5π, is largely (92%) the $3p_x3p_y$ atomic orbital of Al with bonding character. The transition of the electron from the HOMO to LUMO leads to a decrease in the Al–C bond-length. This effect has also been observed in the

$J' \rightarrow J''$	$\nu_{\mathrm{obs}}/\mathrm{cm}^{-1}$	$\nu_{\mathrm{obs}} - \nu_{\mathrm{calc}}/\mathrm{cm}^{-1}$
12 → 11	28 760.9509	0.0155
13 → 12	28 761.6339	0.0153
14 → 13	28 762.3640	0.0349
15 → 14	28 763.0964	0.0296
16 → 15	28 763.8568	0.0250
17 → 16	28 764.6909	0.0669
18 → 17	28 765.4266	-0.0168
19 → 18	28 766.2723	-0.0178
20 → 19	28 767.1661	0.0021
21 → 20	28 768.0839	0.0187
22 → 21	28 768.9984	0.0048
23 → 22	28 769.9609	0.0177
24 → 23	28 770.8994	-0.0327
25 → 24	28 771.9548	0.0126
26 → 25	28 772.9620	-0.0176
27 → 26	28 774.0380	-0.0062
28 → 27	28 775.1175	-0.0188
29 → 28	28 776.2622	-0.0071
30 → 29	28 777.3382	-0.0632
31 → 30	28 778.5758	0.0008

Table 5.7: Observed rotational frequencies in the R-branch of the 0^0_0 band in the $A\ ^1\Pi \leftarrow X\ ^1\Sigma^+$ electronic transition of linear AlCCH.

isoelectronic molecule AlCN[32] as well as in other metal mono-acetylides, such as MgCCH,[20] CaCCH[21] and SrCCH.[22]

5.6 Conclusions

An electronic spectrum of linear AlCCH has been obtained using a resonant two-color two-photon ionization technique. The complicated vibronic structure in the $A\ ^1\Pi \leftarrow X\ ^1\Sigma^+$ band system is due to a Renner-Teller effect involving the two

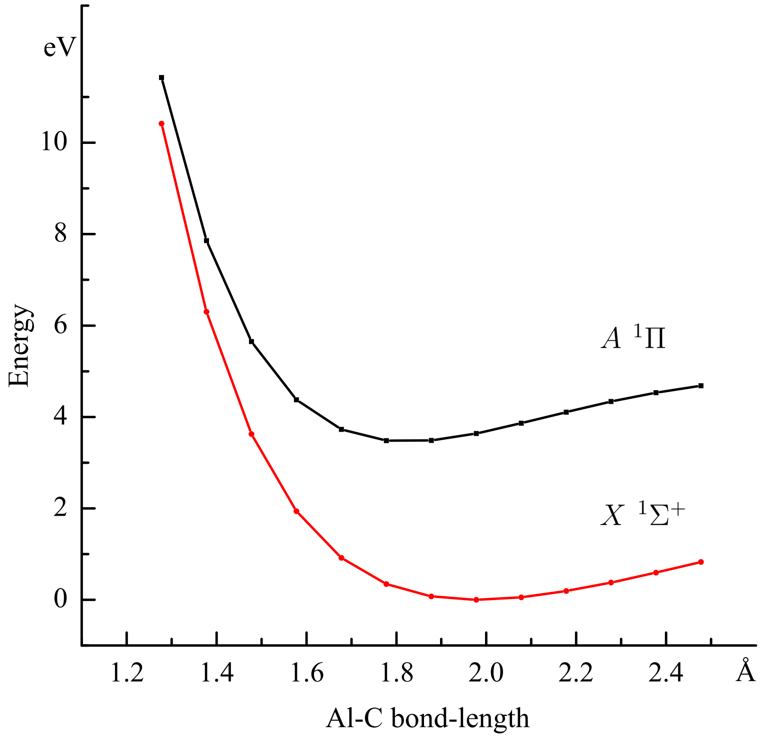

Figure 5.6: Calculated potential energy curves along Al–C bond stretching coordinate using DFT method with aug–cc-pvtz basis sets.

vibrational modes, $\nu_3^{'}$ and $\nu_5^{'}$. An analysis yields $\nu_4^{''} = 516.4\,\mathrm{cm}^{-1}$ for the stretching mode in the ground state and $\nu_4^{'} = 654.5\,\mathrm{cm}^{-1}$ in the $A\ ^1\Pi$ state.

The rotational structure apparent for the origin band shows that AlCCH is linear both in its ground $X\ ^1\Sigma^+$ and first excited $A\ ^1\Pi$ electronic state, the latter being characterized by a decrease in the Al–C bond-length, a behavior similar to other metal mono-acetylides.

Regarding the astrophysical interest it is difficult to compare the observed AlCCH electronic transitions with the diffuse interstellar bands data because there are few discrete absorptions below $\sim$ 400 nm.[33] However, AlCCH is likely to be present in carbon-rich stars where the isoelectronic molecule AlNC as well as other aluminum-bearing compounds have been detected, in particular in IRC +10216 and CRL 2688.[5,6] Although AlCCH is closed-shell, it probably lacks the stability of more robust species such as AlF and AlCl detected in the dense inner envelope of these stars. Thus one would expect to find aluminum acetylide toward the outer-shell. The rotational constants deduced here also may provide the basis for the search of the millimeter-wave spectrum of AlCCH in the laboratory.

Bibliography

[1] J. L. Highberger, K. J. Thomson, P. A. Young, D. Arnett, and L. M. Ziurys, Astrophys. J. **593**, 393 (2003).

[2] K. Kawaguchi, E. Kagi, T. Hirano, S. Takano, and S. Saito, Astrophys. J. **406**, L39 (1993).

[3] L. M. Ziurys, A. J. Apponi, M. Guélin, and J. Cernicharo, Astrophys. J. **445**, L47 (1995).

[4] B. E. Turner, T. C. Steimle, and L. Meerts, Astrophys. J. **426**, L97 (1994).

[5] L. M. Ziurys et al., Astrophys. J. **564**, L45 (2002).

[6] J. Cernicharo and M. Guélin, Astron. Astrophys. **183**, L10 (1987).

[7] L. M. Ziurys, A. J. Apponi, and T. G. Phillips, Astrophys. J. **433**, 729 (1994).

[8] A. Janczyk and L. M. Ziurys, Astrophys. J. **639**, L107 (2006).

[9] S. T. Ridgway, D. F. Carbon, and D. N. B. Hall, Astrophys. J. **225**, 138 (1978).

[10] S. T. Ridgway, D. N. B. Hall, S. G. Kleinmann, D. A. Weinberger, and R. S. Wojslaw, Nature **264**, 345 (1976).

[11] I. Cherchneff and A. E. Glassgold, Astrophys. J. **419**, L41 (1993).

[12] L. Manceron and L. Andrews, J. Am. Chem. Soc. **107**, 563 (1985).

[13] J. H. B. Chenier, J. A. Howard, B. Mile, and R. Sutcliffe, J. Am. Chem. Soc. **105**, 788 (1983).

[14] P. H. Kasai, J. Am. Chem. Soc. **105**, 6704 (1983).

[15] E. S. Kline, Z. H. Kafafi, R. H. Hauge, and J. L. Margrave, J. Am. Chem. Soc. **107**, 7559 (1985).

[16] J. R. Flores and A. Largo, J. Phys. Chem. **96**, 3015 (1992).

[17] Y. M. Xie, B. F. Yates, and H. F. Schaefer, J. Am. Chem. Soc. **112**, 517 (1990).

[18] J. S. Tse, J. Am. Chem. Soc. **112**, 5060 (1990).

[19] G. V. Chertihin, L. Andrews, and P. R. Taylor, J. Am. Chem. Soc. **116**, 3513 (1994).

[20] D. W. Tokaryk, A. G. Adam, and W. S. Hopkins, J. Mol. Spectrosc. **230**, 54 (2005).

[21] M. G. Li and J. A. Coxon, J. Mol. Spectrosc. **176**, 206 (1996).

[22] M. J. Dick, P. M. Sheridan, J. G. Wang, and P. F. Bernath, J. Mol. Spectrosc. **233**, 197 (2005).

[23] H. Ding et al., J. Chem. Phys. **119**, 814 (2003).

[24] W. C. Wiley and I. H. McLaren, Rev. Sci. Instrum. **26**, 1150 (1955).

[25] M. J. Frisch et al., Gaussian98, Revision A.7, Gaussian Inc., Pittsburgh PA, 1998.

[26] R. E. Stratmann, G. E. Scuseria, and M. J. Frisch, J. Chem. Phys. **109**, 8218 (1998).

[27] S. G. He and D. J. Clouthier, J. Chem. Phys. **123**, 014316 (2005).

[28] S. G. He and D. J. Clouthier, J. Chem. Phys. **123**, 014317 (2005).

[29] M. Li and J. A. Coxon, J. Mol. Spec. **180**, 287 (1996).

[30] M. Li and J. A. Coxon, J. Mol. Spec. **196**, 14 (1999).

[31] C. W. Western, PGOPHER a program for simulating rotational structure, http://pgopher.chm.bris.ac.uk.

[32] I. Gerasimov, X. Yang, and P. J. Dagdigian, J. Chem. Phys. **110**, 220 (1999).

[33] P. Jenniskens and F. X. Desert, Astron. Astrophys. Suppl. Ser. **106**, 39 (1994).

6 Electronic spectra of $MgC_{2n}H$ (n=1-3) chains in the gas phase

6.1 Abstract

Electronic transitions of $MgC_{2n}H$ (n=1-3) have been observed in the gas phase in the visible region. A mass-selective resonant two-color two-photon ionization technique coupled to a laser ablation source was used. *Ab initio* calculations on the geometries, energies and vertical electronic excitations have been carried out using the hybrid density functional theory and coupled cluster approach. The spectra are assigned as the $A\ ^2\Pi \leftarrow X\ ^2\Sigma^+$ electronic transition of linear chains. The origin bands are located at 4383, 4453 and 4525 Å for MgC_2H, MgC_4H and MgC_6H, respectively, and provide a means of detecting such species in astronomical environments.

6.2 Introduction

Despite the success of ion-molecule chemistry for carbon and other non-refractory elements, there remain unanswered questions concerning the molecular carriers of the cosmically abundant metallic elements, such as magnesium, iron, and sodium.[1] These elements are heavily depleted in molecular clouds and a few percent may remain in the gas phase as atoms or incorporated in molecules.[2] One believes, in general, that most of these elements are condensed out onto the surfaces of dust grains. The identification of the molecular carriers containing such metals in the interstellar medium would have implications for gas-phase and grain chemistry, ionization balance in dust particles, recycling by shock waves, and constraining models of nucleosynthesis.[3]

Carbon chains are abundant molecules and play an important role in the ISM chemistry.[4–6] For example, small carbon chains C_2, C_3, C_5 were detected in the interstellar medium (ISM)[7,8] and larger ones were proposed to be of relevance as carriers of the diffuse interstellar bands (DIBs).[9] Monohydrocarbon chains C_nH (n=2-8) have been measured in the circumstellar envelope of the carbon rich star IRC +10216 and in dark molecular clouds TMC-1.[10–12] The small even polyynes $HC_{2n}H$, (n=2-3) chains have been observed in the proto-planetary nebulae of CRL 618 and CRL 2688[13,14] and in the atmosphere of planets.[15] Because the isoelectronic cyanopolyynes $HC_{2n+1}N$ (n=1-5) were detected in the ISM,[16–18] the larger ones $HC_{2n}H$ chains are believed to exist there. One thus wonders if metal-containing carbon chains are also present. Unfortunately the knowledge about the gas-phase abundances and forms of refractory-metal containing species in the ISM is limited.[19] Spectroscopy and structure of such species are relevant.

Magnesium is one of the most abundant refractory-metal elements in the Universe. Molecules MgNC and MgCN have been discovered toward circumstellar envelopes of IRC +10216 and CRL 2688.[3,20–22] Both molecules are present in the outer shell of IRC +10216, where temperatures (T∼10-50 K) and densities (n∼ 10^5 cm^{-3}) are comparable to those in molecular clouds. In the inner circumstellar shell (T≥1000 K, n∼ 10^10 cm^{-3}) the more stable metal halide species NaCl, AlCl, KCl, and AlF are abundant.[23,24] The formation of metal halide species in the inner envelope of IRC +10216 has been explained by equilibrium chemistry.[25,26] The synthesis of MgNC and MgCN radicals, however, is more difficult to account for by equilibrium chemistry. Several possible routes have been proposed such as the radiative association of Mg^+ +HCN (or HNC), followed by dissociative electron recombination,[1,21] the reaction of Mg^+ +CN, and desorption from grain surface.[27] However, experimental data for these processes are scarce. As part of the understanding of chemistry, the study of other Mg-bearing species has been carried out. For example, MgC_2H, a radical isoelectronic with MgCN, has been investigated in the laboratory by millimeter wave spectroscopy.[1]

Electronic spectra of several alkaline-earth monoacetylides MC_2H (M=Mg,Ca, Sr) have been investigated experimentally[28–32] and theoretically.[33,34] These indicate that the alkaline-earth monoacetylides have a linear geometry and $X\ ^2\Sigma^+$ ground state symmetry. Considering that magnesium and the polyyne chains $HC_{2n}H$ are both abundant in the ISM, it is expected that $MgC_{2n}H$ chains may be identified. The abundance and distribution of such $MgC_{2n}H$ species, as function of molecular size, in the ISM could provide an important clue for the chemistry of magnesium containing species. Thus laboratory-based spectroscopic studies are vital.

In this paper the gas-phase electronic spectra of MgC_4H and MgC_6H have been observed for the first time. The experimental technique used a two-color laser spectroscopy with mass-analysis and a laser ablation source. *Ab initio* calculations on the ground and electronic excited states have been carried out. The electronic structures and bonding nature of these magnesium containing carbon chains are discussed in view of the spectral analysis.

6.3 Experimental

The experimental set-up consists of a molecular beam combined with a linear time-of-flight (TOF) mass spectrometer[35]). The laser ablation of a magnesium rod in a pulsed gas mixture of 1% CH_4 (or HC_2H) in He was used to produce MgC_4H and MgC_6H. The 532 nm output of a Nd:YAG laser (30 mJ/pulse, 5 ns width) was focused on a rotated and translated magnesium rod. The vaporization took place within a pulse of the carrier gas with a backing pressure of ~ 5 bar. The hot plasma flew through a 15 mm long and 3 mm in diameter channel followed by expansion into a vacuum chamber. The resulting supersonic jet was passed through a skimmer. Ions were removed from the beam by a perpendicular electrical field before entering the extraction zone of the TOF. The neutral molecules were then ionized by lasers and the ions were extracted by a pulsed electrical field. The signal from the multichannel plate ion-detector was fed into a fast oscilloscope followed by data acquisition.

Resonant two-color two-photon ionization (R2C2PI) spectra of MgC_2H, MgC_4H and MgC_6H have been measured over the 360-640 nm range. Excitation photons were provided from an OPO system ($\sim 5\,\mathrm{cm}^{-1}$ bandwidth) or a dye laser ($\sim 0.15\,\mathrm{cm}^{-1}$) pumped by a XeCl excimer laser. The power of the OPO was typically 15 in the visible and 5 mJ/pulse in the UV region. The wavelength calibration was carried out by a wavemeter. An ArF-excimer laser at 193 nm delivered the photons for the ionization.

6.4 Theoretical calculations

6.4.1 Ground states

Ab initio studies for MgC_2H at the RCCSD(T) and MRCI+Q levels of theories have been reported.[34] The results indicated that the single reference RCCSD(T) method yields good results compared with the experimental observations. In this study the hybrid density functional theory DFT-B3LYP[36] and the restricted coupled cluster RCCSDT approach[37] were used for the ground state electronic structures of $MgC_{2n}H$ chains with n=1-8. Dunning's correlation-consistent basis set of aug-cc-pVTZ[38] was taken for full geometry optimization and calculations of vibrational frequencies. The resulting Mg-C bond lengths, the harmonic frequencies of the Mg-C stretching mode, rotational constants B_e and dipole moments D for MgC_2H to MgC_6H are given in Table 6.1.

Species	State	Method	$D(Debye)$	$\nu_{Mg-C}(cm^{-1})$	r_{Mg-C}(Å)	B(GHz)
MgC_2H	$X\ ^2\Sigma^+$	B3LYP	1.735	488	2.048388	4.937922
		RCCSD(T)			2.055774	4.846166
		^{a}MRCI+Q		495	2.0516	4.8890
		Experiment		496^b		5.009256^c
MgC_4H	$X\ ^2\Sigma^+$	B3LYP	2.307	398	2.052273	1.382526
		RCCSD(T)			2.0610296	1.351426
MgC_6H	$X\ ^2\Sigma^+$	B3LYP	2.757	353	2.055892	0.581761
		RCCSD(T)			2.065313	0.576899

Table 6.1: Calculated dipole moments D, Mg-C stretching frequencies, bond lengths and rotational constants B in the ground state for $MgC_{2n}H$ (n=1-3) at the B3LYP and RCCSD(T) levels of theory with aug-cc-pVTZ basis sets; ^{a} from Ref.;[34] ^{b} from Ref.;[31] ^{c} from Ref.[1]

The trends of these values are shown as a function of the chain size $MgC_{2n}H$ (n=1-8) (Figure 6.1). Both the lowest bending frequency (curve **1**) and Mg-C stretching frequency (curve **2**) decrease with n, as has been observed for other carbon chain systems. The Mg-C bond length (curve **3**) increases from 2.048 to 2.063 Åon passing from MgC_2H to $MgC_{16}H$. The calculations also indicate a C-C alternation with short (~ 1.23 Å) and long (~ 1.34 Å) bonds.

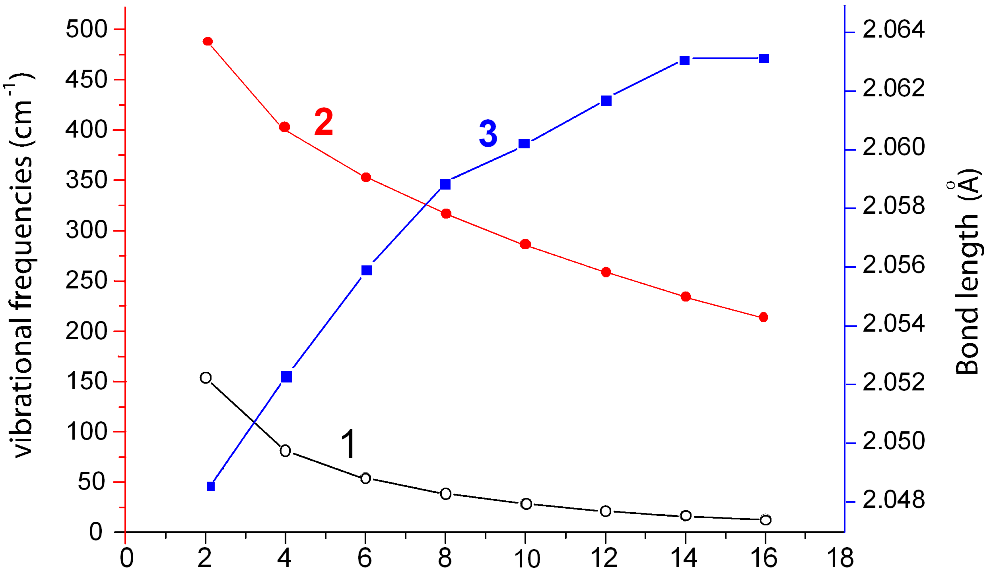

Figure 6.1: Calculated lowest bending vibrational frequencies (**1**), Mg–C stretching frequency (**2**) and Mg–C bond-lengths (**3**) in the ground state for $MgC_{2n}H$ (n=1-8) as a function of the number of carbon atoms, using TD-DFT theory with cc-pVTZ basis sets.

6.4.2 Excited states

Theoretical investigation of the first excited electronic state of MgC_2H has been reported.[34] The calculated T_e of the $A\ ^2\Pi$ state is 2.81 eV and 2.88 eV at the RCCSD(T) and MRCI levels. The observed transition energy of MgC_2H is around 2.83 eV. This indicates that single reference theoretical methods such as RCCSD(T) are reasonable in predictions. Thus the RCCSD(T) approach was used for MgC_2H to MgC_6H and the time-dependence B3LYP theory (TD-DFT)[39] for all $MgC_{2n}H$ (n=1-8) molecules with Dunning's correlation-consistent basis sets of cc-pVTZ. The $X\ ^2\Sigma^+$ ground state of linear $MgC_{2n}H$ is dominated by the $...4(n+1)\sigma^2(n+1)\pi^4(4n+5)\sigma^1$ electronic configuration, n=1,2,3...8.

Electron promotion from the semi-occupied molecular orbital (SOMO), $(4n+5)\sigma$, to the lowest unoccupied molecular orbital (LUMO), $(n+2)\pi$, leads to the first electronic excited state $A\ ^2\Pi$ with electronic configuration $...4(n+1)\sigma^2(n+1)\pi^4(4n+5)\sigma^0(n+2)\pi^1$. The calculations indicate that the SOMO orbital $(4n+5)\sigma$ mainly consists of a 3s orbital of Mg and the LUMO orbital $(n+2)\pi$ is dominated

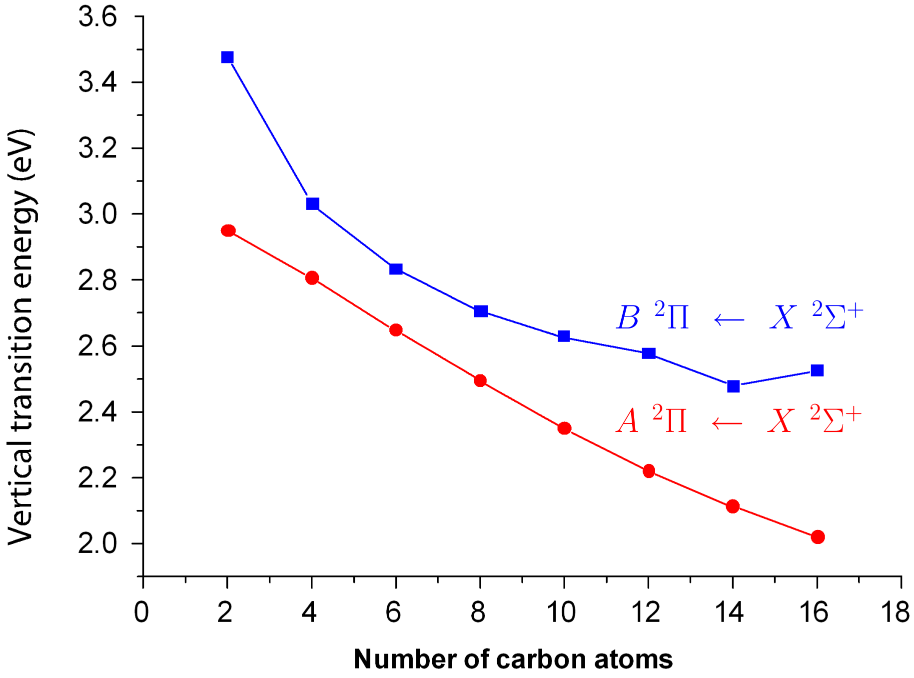

Figure 6.2: Vertical electronic excitation energies of the $A\ ^2\Pi \leftarrow X\ ^2\Sigma^+$ and $B\ ^2\Pi \leftarrow X\ ^2\Sigma^+$ systems for $MgC_{2n}H$ (n=1-8) calculated using the TD-DFT theory with cc-pVTZ basis sets.

by $3p_x/3p_y$ of Mg. The $A\ ^2\Pi \leftarrow X\ ^2\Sigma^+$ transition corresponds to the observed spectra.

Vertical electronic excitation energies were calculated at the ground state geometry for the doublet multiplicity only. These were obtained using TD-DFT for n=1-8 and the RCCSD(T) approach for n=1-3. GAUSSIAN 98 programs[40] and MOLPRO package[41]) were used for the calculations. The values are listed in Table 6.2 and plotted in Figure 6.2. The calculated $A\ ^2\Pi \leftarrow X\ ^2\Sigma^+$ energies at TD-B3LYP level of theory have a typical error of $\sim 0.06\,\text{eV}$ compared to the experimental data. The transition energies of both the $A\ ^2\Pi \leftarrow X\ ^2\Sigma^+$ and $B\ ^2\Pi \leftarrow X\ ^2\Sigma^+$ systems decrease with the chain size (Figure 6.2).

Species	State	T$_0$ (eV)		f
		B3LYP	RCCSD(T)	B3LYP
MgC$_2$H	$X\ ^2\Sigma^+$	0.000	0.00	
	$A\ ^2\Pi$	2.9175	2.8668	0.1300
	$B\ ^2\Pi$	3.5113		0.0073
	$C\ ^2\Sigma^+$	4.3155		0.0100
MgC$_4$H	$X\ ^2\Sigma^+$	0.0	0.0	
	$A\ ^2\Pi$	2.7912	2.8369	0.0870
	$B\ ^2\Pi$	3.0529		0.0178
	$C\ ^2\Sigma^+$	4.4903		0.2891
MgC$_6$H	$X\ ^2\Sigma^+$	0.0	0.0	
	$A\ ^2\Pi$	2.6476	2.8137	0.0495
	$B\ ^2\Pi$	2.8338		0.0198
	$C\ ^2\Sigma^+$	4.3871		0.0296

Table 6.2: Calculated vertical transition energies T$_0$ and oscillator strengths f at the B3LYP and RCCSD(T) levels of theory with cc-pVTZ basis sets for MgC$_{2n}$H (n=1-3).

6.5 Results and discussion

6.5.1 Electronic spectra

The ArF excimer laser multi-photoionization time-of-flight mass spectrum of the products produced by the ablation of magnesium in the presence of a CH$_4$/He supersonic expansion is presented in Figure 6.3. The calculated isotopic ratios (not plotted) fit well with the measured ones. As observed many other species are produced in the ablation but the mass-selected technique employed in this measurements gives an unambiguous assignment of the carriers of the electronic spectra.

The observed spectra of MgC$_2$H, MgC$_4$H and MgC$_6$H in the visible region are shown in Figure 6.4. In the case of MgC$_2$H the observed excitation energy of the origin band at 2.83 eV is close to 2.87 eV as predicted by the RCCSD(T) calculation. The origin bands for MgC$_4$H and MgC$_6$H are at 2.78 eV and 2.74 eV. These are in agreement with the calculated values for the $A\ ^2\Pi \leftarrow X\ ^2\Sigma^+$ system

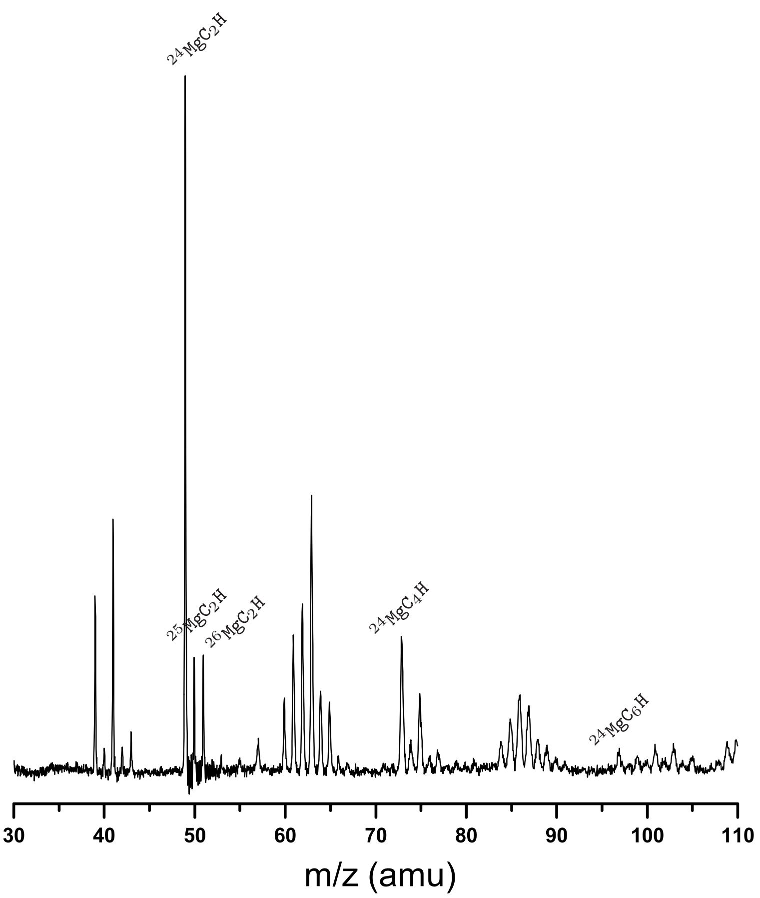

Figure 6.3: The multiphoton ionization time-of-flight mass spectrum of the products of ablated magnesium in the presence of a CH_4/He supersonic expansion.

(Table 6.2). The spin-orbit coupling splitting in the $A\ ^2\Pi$ state of MgC_4H is found to be $\sim 34\,cm^{-1}$. This is close to the value of $35.3\,cm^{-1}$ in MgH and $36.4\,cm^{-1}$ in MgC_2H.[30]

The spectra reveal short vibrational progressions with spacings of $\sim 549\,cm^{-1}$, $\sim 453\,cm^{-1}$ and $\sim 383\,cm^{-1}$ for MgC_2H, MgC_4H and MgC_6H, respectively. The DFT-B3LYP calculations predict that for MgC_2H the frequency of the Mg-C stretch in the ground state is $488\,cm^{-1}$ and $544\,cm^{-1}$ in the $A\ ^2\Pi$ state according to a MRCI calculation.[34] This is in good agreement with the observed value of $549\,cm^{-1}$. In case of MgC_4H the calculations predict that the frequencies of the Mg-C stretch are $398\,cm^{-1}$ in the ground state and $\sim 460\,cm^{-1}$ in the $A\ ^2\Pi$ state;

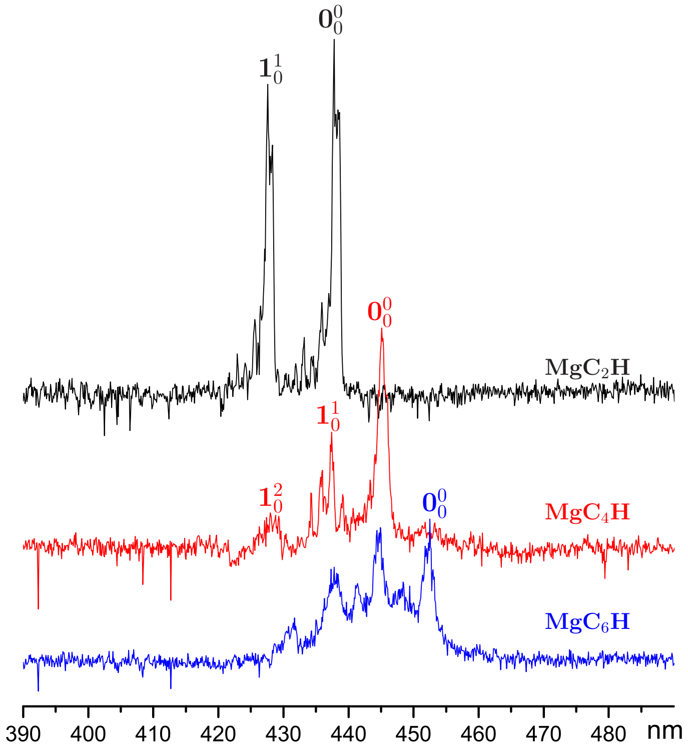

Figure 6.4: Electronic spectra of MgC$_{2n}$H (n=1-3) measured by a resonant two-color two-photon ionization technique in a supersonic molecular beam.

the observed frequency in the latter is $\sim 453\,\mathrm{cm}^{-1}$. Thus the frequency in the $A\,^2\Pi$ state is 7% larger than in the ground state. For MgC$_6$H a similar behavior is expected. Therefore the vibrational progression discernible in the spectra of Figure 6.4 corresponds to the Mg-C stretching motion. The maxima of the detected vibronic bands and their proposed assignment are listed in Table 6.3.

6.5.2 Dipole moment and oscillator strength

The rotational constants (B_e) and dipole moments (D) in the ground state of MgC$_{2n}$H (n=1-8) have been calculated (Figure 6.5). The rotational constant B_e has been fitted:

$$log(B_e) = 4.47754 - 0.46787N + 0.0418N^2 - 0.00219N^3 + 4.58744\times10^{-5}N^4 (MHz), \quad (6.1)$$

	λ (nm)	ν (cm^{-1})	$\Delta\nu$(cm^{-1})	Assignment
MgC_2H	438.3	22809.	0.0	0^0_0 ($A\ ^2\Pi \leftarrow X\ ^2\Sigma^+$)
	428.0	23358	549	ν' (Mg-C)
MgC_4H	445.3	22450	0.0	0^0_0 ($A\ ^2\Pi \leftarrow X\ ^2\Sigma^+$)
	436.5	22903	453	ν' (Mg-C)
	428.4	23336	886	$2\nu'$ (Mg-C)
MgC_6H	452.5	22093	0.0	0^0_0 ($A\ ^2\Pi \leftarrow X\ ^2\Sigma^+$)
	444.8	22476	383	ν' (Mg-C)
	437.9	22830	737	$2\nu'$ (Mg-C)

Table 6.3: Maxima of the vibronic bands in the $A\ ^2\Pi \leftarrow X\ ^2\Sigma^+$ system of $MgC_{2n}H$ and the suggested assignment.

where N=2n=2, 4, 6, ...16. The dipole moment (curve 2 in Fig.6.5) increases monotonically with the size of the chains. This makes the detection of larger $MgC_{2n}H$ chains with microwave spectroscopy easier. A similar behavior has been experimentally observed for cyano substituted carbon chains $NC_{2n+1}H$ (n=1-5), which are among the longest interstellar polyynes detected[16,17] due to their large dipole moments.

The oscillator strength of an electronic transition $n' \leftarrow n$ is defined as:

$$f_{n' \leftarrow n} = \frac{2}{3}(E_{n'} - E_n) \sum \langle n|\mu_\alpha|n'\rangle\langle n'|\mu_\alpha|n\rangle, \tag{6.2}$$

where the energies E_n and dipole components μ_α are in atomic units and the sum is over α. Oscillator strength (f-value) of electronic transition is important for astrophysics. These f values of the $A\ ^2\Pi \leftarrow X\ ^2\Sigma^+$ transition decrease monotonically with the size of the chain while those of the $B\ ^2\Pi \leftarrow X\ ^2\Sigma^+$ system firstly increase from MgC_2H to MgC_4H and then slightly decrease (Figure 6.6). This behavior may arise through mixing of electronic configurations. For the smaller species MgC_2H to MgC_6H, the $A\ ^2\Pi \leftarrow X\ ^2\Sigma^+$ transition loses oscillator strength while $B\ ^2\Pi \leftarrow X\ ^2\Sigma^+$ gains. At larger size it is distributed in a more balanced way between the $A\ ^2\Pi \leftarrow X\ ^2\Sigma^+$ and $B\ ^2\Pi \leftarrow X\ ^2\Sigma^+$ systems.

This is different from the polyyne chains $HC_{2n+1}H$, for which the $B\ ^3\Sigma_u^- \leftarrow X\ ^3\Sigma_g^-$ transition carries most of oscillator strength which increases with n[42]). This is because the f-value in $HC_{2n+1}H$ chains arises from the delo-

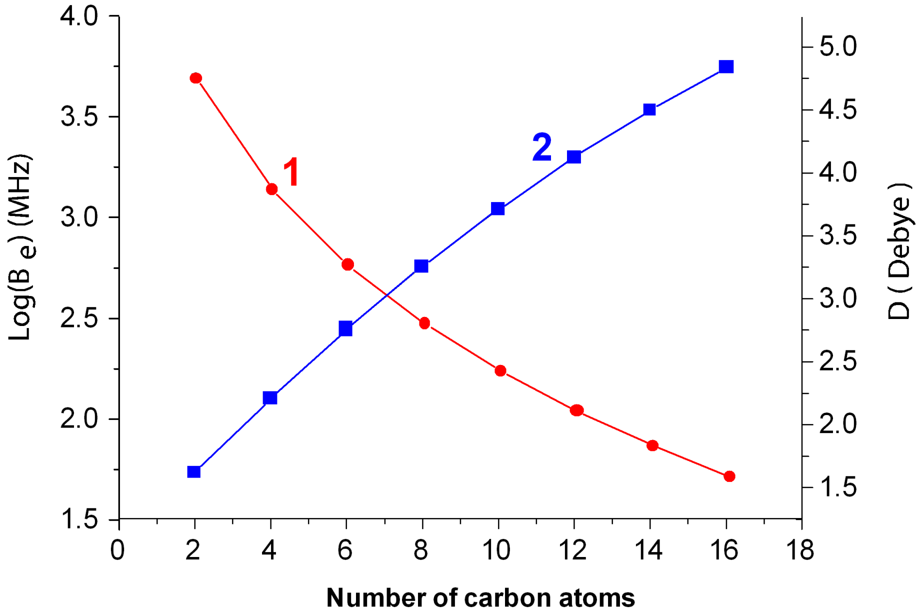

Figure 6.5: Calculated rotational constant (**1**) plotted as log(B_e) and dipole moment, D (**2**) in the ground state for $MgC_{2n}H$ (n=1-8) as a function of the number of carbon atoms, using DFT-B3LYP theory with cc-pVTZ basis sets.

calized π-electron excitation. On the other hand, for $MgC_{2n}H$ the transition is dominated by the promotion of a σ-electron, localized on Mg, and results in a decreasing f-value when the σ-electron becomes more delocalized along the chain for larger n.

6.5.3 Mg-C bonding

The C-C and C-H bond lengths in $MgC_{2n}H$ chains are almost identical with the counterparts of $HC_{2n}H$ chains. However, the study on MgC_2H indicates that the Mg-C bond length in the $A\ ^2\Pi$ state decreases by 2% compared to the ground state.[30,34] For MgC_4H the Mg-C bond lengths are 2.061 Å in the ground and 2.002 Å in the $A\ ^2\Pi$ state. A characteristic of the $MgC_{2n}H$ molecules is that the Mg-C bond length is shorter in the $A\ ^2\Pi$ than that in the ground state while the Mg-C vibrational frequency is higher in the $A\ ^2\Pi$ state.

It has been suggested that this is due to a stronger Mg-C bonding in the excited than in the ground state,[30] but computations did not confirm this and indicate that

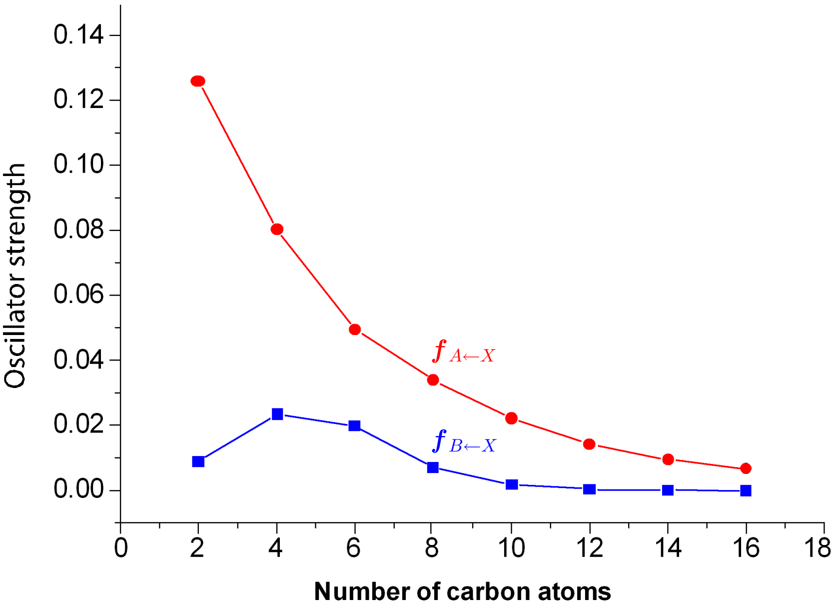

Figure 6.6: Oscillator strengths of the $A\ ^2\Pi \leftarrow X\ ^2\Sigma^+$ and $B\ ^2\Pi \leftarrow X\ ^2\Sigma^+$ transition systems for $MgC_{2n}H$ (n=1-8) calculated using the TD-DFT theory with cc-pVTZ basis sets.

if curve crossings were not present (see Fig.1 in Woon 1997[34]), the energy required to dissociate $A\ ^2\Pi$ MgC_2H to Mg (^3P) + C_2H ($^2\Sigma^+$) is 71.9 kcal mol^{-1} at the estimated RCCSD(T) CBS limit, about 5 kcal mol^{-1} less than the 76.8 kcal mol^{-1} value for the ground state.[34] The potential energy curves of the ground state and $A\ ^2\Pi$ state of MgC_4H as a function of Mg-C coordinate have been calculated at RCCSD(T)/cc-pVTZ level of theory. This shows that the ground state dissociates with no barrier to Mg (^1S) + C_4H ($^2\Sigma^+$) with energy of 78.3 kcal mol^{-1} (Fig. 6.7). An avoided crossing is indicated for the $A\ ^2\Pi$ state. This state correlates with the Mg (^3P) + C_4H ($^2\Sigma^+$) asymptote (not plotted in Fig.6.7).

The latter products correlate with the initially repulsive $B\ ^2\Pi$ state of MgC_4H. The calculated dissociation energy of $A\ ^2\Pi$ of MgC_4H is 73.4 kcal/mol to Mg (^3P) + C_4H ($A\ ^2\Pi$) with a small barrier. This demonstrates that the bonding energy in the ground state is stronger than that in the $A\ ^2\Pi$ state for MgC_4H. The major reason for a shorter bond-length of Mg-C in $A\ ^2\Pi$ is due to its molecular orbital nature. Since the SOMO orbital, $(4n+5)\sigma$, has anti-bonding character, electron promotion from $(4n+5)\sigma$ to the LUMO orbital, $(n+2)\pi$ leads to a Mg-C bond-

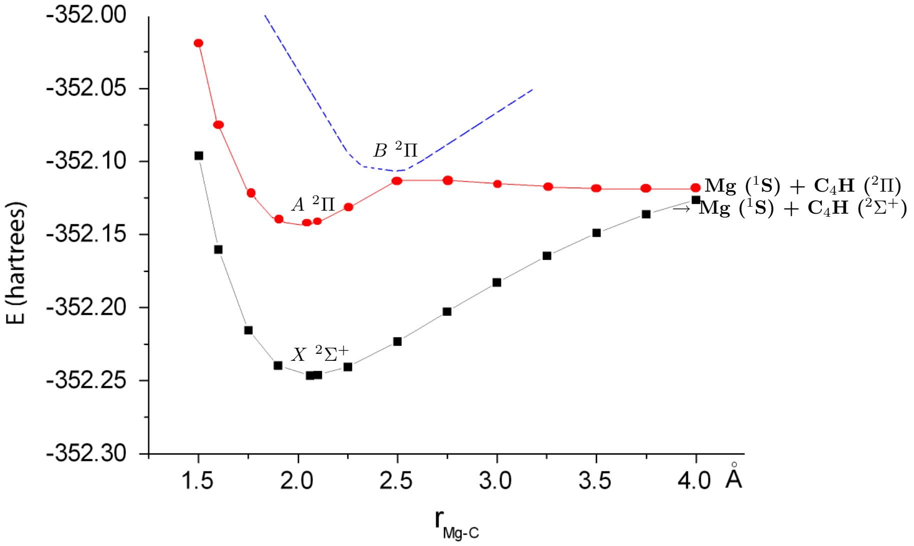

Figure 6.7: Calculated potential energy curves of the $X\ ^2\Sigma^+$ and $A\ ^2\Pi$ states for MgC_4H as a function of Mg-C bond-length using the RCCSD(T)/cc-pVTZ level of theory.

length contraction, as noted in the study on MgC_2H.[34] The occupied $(n+2)\pi$ orbital leads to a Mg-C bond-length decrease and enhances the harmonic force for the Mg-C stretch motion, as experimentally observed. A similar behavior has been found for other metal containing molecules such as CaC_2H and SrC_2H.[28,29,32]

6.6 Concluding remarks

The electronic transitions of magnesium substituted carbon chains $MgC_{2n}H$ have a significantly different character compared to highly unsaturated carbon chains such $HC_{2n}H$. Although the dipole moment of $MgC_{2n}H$ increases with the chain's size, the oscillator strength of the allowed electronic transitions decreases. This has a consequence that the electronic spectrum for the longer chains becomes more difficult than to observe their microwave transition in the ground state. The laboratory gas-phase electronic spectra of MgC_2H, MgC_4H and MgC_6H allow a comparison with the catalog of the diffuse interstellar bands (DIBs).[43] No match was found between the laboratory bands and the DIBs. Nevertheless, the presented laboratory data on electronic transitions of these magnesium containing carbon chains in the optical spectrum provides means of their detection by astronomers in space. The bonding energy of Mg-C was calculated as $\sim$ 78 kcal/mol (3.4 eV). This suggests that MgC_2H, MgC_4H and MgC_6H may be destroyed by UV light in the gas-phase but could remain on the surface of dust grains in molecular clouds.

Bibliography

[1] L. M. Ziurys, A. J. Apponi, M. Guélin, and J. Cernicharo, Astrophys. J. **445**, L47 (1995).

[2] U. J. Sofia, J. A. Cardelli, and B. D. Savage, Astrophys. J. **430**, 650 (1994).

[3] M. A. Anderson and L. M. Ziurys, Astrophys. J. **452**, L157 (1995).

[4] R. P. A. Bettens and E. Herbst, Astrophys. J. **478**, 585 (1997).

[5] E. Herbst, H.-H. Lee, D. A. Howe, and T. J. Millar, Mon. Not. R. Astron. Soc. **268**, 335 (1994).

[6] T. J. Millar and E. Herbst, Astron. Astrophys. **288**, 561 (1994).

[7] E. F. V. Dishoeck and J. H. Black, Astrophys. J. Suppl. Ser. **62**, 109 (1986).

[8] J. P. Maier, N. M. Lakin, G. A. H. Walker, and D. A. Bohlender, Astrophys. J. **553**, 267 (2001).

[9] J. P. Maier, G. A. H. Walker, and D. A. Bohlender, Astrophys. J. **566**, 332 (2002).

[10] M. B. Bell et al., Astrophys. J. **518**, 740 (1999).

[11] M. C. McCarthy, M. J. Travers, A. Kovacs, C. A. Gottlieb, and P. Thaddeus, Astrophys. J. Suppl. Ser. **113**, 105 (1997).

[12] M. C. McCarthy, E. S. Levine, A. J. Apponi, and P. Thaddeus, J. Mol. Spectrosc. **203**, 75 (2000).

[13] J. Cernicharo et al., Astrophys. J. **546**, L123 (2001).

[14] J. Cernicharo et al., Astrophys. J. **546**, L127 (2001).

[15] S. J. Kim, J. Caldwell, R. A. Rivolo, R. Wagener, and S. G. Orton, Mon. Not. R. Astron. Soc. **64**, 233 (1985).

[16] N. W. Broten, T. Oka, L. W. Avery, J. M. Macleod, and H. W. Kroto, Astrophys. J. **223**, L105 (1978).

[17] M. B. Bell, S. Kwok, P. A. Feldman, and H. E. Matthews, Nature **295**, 389 (1982).

[18] H. W. Kroto, J. R. Heath, S. C. O'Brian, R. F. Curl, and R. E. Smalley, Astrophys. J. **314**, 352 (1987).

[19] B. E. Turner, S. Petrie, R. C. Dunbar, and G. Langston, Astrophys. J. **621**, 817 (2005).

[20] M. Guélin, J. Cernicharo, C. Kahane, and J. Gomez-Gonzalez, Astron. Astrophys. **157**, L17 (1986).

[21] K. Kawaguchi, E. Kagi, T. Hirano, S. Takano, and S. Saito, Astrophys. J. **406**, L39 (1993).

[22] M. A. Anderson and L. M. Ziurys, J. Phys. Chem. B **231**, 164 (1994).

[23] J. Cernicharo and M. Guélin, Astron. Astrophys. **183**, L10 (1987).

[24] L. M. Ziurys, A. J. Apponi, and T. G. Phillips, Astrophys. J. **433**, 729 (1994).

[25] T. Tsuji, Astron. Astrophys. **23**, 411 (1973).

[26] C. M. Sharp and W. F. Huebner, Astrophys. J. Suppl. Ser. **72**, 417 (1990).

[27] M. Guélin, R. Lucas, and J. Cernicharo, Astron. Astrophys. **280**, L19 (1993).

[28] A. M. R. P. Bopegedera, C. R. Brazier, and P. F. Bernath, Chem. Phys. Lett. **136**, 97 (1987).

[29] M. G. Li and J. A. Coxon, J. Mol. Spectrosc. **176**, 206 (1996).

[30] G. K. Corlett, A. M. Little, and A. M. Ellis, Chem. Phys. Lett. **249**, 53 (1996).

[31] G. K. Corlett, M. S. Beardah, and A. M. Ellis, J. Mol. Spectrosc. **185**, 202 (1997).

[32] M. J. Dick, P. M. Sheridan, J. G. Wang, and P. F. Bernath, J. Mol. Spectrosc. **233**, 197 (2005).

[33] D. E. Woon and E. Herbst, Astrophys. J. **465**, 795 (1996).

[34] D. E. Woon, Chem. Phys. Lett. **274**, 299 (1997).

[35] H. Ding, M. D. Morse, C. Apetrei, L. Chacaga, and J. P. Maier, J. Chem. Phys. **125**, 194315 (2006).

[36] A. D. Becke, J. Chem. Phys. **98**, 5648 (1993).

[37] J. D. Watts, J. Gauss, and R. J. Bartlett, J. Chem. Phys. **98**, 8718 (1993).

[38] D. E. Woon and T. H. Dunning, J. Chem. Phys. **98**, 1358 (1993).

[39] R. E. Stratmann, G. E. Scuseria, and M. J. Frisch, J. Chem. Phys. **109**, 8218 (1998).

[40] M. J. Frisch et al., Gaussian98, Revision A.7, Gaussian Inc., Pittsburgh PA, 1998.

[41] H. J. Werner et al., MOLPRO, version 2006.1, a package of ab initio programs written by, http://www.molpro.net.

[42] H. Ding et al., J. Chem. Phys. **119**, 814 (2003).

[43] P. Jenniskens and F. X. Desert, Astron. Astrophys. Suppl. Ser. **106**, 39 (1994).

7 Gas phase electronic spectrum of T-shaped AlC_2 radical

7.1 Abstract

Gas phase electronic transitions for the $\tilde{C}\ ^2B_2 \leftarrow \tilde{X}\ ^2A_1$ and $\tilde{D}\ ^2B_1 \leftarrow \tilde{X}\ ^2A_1$ band systems of T-shaped AlC_2 (C_{2v}) radical have been measured in the 345–475 nm range. Vibrational analyses of both band systems are reported. Simulation of several rotationally resolved bands confirms previously obtained rotational parameters for the $\tilde{C}\ ^2B_2$ state. The radical is produced by ablating an aluminium rod in the presence of acetylene gas. The resulting supersonic molecular beam is probed using both mass-selective resonant two-color, two-photon ionization and laser induced fluorescence. *Ab initio* calculations and vertical electronic excitation energies help the assignment. Vibrational frequencies for the $\tilde{X}\ ^2A_1$, $\tilde{C}\ ^2B_2$, and $\tilde{D}\ ^2B_1$ states have been determined. Rotational analysis of a number of bands yields spectroscopic constants for one vibronic state in the $\tilde{C}\ ^2B_2$ manifold and the origin band of the $\tilde{D}\ ^2B_1 \leftarrow \tilde{X}\ ^2A_1$ system.

7.2 Introduction

The relationship between the structure of organometallic species and the nature of the carbon-metal chemical bonding remain a topic of considerable interest. Such clusters provide an opportunity to understand these interactions and to gain insight into the growth mechanisms of metal-carbon nanomaterials. Of these, metal carbides and dicarbides represent an important chemical class with application in a wide range of processes and materials. However, spectroscopic information that could reveal aspects of metal-carbon bonding at the triatomic level is relatively sparse.

Metal-containing carbon compounds are also of interest in astrochemistry, where a few such molecules have been detected in carbon rich astrophysical environments through their microwave and sub-mm/mm transitions.[1–3] Because many elements such as magnesium, iron, and sodium are depleted in molecular clouds,[4] the central question concerns the form in which these metal-containing species exist in the interstellar medium (ISM). It is generally believed that the most refractory elements are condensed out onto the surface of dust grains. Unfortunately, knowledge about the gas-phase abundances and the surface absorption of such species in the ISM is limited. Accordingly, the spectroscopic identification of metal-containing molecular carriers has implication for both gas-phase and grain chemistry.[3]

To date, eleven main group dicarbides have been investigated spectroscopically (XC_2, X=H, B, C, N, O, Al, Si, P, S, Cl, As).[5] HC_2, NC_2,[6] OC_2,[7] PC_2,[5] SC_2,[8] and AsC_2[5] all possess linear ($C_{\infty v}$) structures. ClC_2 has been shown to have bent shaped $\tilde{X}\ ^2A'$ ground state,[9] while AlC_2 and SiC_2 are T-shaped (C_{2v}).[10,11] Matrix infrared and electronic spectra of BC_2, which is isovalent with AlC_2, have been obtained with features assigned to a cyclic structure.[12,13] As far as heavier systems are concerned, the $\tilde{A}\ ^2A_1 \leftarrow \tilde{X}\ ^2A_1$ transition of the T-shaped YC_2 radical has been studied extensively in vibrational, rotational, and hyperfine detail.[14–16]

At high temperatures, vaporous metal dicarbides are the predominant species in thermodynamic equilibrium with metal-carbon condensed systems.[17–19] Aluminium dicarbide was first detected in a high temperature Knudsen cell using mass spectrometry.[18] The study indicated that the atomization energy of AlC_2 is 1104 ± 21 kJ mol^{-1} and the dissociation energy of $Al-C_2$ is 514.2 ± 21 kJ mol^{-1}. The latter is slightly higher than the dissociation energy of AlO, and thus an apparent exception to the empirical rule that the dissociation energy of a $M-C_2$ bond is usually 40−130 kJ mol^{-1} less than the corresponding M−O bond.[18]

Photoelectron spectroscopy of AlC_2^- revealed a vibrational progression of 590 cm^{-1}, which was assigned as the stretching mode of the neutral $Al-C_2$.[20] Theoretical calculations have provided estimates for all three vibrational frequencies for AlC_2, none of these have yet been observed in the infrared.[10,21,22]

Ablation of an aluminium rod in the presence of a C_2H_2 / He gas mixture together with photoionization mass spectrometry with 7.9 eV photons, yielded ions at m/z 51 consistent with the mass of AlC_2. The implication that AlC_2 possesses a stable structure in the gas phase was established using laser induced fluorescence (LIF). Confirmation of its T-shaped (C_{2v}) structure emerged from the measurement of the $\tilde{C}\ ^2B_2 \leftarrow \tilde{X}\ ^2A_1$ transition of AlC_2. Rotational analysis for the origin band provided estimates for the $\tilde{C}\ ^2B_2$ state molecular parameters.[10]

In this paper the gas-phase electronic spectrum of AlC_2 is investigated over a broad spectral range using both a mass-selective resonant two-color two-photon ionization (R2C2PI) technique and LIF. The $\tilde{C}\ ^2B_2 \leftarrow \tilde{X}\ ^2A_1$ origin band has been confirmed and new vibronic bands are observed. *Ab initio* calculations on T-shaped AlC_2 (C_{2v}) have been carried out to guide the assignments.

7.3 Experimental

Jet cooled AlC_2 was produced using laser vaporization of an aluminium rod (30 mJ / 5 ns pulse from a 532 nm Nd^{3+}:YAG, focused to 0.3 mm) in the presence of a 1-5% acetylene gas mixture seeded in either helium or argon provided by a 0.3 mm orifice pulsed valve. The rod was rotated and translated so that a fresh surface was continuously exposed to the laser, which was fired to coincide with the gas flow over the target area. The ablation plume flows through a channel (3 mm diameter, 5-15 mm long) before entering vacuum. The resulting free-jet expansion is probed using the mass-selective R2C2PI technique[23] or LIF.

R2C2PI spectra were collected by probing the skimmed beam of the jet expansion. Ions were removed by applying a perpendicular electric field before entering the ionization region of a Wiley-McLaren time-of-flight mass spectrometer.[24] Neutral molecules were irradiated with a pulse of tunable ultraviolet-visible radiation, followed by 7.9 eV photons from an F_2 excimer laser. Ions were then extracted into a time-of-flight tube where the signal from a microchannel plate ion-detector was sent to a fast oscilloscope and data acquisition card. The combination of the UV-VIS and the 157 nm photons was sufficient to ionize AlC_2. Low resolution spectra for the vibronic survey scans were collected over the 355 - 500 nm range using an OPO system ($\sim 5\,cm^{-1}$ bandwidth). A pulsed dye laser was used ($\sim 0.15\,cm^{-1}$ bandwidth, $\sim$ 5 mJ/pulse) for the rotationally resolved work, with calibration through the use of an optogalvanic spectrum obtained from a Fe/Ne hollow cathode lamp.

LIF spectra were measured using an excimer pumped dye laser (bandwidth 0.15 cm^{-1}). Fluorescence signal was collected by an $f/1$ lens and detected using a photomultiplier and digital oscilloscope.

7.4 Theoretical Calculations

The electronic ground state structures of AlC_2 were investigated using both coupled cluster RCCSD(T) theory[25] and the hybrid density B3LYP functional[26] with Dunning's correlation-consistent basis sets.[27] The calculations indicate that T-shaped AlC_2 (C_{2v}) is a global minimum. Linear AlCC ($C_{\infty v}$) and CAlC ($D_{\infty h}$) are local minima lying approximately 0.4 eV and 7 eV higher in energy, respectively.

Transition	T_v(eV)			f
	CAS	MRCI	MRCI+Q	CAS
$\tilde{A}\ ^2A_1 \leftarrow \tilde{X}\ ^2A_1$	1.19	1.27	1.49	$2.8{\cdot}10^{-2}$
$\tilde{B}\ ^2B_1 \leftarrow \tilde{X}\ ^2A_1$	2.21	2.37	2.46	$7.5{\cdot}10^{-4}$
$\tilde{C}\ ^2B_2 \leftarrow \tilde{X}\ ^2A_1$	2.76	2.83	2.73	$1.5{\cdot}10^{-2}$
$\tilde{D}\ ^2B_1 \leftarrow \tilde{X}\ ^2A_1$	2.97	3.31	3.31	$7.8{\cdot}10^{-3}$
$\tilde{E}\ ^2B_2 \leftarrow \tilde{X}\ ^2A_1$	3.59	3.89	3.83	$1.5{\cdot}10^{-2}$
$\tilde{F}\ ^2A_1 \leftarrow \tilde{X}\ ^2A_1$	4.21			$1.8{\cdot}10^{-3}$
$\tilde{G}\ ^2A_2 \leftarrow \tilde{X}\ ^2A_1$	4.70			0.0

Table 7.1: Calculated vertical transition energies (T_v) and oscillator strengths (f) with CASSCF, MRCI, MRCI+Q theories with cc-pVTZ basis sets for T-shaped AlC_2 (C_{2v}).

Equilibrium geometries for the ground state were optimized using the B3LYP/aug-cc-pVQZ theory and RCCSD(T)/cc-pVTZ approach. Previously[10] theoretical calculations of excited electronic states of AlC_2 (C_{2v}) were carried out using the complete active space self-consistent field method (CASSCF)[28] and multi-reference configuration interaction (MRCI) theory.[29] Vertical excitation energies were calculated for states up to 3.8 eV above the ground state. In order to predict the spectrum in the UV region, higher lying states for AlC_2 (C_{2v}) have been investigated with CASSCF and MRCI approaches using the Gaussian 98 suite of programs [30] and MOLPRO package.[31] The resulting vertical transition energies and oscillator strengths are summarized in Table 7.1.

7.5 Results and discussions

The R2C2PI low resolution ($\sim 5\,\mathrm{cm}^{-1}$ bandwidth) electronic spectra of the $\tilde{C}\,^2B_2 \leftarrow \tilde{X}\,^2A_1$ and $\tilde{D}\,^2B_1 \leftarrow \tilde{X}\,^2A_1$ systems of AlC_2 for the 345-475 nm range are shown in Figures 7.1 and 7.6, respectively. The wavelengths of the vibronic bands (maxima) and suggested assignments are listed in Table 7.2.

$\tilde{\nu}$	$\Delta\tilde{\nu}$	Assignment
		$\tilde{C}\,^2B_2 \leftarrow \tilde{X}\,^2A_1$
22098	0.0	0^0_0
22305	207	2^1_0
22498	400	2^2_0
22682 [a]	584	3^1_0, 2^3_0
(22678, 22713)	(580, 613)	
22879	781	$3^1_0 2^1_0$
23309	1211	3^2_0
23496	1398	1^1_0
23710	1612	$2^1_0 1^1_0$
24733	2635	$3^2_0 1^1_0$
24880	2782	1^2_0
		$\tilde{D}\,^2B_1 \leftarrow \tilde{X}\,^2A_1$
26073	0.0	0^0_0
26475	402	3^2_0
26616	543	2^1_0
27055	982	$3^2_0 2^1_0$
27186	1113	2^2_0
27563	1490	1^1_0, 2^3_0, $3^2_0 2^2_0$

Table 7.2: Vibrational band maxima (cm^{-1}) in the $\tilde{C}\,^2B_2 \leftarrow \tilde{X}\,^2A_1$ and $\tilde{D}\,^2B_1 \leftarrow \tilde{X}\,^2A_1$ band systems of AlC_2. [a]Higher resolution studies show that the band at $22\,682\,\mathrm{cm}^{-1}$ is actually consists of two overlapping bands at 22 678 and $22\,713\,\mathrm{cm}^{-1}$.

7.5.1 $\tilde{C}\ ^2\mathrm{B}_2 \leftarrow \tilde{X}\ ^2\mathrm{A}_1$

Previous coupled cluster calculations (CCSD(T)) estimate the harmonic frequencies of ground state $\tilde{X}\ ^2\mathrm{A}_1$ AlC_2 as ν_1=1735 (a_1), ν_2=645 (a_1) and ν_3=421 (b_2) cm^{-1}.[10] These frequencies were thus used as a starting point in assigning the low resolution $\tilde{C}\ ^2\mathrm{B}_2 \leftarrow \tilde{X}\ ^2\mathrm{A}_1$ spectrum depicted in Figure 7.1. Higher resolution rotationally resolved spectra were obtained to assist in confirming the most probable identities of the vibrational bands.

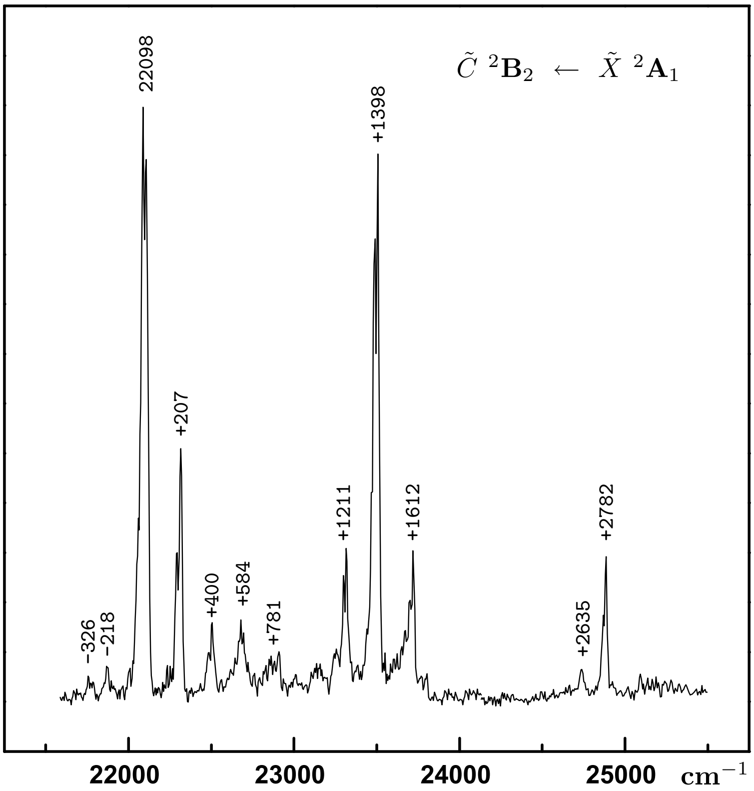

Figure 7.1: Low resolution (5 cm^{-1} bandwidth) spectrum of the $\tilde{C}\ ^2\mathrm{B}_2 \leftarrow \tilde{X}\ ^2\mathrm{A}_1$ electronic system for the T-shaped AlC_2 radical, recorded in the range 21 000−26 000 cm^{-1} using a resonant two-color, two-photon ionization technique in a supersonic molecular beam.

The observed rotational structure of the $\tilde{C}\ ^2\mathrm{B}_2 \leftarrow \tilde{X}\ ^2\mathrm{A}_1$ origin band of AlC_2 is consistent with that expected for an electric dipole allowed perpendicular *b*-type transition in a C_{2v} molecule.[10] Accordingly, transitions involving a_1 modes are also electric dipole allowed, and will be observed as *b*-type perpendicular.

However, those involving non-totally symmetric b_2 vibrations, in the absence of vibronic coupling, are only allowed as even quantum changes (i.e. Franck-Condon allowed). These $\Delta v = \pm 2$ transitions will also display rotational contours with *b*-type perpendicular band structure. Using these guidelines, assignments may be made, starting with the dominant 22 108 cm^{-1} band in Figure 7.1, which has been already confirmed as the origin.[10]

The rotational resolved R2C2PI spectrum of the +1398 cm^{-1} band in the $\tilde{C}\ ^2B_2 \leftarrow \tilde{X}\ ^2A_1$ transition is shown in Figure 7.2, accompanied by a spectral simulation, assuming a *b*-type perpendicular band for a near-prolate symmetric top, performed using the WANG program.[32] The band is assigned as the 1_0^1 transition, where ν_1 is the C=C stretching mode. The measured excited state ($\tilde{C}$) frequency of $\nu_1^{'}$=1398 cm^{-1} compares with the calculated ground state frequency for $\nu_1^{''}$ of 1735 cm^{-1}. The reduction in the C=C stretching frequency relative to the ground state is consistent with the lengthening of the C=C bond in the $\tilde{C}$ state (both calculation and estimated rotational constants are in support of this). The significant Franck-Condon activity in ν_1 is also consistent with the appreciable lengthening of the C=C bond bond in the $\tilde{C}$ state relative to the ground state. Spectroscopic constants for $\nu_1^{'}$ vibronic level have been estimated from the spectral simulation with constants reported in Table 7.3.

However it must be recognized that difficulties can arise in fitting the finer features of the observed spectrum due to the potential perturbations in the $\tilde{C}\ ^2B_2$ manifold arising as a result of interactions with rovibronic levels of the underlying $\tilde{B}$ state.[10] Nevertheless the simulation is quite acceptable.

The second progression member in $\nu_1^{'}$, i.e. the 1_0^2 transition, is observed at +2782 cm^{-1} (Figure 7.1) and displays a *b*-type perpendicular rotational band contour with a shape quite similar to those shown in Figure 7.3, thus being associated with transition involving progressions in a_1 modes or even-quantum-change overtones.

Figure 7.3 displays the origin band for the $\tilde{C}\ ^2B_2 \leftarrow \tilde{X}\ ^2A_1$ transition at 452 nm (22 098 cm^{-1}), recorded using an excimer pumped dye laser (0.15 cm^{-1} resolution) and LIF detection. The extended *K*-rotational structure observed is consistent with its interpretation as a *b*-type perpendicular band for a near-prolate symmetric top. Below the spectrum two vibronic transitions observed at +207, and +400 cm^{-1} with respect to the origin. The intensity of the +207 cm^{-1} band is

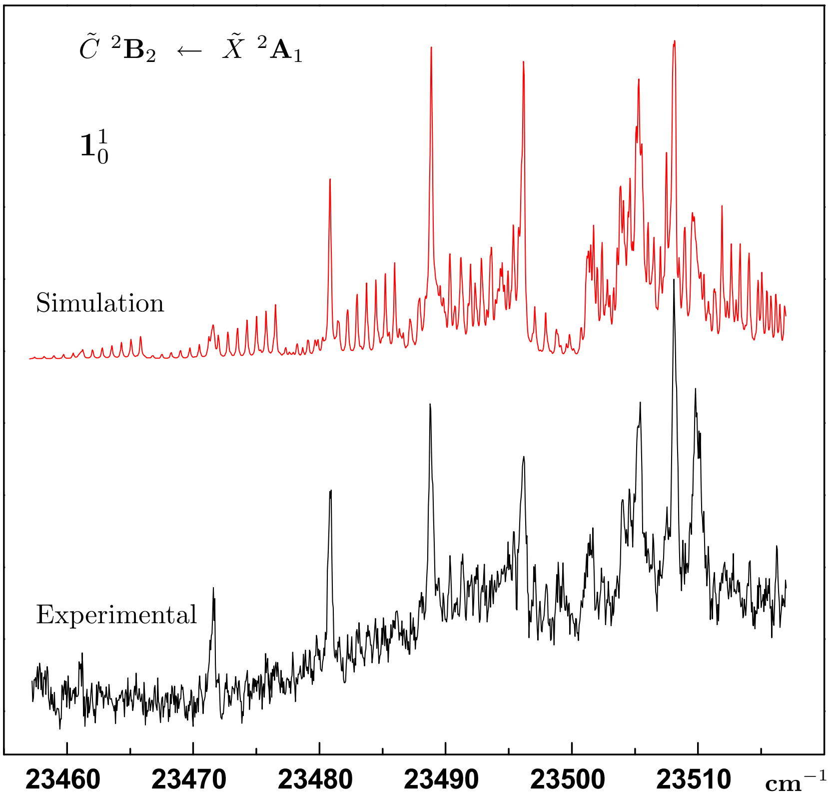

Figure 7.2: Rotationally resolved resonant two-color, two-photon ionization spectrum (0.15 cm^{-1} bandwidth) of the 23 496 cm^{-1} band in the $\tilde{C}\ ^2B_2 \leftarrow \tilde{X}\ ^2A_1$ AlC$_2$ band system and a rotational contour simulation.

approximately one-third that of the origin, while that for +400 cm^{-1} is less again by a factor approximately four. The pattern of relative intensities, as well as the contour being the same as that of the origin band, is consistent with a progression in a totally symmetric mode. Accordingly, the +207 and +400 cm^{-1} bands are assigned as first two progression members involving the ν_2 (Al$-$C$_2$ stretch), with an approximate value of ν_2'=207 cm^{-1}. The appreciable anharmonicity observed is consistent with a large frequency change occurring for ν_2 between the $\tilde{X}$ and $\tilde{C}$ states (the calculated value for ν_2'' is 645 cm^{-1}), indicating a much shallower ν_2 potential function in the $\tilde{C}$ state. The 2_0^2 transition, bottom plot, overlaps with the 0$-$0 and 1$-$1 bands of the $\tilde{B}\ ^4\Sigma^- \leftarrow \tilde{X}\ ^4\Sigma^-$ AlC transition, and therefore the trace shown has been obtained using a normalized spectral substraction to remove

	$\tilde{X}\ ^2A_1$ [a]	$\tilde{C}\ ^2B_2$	$\tilde{D}\ ^2B_1$
		1_0^1	0_0^0
A	1.7093(107)	1.5695(98)	1.743(50)
B	0.4052(50)	0.4035(50)	0.355(49)
C	0.3228(49)	0.321(45)	0.295(94)
T_0		23499.7 ± 0.2	26083.2 ± 0.2
r_{Al-C}	1.928 [b]	1.950 [b]	2.095 [c]
r_{C-C}	1.276 [b]	1.321 [b]	1.27 [c]
α_{C-Al-C}	38.7° [b]	39.6° [b]	35.3° [c]

Table 7.3: Molecular parameters (cm^{-1}) determined from the least square fit of the spectrum for AlC_2, $\tilde{C}\ ^2B_2 \leftarrow \tilde{X}\ ^2A_1$ (1_0^1) and $\tilde{D}\ ^2B_1 \leftarrow \tilde{X}\ ^2A_1$ (0_0^0). Values in parenthesis denote 2σ standard deviation. [a] Ref. 10. Optimized geometries for the $\tilde{X}\ ^2A_1$, $\tilde{C}\ ^2B_2$ (0_0^0) and $\tilde{D}\ ^2B_1$ (0_0^0) state at CASSCF ([b] Ref. 10) and SA-CASSCF level of theories ([c] Ref. 33).

the contamination from the AlC diatomic fluorescence. This was possible due to the fact that the above mentioned transition in AlC has a longer fluorescence lifetime than that of AlC_2, thus allowing the collection of a decongested spectrum of the diatomic through gating the tail end of the LIF decay and later subtracting it from the total signal containing fluorescence from both species.

Based on the assignment ν_2'=207 cm^{-1} for the $\tilde{C}$ state, the two bands observed towards lower energy from the $\tilde{C}\ ^2B_2 \leftarrow \tilde{X}\ ^2A_1$ origin (Figure 7.1, -218 and -326 cm^{-1}) are both candidates for the 2_1^1 sequence band. Our preferred assignment for the -326 cm^{-1} band is 2_1^1 which yields ν_2''=533 cm^{-1} compared with ν_2''=645 cm^{-1} from calculation. Despite the supersonic free jet environment vibrational cooling may not be that efficient in the helium carrier gas, hence it is not unexpected that there is thermal population in the ν_2'',v=1 level.

LIF spectra (0.15 cm^{-1} resolution) recorded for three more transitions at 421, 425, and 428 nm are shown in Figure 7.4. These correspond to the bands showed in Figure 7.1 at +1211, +1398 and +1612 cm^{-1} with respect to the origin.

The band observed at +1211 cm^{-1} from the origin (Figure 7.1) is shown in high resolution detail as the top trace in Figure 7.4. The observed band contour indicates a totally symmetric transition. The most compelling assignment is the

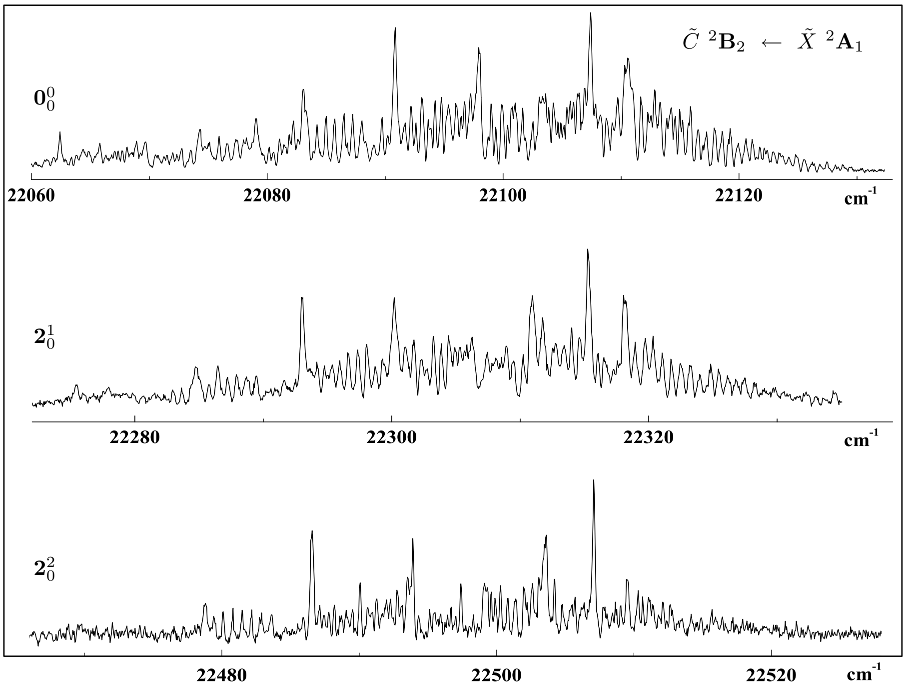

Figure 7.3: Rotationally resolved laser induced fluorescence spectra (0.15 cm^{-1} bandwidth) of the 22 098, 22 305, and 22 498 cm^{-1} transitions in the $\tilde{C}\ ^2\mathrm{B}_2 \leftarrow \tilde{X}\ ^2\mathrm{A}_1$ AlC$_2$ band system.

Franck-Condon allowed Δv=2 transition involving excitation in ν_3, i.e. 3_0^2. This yields an approximate frequency of 605 cm^{-1} for ν_3 in the $\tilde{C}$ state.

The lowest trace in Figure 7.4 is for the band observed at +1612 cm^{-1}. The frequency is close to the combination of the observed frequencies for ν_1' and ν_2', i.e. 1398+207=1605 cm^{-1}. Accordingly, this transition is assigned as the $2_0^1 1_0^1$ combination band. The *b*-type perpendicular *K*-structure is also as expected for a combination involving two a$_1$ modes.

Finally, the LIF spectrum (0.15 cm^{-1} resolution) recorded in the region near 440 nm (Figure 7.1, +584 cm^{-1}) is presented in Figure 7.5. Measurement at higher resolution provides clear indication that this does not conform to a *b*-type perpendicular transition. Figure 7.5 includes rotational band contour simulations for an *a*-type parallel band centered at $\sim$ 22 678 cm^{-1} and a *b*-type perpendicular band (intensity $\sim$ 30% that of the parallel band) at $\sim$ 22 713 cm^{-1}. The third member of the ν_2 progression, i.e. 2_0^3 excitation, is expected to lie in this region

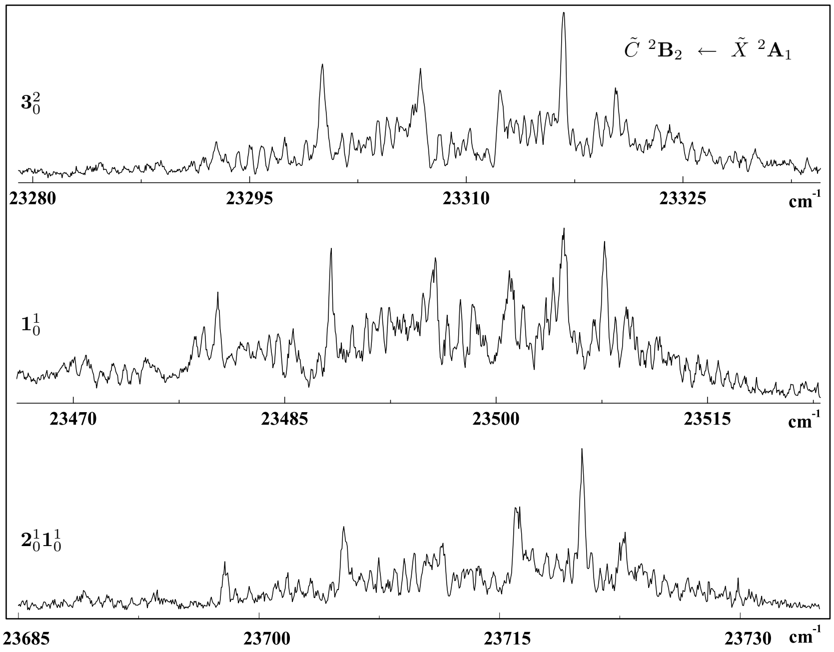

Figure 7.4: Rotationally resolved laser induced fluorescence spectra (0.15 cm^{-1} bandwidth) of the 23 309, 23 496, and 23 710 cm^{-1} transitions in the $\tilde{C}$ ^{2}B$_2$ ← $\tilde{X}$ ^{2}A$_1$ AlC$_2$ band system.

and would be responsible for the *b*-type perpendicular band. Added together, this combined simulation matches the overall spectral structure in the region 22 640 to 22 740 cm^{-1} quite well.

An *a*-type parallel band derives intensity from the dipole-allowed T$_z$ transition moment, implying that the vibronic symmetry associated with the +584 cm^{-1} band is A$_1$. The conclusion advanced is that the +584 cm^{-1} band corresponds to the transition 3^1_0 where the ν_3 vibrational mode (b$_2$ symmetry; $\tilde{C}$ state vibronic symmetry=b$_2 \otimes$ B$_2$=A$_1$) derives intensity through vibronic coupling with the strong, T$_z$ dipole-allowed $\tilde{A}$ ^{2}A$_1$ ← $\tilde{X}$ ^{2}A$_1$ transition. The $\tilde{A}$ state is calculated to lie approximately 12 000 cm^{-1} below the $\tilde{C}$ state. The fact that the ν_3,v=1 vibrational frequency has increased in the $\tilde{C}$ state relative to the $\tilde{X}$ state (ν_3 ground state frequency calculated as 421 cm^{-1}) is consistent with the $\tilde{A}$ ^{2}A$_1$ electronic state, from which intensity is borrowed, lying lower in energy than the $\tilde{C}$ state.

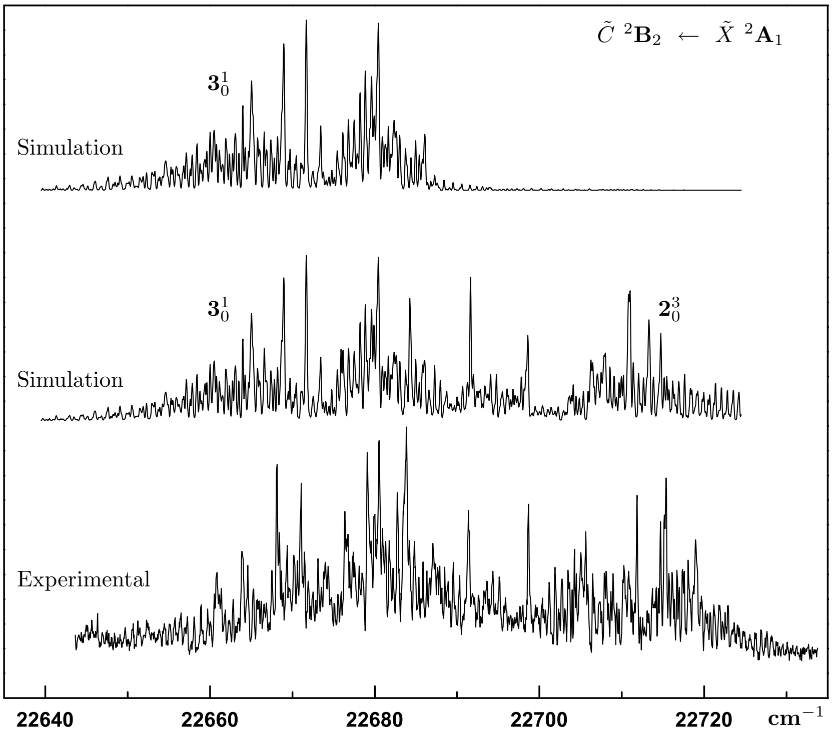

Figure 7.5: Rotationally resolved laser induced fluorescence spectrum ($0.15\,cm^{-1}$ bandwidth) of the $\tilde{C}\ ^2B_2 \leftarrow \tilde{X}\ ^2A_1$ AlC_2 band system (Figure 7.1, $+584\,cm^{-1}$). Rotational contour simulations for an a-type parallel and a mixture of both a-type parallel band and b-type perpendicular bands are shown above the experimental spectrum.

Hence we conclude that the $+584\,cm^{-1}$ band is composed of a stronger constituent due the vibronically allowed 3_0^1 transition together with a lesser contribution from the Franck-Condon allowed 2_0^3 progression member (Table 7.2).

The attribution of the $+781\,cm^{-1}$ band in Figure 7.1 as $3_0^1 2_0^1$ follows from the observed displacement of $\sim +200\,cm^{-1}$ relative to the 3_0^1 vibronically induced progression origin. Assignment of the $+1211\,cm^{-1}$ band as 3_0^2 is based on the anticipated Franck-Condon intensity for this transition.

Finally, we consider the band at $-218\,cm^{-1}$ (towards lower energy) from the $\tilde{C}\ ^2B_2 \leftarrow \tilde{X}\ ^2A_1$ origin. A candidate for its assignment might be the 3_1^1 sequence band. However, based on the estimate, $\nu_3'=580\,cm^{-1}$ from the measured position of the 3_0^1 transition, this assignment would imply that $\nu_3''=580+218=798\,cm^{-1}$. This appears to be too high given the values for ν_3'' derived from theory ($\sim$400-

450 cm^{-1}).[10] An alternative assignment is the hot band $3^0_1 2^1_0$, which would yield ν_3''=207+218=425 cm^{-1}.

7.5.2 $\tilde{D}\ ^2\mathbf{B}_1 \leftarrow \tilde{X}\ ^2\mathbf{A}_1$

The two strongest UV bands found in the $\tilde{D}\ ^2\mathrm{B}_1 \leftarrow \tilde{X}\ ^2\mathrm{A}_1$ band system (Figure 7.6, bands at 26 073 and +543 cm^{-1}) were investigated further at higher resolution (0.15 cm^{-1}) with R2C2PI and are shown in Figure 7.7. The bands could also be recorded using LIF but due to other overlapping features in this UV region the spectra are congested and more complicated to analyze.

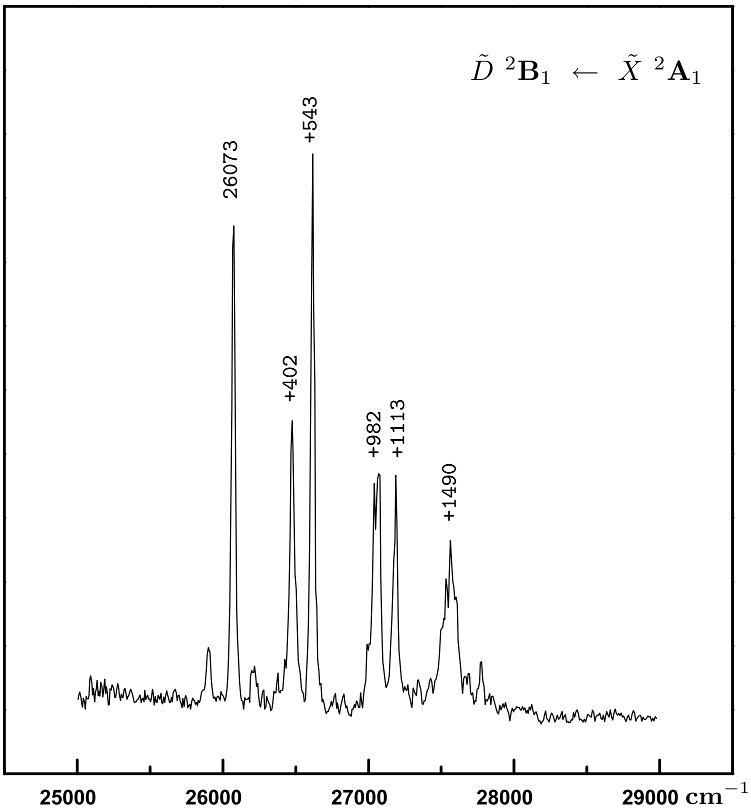

Figure 7.6: Low resolution resonant two-color, two-photon ionization spectrum of the $\tilde{D}\ ^2\mathrm{B}_1 \leftarrow \tilde{X}\ ^2\mathrm{A}_1$ electronic system for the T - shaped $\mathrm{AlC_2}$ radical, recorded in the range 24 000–29 000 cm^{-1} in a supersonic molecular beam.

The rotational band profiles are matched successfully with a simulation assuming a conventional Hamiltonian for an asymmetric top considering a *c*-type perpendicular transition in a C_{2v} molecule (dipole allowed T_x transition moment). The simulation compares favorably with the experimental trace for the 26 073 cm^{-1} band. Despite poorer signal to noise for the 26 616 cm^{-1} band, the simulation is acceptable. Attempts to match the measured rotational profile for the 26 073 cm^{-1} band with either a *b*-type perpendicular or *a*-type parallel simulation proved unsuccessful. Accordingly, these are assigned as belonging to another electronic band system, presumably the T_x electric dipole allowed $\tilde{D}\ ^2B_1 \leftarrow \tilde{X}\ ^2A_1$ transition. Recent calculations (SA-CASSCF geometry optimization - Table 7.3),[33] estimate that the $\tilde{D}\ ^2B_1$ state energy is in vicinity of 3.1 eV (~25 000 cm^{-1}), lending further support to the assignment of the AlC_2 vibronic structure in the 24 000-28 000 cm^{-1} region as being due to the $\tilde{D}\ ^2B_1 \leftarrow \tilde{X}\ ^2A_1$ transition. Assignments for the vibrational structure observed are discussed below and presented in Table 7.2.

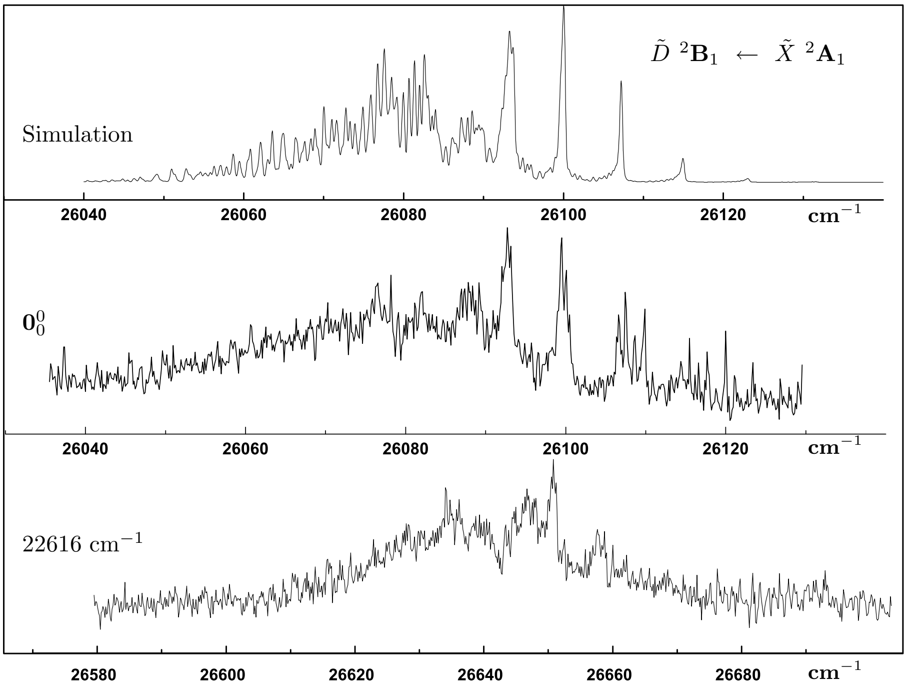

Figure 7.7: Rotationally resolved resonant two-color, two-photon ionization spectra (0.15 cm^{-1} bandwidth) of the two strongest bands observed in the $\tilde{D}\ ^2B_1 \leftarrow \tilde{X}\ ^2A_1$ system. A rotational contour simulation for a *c*-type $^2B_1 \leftarrow {}^2A_1$ transition is shown in the top trace.

The dominant progression forming mode in the $\tilde{D}\ ^2B_1 \leftarrow \tilde{X}\ ^2A_1$ transition appears to be ν_2, in contrast to the activity observed in ν_1 for the $\tilde{C} \leftarrow \tilde{X}$

excitation. The ν_2 vibrational mode is principally the Al$-$C$_2$ symmetric stretch. As may be deduced from the inertial parameters emerging from the *c*-type band contour simulation shown in Figure 7.7, the Al$-$C bond length, hence the Al$-$C$_2$ perpendicular distance, changes appreciably in the $\tilde{D}$ state relative to the ground state ($\tilde{D}$: 1.996 Å; $\tilde{X}$: 1.819 Å; Δ=0.165 Å), and considerably more than between the $\tilde{C}$ and $\tilde{X}$ states (Δ=0.016 Å).[10] This large geometric change along the ν_2 normal coordinate associated with $\tilde{D} \leftarrow \tilde{X}$ excitation confirms the assignment of ν_2 as the dominant progression forming mode in the $\tilde{D}\ ^2\mathrm{B}_1 \leftarrow \tilde{X}\ ^2\mathrm{A}_1$ transition. The displacements for the transitions 2^1_0 and 2^2_0 are +543 cm^{-1} and 1113 cm^{-1} respectively. It is clear that the interval (570 cm^{-1}) between ν_2', v=1 and v=2 suggests a significant positive anharmonicity.

Figure 7.6 shows a relatively strong transition at +402 cm^{-1} displacement from the origin. The assignment offered is the Franck-Condon allowed Δv=2 transition in ν_3, i.e. 3^2_0. No band is observed at twice this displacement from the $\tilde{D}\ ^2\mathrm{B}_1 \leftarrow \tilde{X}\ ^2\mathrm{A}_1$ origin, hence the +402 cm^{-1} band cannot be the first member of a progression in an a$_1$ mode (the only possibility would be ν_1, but in any case the observed frequency is far too low for ν_1 to be a valid candidate). The observed transition cannot be 3^1_0 because the vibronic symmetry for the 3^1 level, assuming that this is the $\tilde{D}\ ^2\mathrm{B}_1 \leftarrow \tilde{X}\ ^2\mathrm{A}_1$ transition, is $\mathrm{b}_2 \otimes \mathrm{B}_1 = \mathrm{A}_2$ and the A$_2$-A$_1$ transition moment is zero for a C$_{2\mathrm{v}}$ molecule.

Assignments follow for the bands at +982 cm^{-1} and 1113 cm^{-1} as $3^2_0 2^1_0$ and 2^2_0. However, it is necessary to address two questions regarding this, as well as the relatively large anharmonicity in the ν_2 progression. First, the 3^2_0 assigned band is quite strong for a ν_3', v=2 Franck-Condon allowed transition. Second, the positions for $3^2_0 2^1_0$ and 2^2_0 appear a little abnormal. The most likely cause of these anomalies is a Fermi resonance between ν_3', v=2 and ν_2', v=1. This would be a classic case of $3^2 \ldots 2^1$ coupling via cubic anharmonicity (the well known ground state stretch-bend coupling in CO$_2$ being the pedagogical example).[34] This explanation is supported by the appearance of the structure in the +982, 1113 cm^{-1} region, which is relatively broad and indicative of the expected Fermi triad arising from the coupling between $3^4 \ldots 3^2 2^1 \ldots 2^2$. Likewise, the broad structure in the +1490 cm^{-1} region would be due to the corresponding Fermi quartet. Modeling of these possible Fermi resonances is outside the scope of this paper. It is likely that the first progression member of the ν_1 mode, i.e. 1^1_0, may also lie amongst this structure.

7.5.3 Vibronic coupling

The estimates for the AlC_2 vibrational frequencies derived for both the $\tilde{C}$ and $\tilde{D}$ states are summarized in Table 7.4. In the $\tilde{C}$ state, ν_2 is reduced considerably from its ground state value (ν_2'=207 cm^{-1} versus ν_2''=533 cm^{-1}). The 2^1 level is of B_2 vibronic symmetry. The drop in frequency is consistent with the proposal that the $\tilde{E}$ ($^2B_2$) state, calculated ~7500 cm^{-1} above the $\tilde{C}$ state, perturbs levels of B_2 symmetry in the $\tilde{C}$ state.

	$\tilde{X}\ ^2A_1$		$\tilde{C}\ ^2B_2$	$\tilde{D}\ ^2B_1$
	ω	$\tilde{\nu}$	$\tilde{\nu}$	
ν_1	1735^a	–	$1398(5)^c$	$1490(5)^c$
ν_2	645^a	$533(5)^b$	$207(5)^c$	$543(5)^c$
ν_3	421^a	$425(5)^b$	$580(5)^c$	$201(5)^d$

Table 7.4: Experimentally determined vibrational frequencies (cm^{-1}) for the two electronic systems. [a]calculated,[10] [b]this work (based on the assigned hot bands), [c]this work, [d]by dividing double quanta excitations.

Vibronic coupling between states in two interacting manifolds does involve all vibrational levels of appropriate symmetry. However, the dominant interactions are between like states with Δv=±1 differences in vibrational quantum numbers.[35,36] Hence, the v=0 level of the $\tilde{C}$ state will interact with the ν_2,v=1 level in the higher $\tilde{E}$ ($^2B_2$) state. In contrast, the ν_2,v=1 level of the $\tilde{C}$ state will be coupled with both the ν_2,v=0 and v=2 levels of the $\tilde{E}$ ($^2B_2$) state.

From simple perturbation theory |energy shift| = $|H^2_{ij}/(E_j - E_i)|$, where H^2_{ij} is the vibronic coupling interaction matrix element and $\Delta E = E_j - E_i$ is the energy difference between the coupled states. Furthermore, the coupling matrix elements (for harmonic oscillator wavefunctions) are related by the relationship $\langle \mathrm{v}+1|H_{ij}|\mathrm{v}\rangle = \sqrt{\mathrm{v}}\langle 1|H_{ij}|0\rangle$. Accordingly, a simple coupling scheme is used to obtain estimates for the shifts in vibrational energy levels due to vibronic coupling. The coupling matrix elements in the range ~1 000-3 000 cm^{-1} are typical for coupling between electronically excited states.[35,36]

A modest vibronic coupling matrix element of $\sim$1050 cm^{-1} (with ΔE=7 500 cm^{-1} taken as energy gap between the $\tilde{C}$ and $\tilde{E}$ states) is sufficient to "push down" the ν_2,v=1 level in the $\tilde{C}$ state by $\sim$300 cm^{-1} relative to what might be an unperturbed frequency for $\nu_2^{'}$ of $\sim$500 cm^{-1} (based on $\nu_2^{''}$=533 cm^{-1}). This could explain the considerably reduced frequency for ν_2 observed for the $\tilde{C}$ state.

The estimates for $\nu_3^{''}$ and $\nu_3^{'}$ are 425 and 580 cm^{-1}. The question arises as to why ν_3 is *increased* in the $\tilde{C}$ state relative to the $\tilde{X}$ state. Observe that ν_3 is of symmetry species b$_2$, hence the vibronic symmetry of the 3^1 level is $b_2 \otimes B_2 = A_1$. As established above from rotational contour simulations, the 3^1_0 transition arises as a result of vibronic coupling. The A$_1$ electronic state (with significant oscillator strength) that is most likely to be responsible for the intensity borrowing is the *lower* lying $\tilde{A}\,^2$A$_1$ state, calculated as lying $\sim$12 000 cm^{-1} below the $\tilde{C}$ state. From calculations analogous to those discussed above for ν_2, a coupling matrix element of $\sim$900 cm^{-1} is sufficient to "push up" the 3^1 level by $\sim$160 cm^{-1} in the $\tilde{C}$ state relative to its (calculated) frequency of $\sim$420 cm^{-1} in the $\tilde{X}$.

Analogous arguments may be applied to rationalize the frequencies for ν_2 and ν_3 observed in the $\tilde{D}$ state. The 2^1 level is observed at +543 cm^{-1}. This in fact is little different from it's ground state frequency of 533 cm^{-1}. The vibronic symmetry of 2^1 in the $\tilde{D}$ state is B$_1$. Moreover, the nearest B$_1$ electronic state with which the $\tilde{D}$ state can couple is the *lower* $\tilde{B}\,^2$B$_1$ state, $\sim$6 700 cm^{-1} below. Thus one would anticipate that if anything, ν_2 might increase in frequency in the $\tilde{D}$ state. The observed frequency of 543 cm^{-1} is consistent with the proposal that it has been pushed up, relative to its unperturbed frequency, as a result of vibronic coupling with the *lower* lying $\tilde{B}\,^2$B$_1$ state.

The ν_3 vibronic frequency in the $\tilde{D}$ state, derived from the observation of the 3^2_0 band at +402 cm^{-1} is approximately 200 cm^{-1}. This contrasts with ν_3 in the $\tilde{X}$ state, derived from the spectrum of $\sim$425 cm^{-1}. The vibronic symmetry of 3^1 in the $\tilde{D}(^2B_1)$ state is A$_2$. The only A$_2$ state nearby in AlC$_2$ is $\tilde{G}(^2A_2)$ state, calculated $\sim$12 500 cm^{-1} *above* the $\tilde{D}$ state. A vibronic coupling matrix element of $\sim$1150-1200 cm^{-1} would be sufficient to depress the 3^1 level in the $\tilde{D}$ state by the requisite amount of $\sim$220-250 cm^{-1}.

While the above arguments are indicative rather than quantitative, they serve to rationalize the observed frequencies for ν_2 and ν_3 observed in the $\tilde{C}$ and $\tilde{D}$ electronic states of AlC$_2$.

7.6 Conclusion

Vibrational structure in the electric dipole allowed $\tilde{C}\ {}^2\mathrm{B}_2 \leftarrow \tilde{X}\ {}^2\mathrm{A}_1$ and $\tilde{D}\ {}^2\mathrm{B}_1 \leftarrow \tilde{X}\ {}^2\mathrm{A}_1$ transitions has been measured with both LIF and mass selective R2C2PI spectroscopy. Rotational contour measurements have been carried out at higher resolution for a selection of the stronger bands in both systems. Assignments are provided for the Franck-Condon activity involving ν_1, ν_2 in the $\tilde{C}\ {}^2\mathrm{B}_2 \leftarrow \tilde{X}\ {}^2\mathrm{A}_1$ transition, as well as vibronic activity in ν_3 due to coupling with the strong dipole allowed $\tilde{A}\ {}^2\mathrm{A}_1 \leftarrow \tilde{X}\ {}^2\mathrm{A}_1$ excitation. The strong Franck-Condon activity in the ν_1 mode (C=C stretch) is consistent with the observed $\tilde{C}\ {}^2\mathrm{B}_2 \leftarrow \tilde{X}\ {}^2\mathrm{A}_1$ geometry change, deduced from rotational band contour simulations, which involved appreciable lengthening of the C=C bond. In the higher lying $\tilde{D}\ {}^2\mathrm{B}_1 \leftarrow \tilde{X}\ {}^2\mathrm{A}_1$ transition, the Franck-Condon activity is dominated by an intense progression involving ν_2 (Al$-$C$_2$ stretch). This assignment is supported by an appreciable change in the Al-C bond length, and hence Al$-$C$_2$ perpendicular distance, estimated from rotational band contour simulation assuming an *c*-type perpendicular transition. The simulations confirm the attribution of the excitation as $\tilde{D}\ {}^2\mathrm{B}_1 \leftarrow \tilde{X}\ {}^2\mathrm{A}_1$. No vibronic activity in ν_3 is possible for this transition because of symmetry constrains. However, there is evidence of $3^2 \ldots 2^1$ coupling via cubic anharmonicity in the $\tilde{D}$ vibrational manifold. New estimates for vibrational frequencies and rotational parameters are thereby provided for the $\tilde{C}$ and $\tilde{D}$ states of AlC$_2$ (Table 7.4).

Bibliography

[1] M. Guélin, J. Cernicharo, C. Kahane, and J. Gomez-Gonzalez, Astron. Astrophys. **157**, L17 (1986).

[2] K. Kawaguchi, E. Kagi, T. Hirano, S. Takano, and S. Saito, Astrophys. J. **406**, L39 (1993).

[3] M. A. Anderson and L. M. Ziurys, Astrophys. J. **452**, L157 (1995).

[4] U. J. Sofia, J. A. Cardelli, and B. D. Savage, Astrophys. J. **430**, 650 (1994).

[5] F. X. Sunahori, J. Wei, and D. J. Clouthier, J. Am. Chem. Soc. **129**, 9600 (2007).

[6] N. Oliphant, A. Lee, P. F. Bernath, and C. R. Brazier, J. Chem. Phys. **92**, 2244 (1990).

[7] H. Abe, M. Mukai, M. Fujitake, and N. Ohashi, J. Mol. Spectrosc. **195**, 317 (1999).

[8] A. J. Schoeffler, H. Kohguchi, K. Hoshina, Y. Ohshima, and Y. Endo, J. Chem. Phys. **114**, 6142 (2001).

[9] Y. Sumiyoshi, T. Ueno, and Y. Endo, J. Chem. Phys. **119**, 1426 (2003).

[10] E. Chasovskikh, E. B. Jochnowitz, E. Kim, I. Navizet, and J. P. Maier, J. Phys. Chem. A **111**, 11986 (2007).

[11] D. L. Michalopoulus, M. E. Geusic, P. Langridgesmith, and R. E. Smalley, J. Chem. Phys. **80**, 3556 (1984).

[12] J. M. L. Martin, P. R. Taylor, J. T. Yustein, T. R. Burkholder, and L. Andrews, J. Chem. Phys. **99**, 12 (1993).

[13] M. Wyss, M. Grutter, and J. P. Maier, J. Phys. Chem. A **102**, 9106 (1998).

[14] T. C. Steimle et al., J. Chem. Phys. **106**, 2060 (1997).

[15] R. R. Bousquet and T. C. Steimle, J. Chem. Phys. **114**, 1306 (2001).

[16] T. C. Steimle, R. R. Bousquet, K. C. Namiki, and A. J. Merer, J. Mol. Spectrosc. **215**, 10 (2002).

[17] F. J. Kohl and C. A. Stearns, J. Chem. Phys. **52**, 6310 (1970).

[18] C. A. Stearns and F. J. Kohl, J. Phys. Chem. **77**, 136 (1973).

[19] E. E. Filby and L. L. Ames, Inorg. Nucl. Chem. Lett. **8**, 855 (1972).

[20] A. I. Boldyrev, J. Simons, X. Li, and L. S. Wang, J. Am. Chem. Soc. **121**, 10193 (1999).

[21] G. V. Chertihin, L. Andrews, and P. R. Taylor, J. Am. Chem. Soc. **116**, 3513 (1994).

[22] X. G. Zheng, Z. H. Wang, and A. C. Tang, J. Phys. Chem. A **103**, 9275 (1999).

[23] H. Ding et al., J. Chem. Phys. **119**, 814 (2003).

[24] W. C. Wiley and I. H. McLaren, Rev. Sci. Instrum. **26**, 1150 (1955).

[25] J. D. Watts, J. Gauss, and R. J. Bartlett, J. Chem. Phys. **98**, 8718 (1993).

[26] A. D. Becke, J. Chem. Phys. **98**, 5648 (1993).

[27] D. E. Woon and T. H. Dunning, J. Chem. Phys. **98**, 1358 (1993).

[28] H. J. Werner and P. J. Knowles, J. Chem. Phys. **82**, 5053 (1985).

[29] H. J. Werner and P. J. Knowles, J. Chem. Phys. **89**, 5803 (1988).

[30] M. J. Frisch et al., Gaussian98, Revision A.7, Gaussian Inc., Pittsburgh PA, 1998.

[31] H. J. Werner et al., MOLPRO, version 2006.1, a package of ab initio programs written by, http://www.molpro.net.

[32] D. Luckhaus and M. Quack, Mol. Phys. **68**, 745 (1989).

[33] R. Linguerri, private communication.

[34] G. Herzberg, *Molecular Spectra and Molecular Structure. II. Infrared and Raman Spectra of Polyatomic Molecules*, D. van Nostrand, New York, 1945.

[35] G. Fischer, *Vibronic Coupling - The Interaction between the Electronic and Nuclear Motions*, Academic Press, New York, 1984.

[36] W. D. Lawrance and A. E. W. Knight, J. Phys. Chem. **94**, 1249 (1990).

8 Electronic spectrum of titanium dioxide, TiO_2

8.1 Introduction

Among the more important of the numerous technological applications of titanium dioxide is its use as a photocatalyst to degrade organic pollutants or to perform other useful chemical transformations. Nanomeric and subnanomeric clusters of TiO_2 prepared on or incorporated in zeolites are particularly promising photocatalysts.[1,2] The photocatalytic role of TiO_2 could be greatly enhanced if a particular isomer that more effectively absorbs the solar radiation at the Earth's surface could be identified and synthesized. Studies of gas-phase clusters of TiO_2 provide a practical experimental and theoretical means of gaining a molecular level understanding of the properties that influence the activity of zeolite supported TiO_2 clusters and the isomeric dependence of absorption. Insight into the chemical activity of bulk TiO_2 may also be revealed from studies of clusters. Indeed, there is experimental evidence that the properties of small gas-phase clusters of TiO_2 emulate those of the bulk. For example, the observed band gap of molecular $(TiO_2)_n$ clusters approach that of bulk TiO_2 at $n = 6$ and remains relatively constant up to $n=10$, the largest species studied.[3] Furthermore, small clusters of mixtures of $(TiO_2)_n$ and $(Ti_2O_3)_m$ are observed to have an intense vibrational transition at 13.5 μm, which coincides with an intense band in the rutile spectrum, independently of their size and stoichiometry.[4] The monomer and small clusters of TiO_2 are also of interest in their own right being prototypes for *d*-orbital chemical bonding investigations.

Titanium is one of the most abundant refractory metals in space. It has been detected in the gas phase form as TiO and TiH towards cool M-type stars. The electronic transitions of the TiO molecule are so prominent in the M- and S-stars, that they are used for their spectral classification. Due to the refractory nature of this element, it is assumed that a large fraction of Ti will be absent from the gas phase, but the temperature at which depletion becomes significant is not known. It has been suggested that Ti may be removed from the gas phase at temperature as high as 1650 K because of the formation of $CaTiO_3$.[5] Observations of the electronic spectrum of TiO towards M-stars, however, indicate rotational temperatures as low as 600 K, possibly even lower.[6] Towards cooler regions of stellar atmospheres or in the circumstellar shells of oxygen-rich stars, TiO may be further oxidized to TiO_2,[7] a very stable molecule which may be then incorporated into grains along with other oxides such as MgO, SiO_2, CaO, or FeO, to form complex minerals.

Given this diverse interest, there has been an intense effort to measure and predict the properties of the monomer and small clusters of TiO_2. The properties of the monomer are more readily derived from experimental studies than the properties of clusters. Accordingly, a comparison of theoretically and experimentally derived properties for the monomer is the primary means of assessing methodologies being implemented for predicting the properties of clusters of TiO_2. The numerous reported theoretical studies for the TiO_2 monomer[8–19] are, in a large part, due to its use as a benchmark for this purpose. A review of the theoretical investigations can be found in Ref. 19. The theoretical predictions for this prototypical metal dioxide should be highly quantitative because of the limited number of valence electrons (eight) and the small relativistic effects owing to the low atomic number. A goal of the present study is to experimentally determine the vibrational frequencies and geometric structure for the low-lying excited states of molecular TiO_2 using optical spectroscopy.

The majority of spectroscopic studies of TiO_2 involve matrix-isolated samples. The infrared absorption and visible emission spectra of neon matrix isolated TiO_2 were analyzed in early 70s.[20] The spectrum was consistent with a C_{2v} structures in both the ground and excited electronic state. The ν_1 (a_1) symmetric stretching frequency, ω_1, the ν_3 (b_2) asymmetric stretching frequency, ω_3, for the $^{48}TiO_2$ isotopologue were determined to be $962.0\pm2\,\mathrm{cm}^{-1}$ and $934.8\pm2\,\mathrm{cm}^{-1}$, respectively. The isotopic dependence of ω_3 was used to extract an estimate for the bond angle, Θ, of $110\pm15°$. Weak, visible emission having an origin at 5295.02 ± 2Å and exhibiting a progression in the ν_3 (b_2) asymmetric stretch of the $\tilde{X}\ ^1A_1$ state was observed. It was rationalized that the observed long vibrational progression implied a significant change in geometry upon excitation. The infrared absorption spectrum in an argon matrix was recorded and analyzed to give ν_1 and ν_3 of 946.9 cm^{-1} and 917.1 cm^{-1}, respectively.[10] Again the isotopic dependence of ν_3 was used to estimate Θ to be 113±5°. The results were supported by Hartree-Fock level *ab initio* calculations. The infrared and electronic spectrum in a neon matrix of isolated TiO_2 was recently recorded in our group.[21] A mass selected deposition technique using TiO_2^- anions was employed and neutral TiO_2 was generated by photo-detachment. Progressions in two band systems in the visible range were assigned. The origin of one band, having a vibrational progression with spacing of 840 cm^{-1}, was at 628 nm. It was suggested that this band was due to an electronic transition for the linear isomer. The second band system exhibited two vibrational progressions, one with a spacing of 850 cm^{-1}, and another of 180 cm^{-1}. The origin of this band was difficult to assign because of overlapped TiO features, but was estimated to be 524 nm and assigned as the $\tilde{A}\ ^1B_2 \leftarrow \tilde{X}\ ^1A_1$ transition of the bent oxo (O=Ti=O) form. A third, weak, band system with an origin at 368 nm was assigned as the $\tilde{C}\ ^1B_1 \leftarrow \tilde{X}\ ^1A_1$ transition of the same isomer.

Gas phase spectroscopic studies of TiO_2 are few in number. Forty years ago, the Harvard group[22] performed an electrostatic deflection measurement on a molecular beam sample of TiO_2 demonstrating that the ground state had a permanent electric dipole, thus ruling out a linear O=Ti=O structure. The electronic structure of TiO_2, and small clusters thereof, were investigated by photoelectron spectroscopy (PES).[23] The symmetric stretching frequency, ω_1 (a_1), of the $\tilde{X}\ ^1A_1$ state was measured to be 940±40 cm^{-1}, consistent with the matrix isolation value. Spectral features at 1.96 eV and 2.4 eV above that of the $\tilde{X}\ ^1A_1$ were assigned to the $\tilde{a}\ ^3B_2$ and $\tilde{A}\ ^1B_2$ excited states, with the latter being consistent with the matrix isolation value. Recently, the pure rotational transitions in the (0,0,0) $\tilde{X}\ ^1A_1$ vibronic state were recorded and analyzed to produce the first experimental structure.[24] The determined effective bond length, R_{Ti-O}, and bond angle, Θ, were 1.651Å, =111.6°, respectively. A laser ablation/supersonic expansion scheme was used for the generation of molecular TiO_2 in both the pure rotational and PES studies.

The theoretical predictions and experimental data suggest that the optical spectrum of TiO_2 will be complex. The lowest $\tilde{a}^3B_2$ triplet and $\tilde{A}^1B_2$ singlet states are predicted[17] to assume a bent oxo (O=Ti=O) form like the $\tilde{X}^1A_1$ state, but with a much smaller bond angle (≈95°). Hence the $\tilde{A}\ ^1B_2 \leftarrow \tilde{X}\ ^1A_1$ electronic transition will have long vibronic progressions and a very open branch structure. Strong vibronic coupling is also expected because the C_{2v} structures $\tilde{a}^3B_2$ triplet and $\tilde{A}^1B_2$ states are only approximately 0.3 eV more stable than the linear form.[17]

8.2 Experimental

Mass selected resonance enhanced multiphoton ionization (REMPI) measurements were carried out to obtain the low resolution and partially rotationally resolved vibronic bands in the TiO_2 electronic spectrum. The experimental setup is presented in the Experimental section of this thesis. TiO_2 was produced by laser ablation of a pure titanium rod in the presence of approximately 2% O_2 in helium. The supersonic expansion products were skimmed to produce a well collimated molecular beam. Low-resolution ($\sim 5\,\mathrm{cm}^{-1}$ bandwidth) mass selected REMPI spectra were recorded using an OPO system (excitation laser) and an F_2 excimer laser (λ=157 nm or 7.9 eV) as the ionization source. Higher-resolution ($\sim 0.15\,\mathrm{cm}^{-1}$ bandwidth) spectra were recorded using a broad-band tunable dye laser with an output of 2 mJ/pulse (pumped by a XeCl (λ=308 nm) excimer laser).

8.3 Results and discussion

The F_2 excimer laser multi-photoionization time-of-flight mass spectrum of the products produced by the ablation of titanium in the presence of a He/O_2 supersonic expansion is presented as the red trace in Figure 8.1. In addition to the monomer TiO_2, signals from the dimers $(TiO_2)_2$, and $(TiO)_2$, the O_2 complexes $TiO(O_2)$ and $TiO_2(O_2)$, and Ti_2O_3 are detected. The stick diagram is the calculated mass spectrum based on the isotopic ratios of Ti atom. The mass spectrum is dominated by the Ti atomic signal and TiO (not displayed in the spectrum), both having and ionization potential lower then 7.9 eV. The TiO_2 mass signal was recorded only on resonance. It is to be noted that the adiabatic and vertical ionization potential of TiO_2 have been determined to be 9.5 and 9.62 eV, respectively.

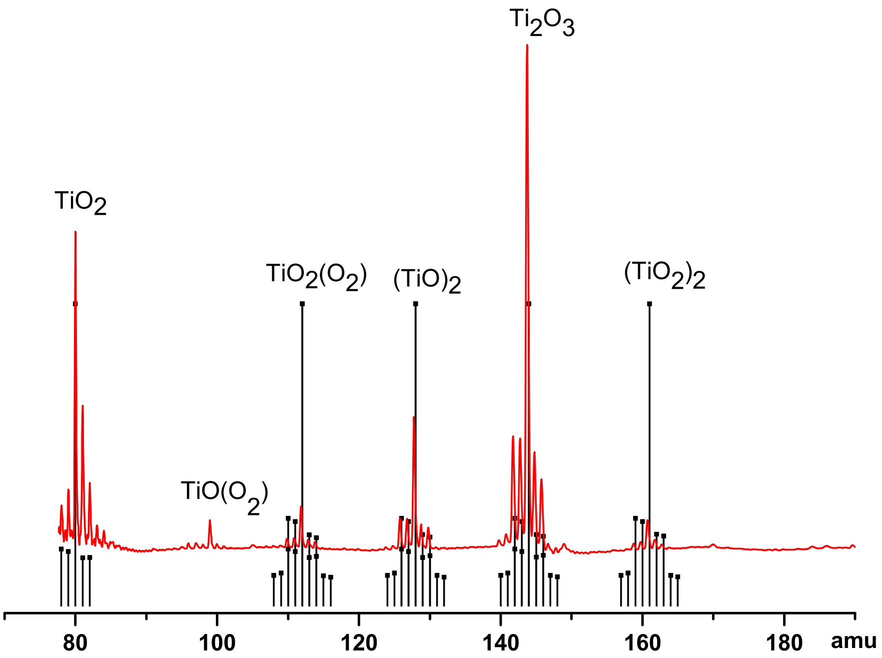

Figure 8.1: The multiphoton ionization time-of-flight mass spectrum of the product of the ablated titanium in a He/O_2 supersonic expansion.

The low resolution, mass selected, REMPI spectrum in the range of a $17000\,\mathrm{cm}^{-1}$ to $21500\ \mathrm{cm}^{-1}$ is presented in Figure 8.2. The simulated spectrum is displayed below the experimental one. Based on the theoretical studies which predict a big geometry change from ground to excited state, the experimental spectrum would be dominated by a long vibronic progression and a very open branch structure. The TiO_2 molecule, as other triatomic species of C_{2v} symmetry, is characterized by three vibrational frequencies, ν_1, ν_2 of a_1 symmetry, and the asymmetric mode ν_3 (b_2). The $\tilde{X}^1A_1$ ground state of TiO_2 has been well characterized, the ν_1 and ν_3 vibronic frequencies have been measured using matrix isolation spectroscopy.[10] Recently, the ν_2 has been determined through dispersed fluorescence technique.[25] Unfortunately, little is known about the excited state

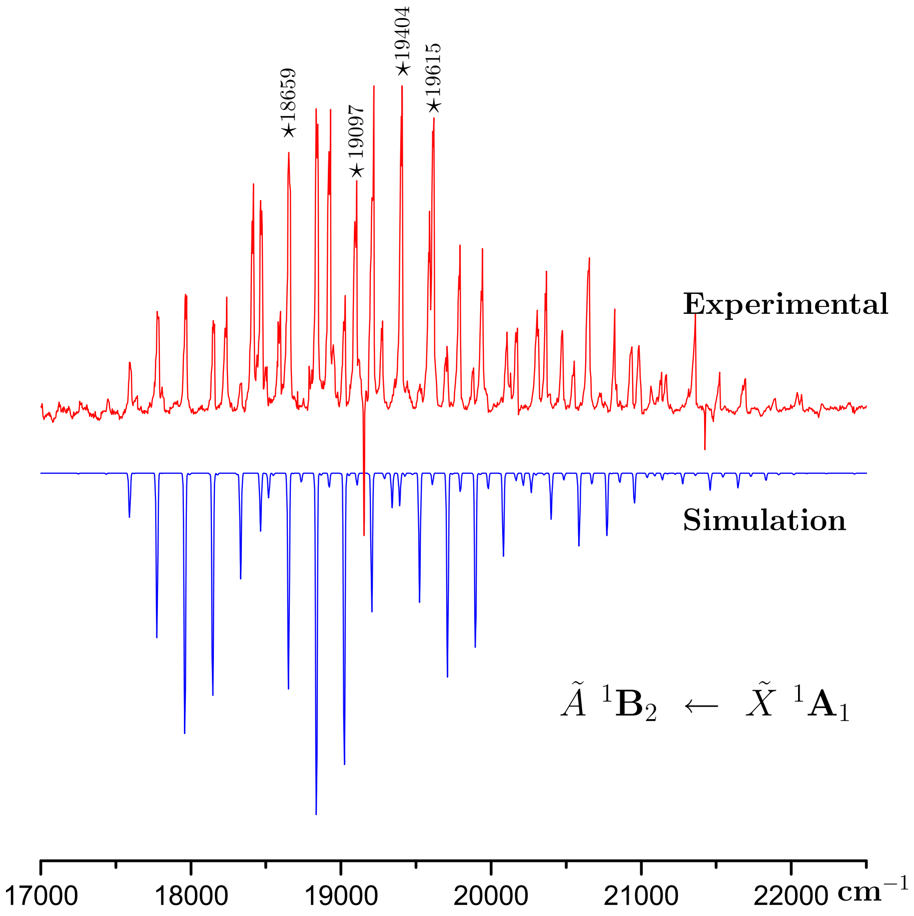

Figure 8.2: Low resolution REMPI electronic spectrum of the $\tilde{A}\ ^1B_2 \leftarrow \tilde{X}\ ^1A_1$ electronic transition of titanium dioxide. Below the experimental spectrum the vibrational simulation is presented.

geometry and vibrational frequencies, except the theoretical calculations which predict ν_1=875 cm^{-1}, ν_2 drops to approximately half of its ground state value, 196 cm^{-1} and the same behavior for the ν_3 which drops to 480 cm^{-1}.[17] These differences are associated with the big geometry change in the excited state.

The preliminary analysis of the experimental spectrum shows a long progression in the symmetric stretching (ν_1) and bending (ν_2) vibrational modes, and combinations of the two. In the simulated vibrational spectrum, the predicted values for the excited state have been used and a vibrational temperature of 100 K has been assumed. The spectrum fits well in the low frequency region but not very well at high frequencies. The discrepancies between experimental and simulated spectrum may arise from the fact that vibronic coupling of ν_3 with a low or high lying electronic state has not been introduced in the simulation. It should be noted that the calculations predicted the $\tilde{a}^3B_2$ triplet state to lie only 0.05 eV higher in energy than the singlet state. In order to check the presence of another state in the same frequency region, excited state lifetime measurements have been performed by varying the delay between the excitation and ionization laser. No significant differences between the lifetimes of the vibronic bands has been observed, indicating that the observed bands should belong to one state. The triplet state, based on the electronic selection rules would be spin forbidden, if allowed would be a long lived state.

The dispersed fluorescence measurements were performed by exciting the $5_{14} \leftarrow 4_{13}$ rotational line of the 18659.2 cm^{-1} band in the $\tilde{A}\ ^1B_2 \leftarrow \tilde{X}\ ^1A_1$ electronic spectrum and dispersing the fluorescence with the use of a monochromator.[25] The results indicate no features to the blue of the excitation wavelength confirming that the excited band is not a hot band. Based on the parallel profile of the observed band it was concluded that the excited band originates from a totally symmetric mode (either ν_1 or ν_2). The lack of more dispersed fluorescence measurements of other vibronic bands to the red of 18659.2 cm^{-1} band make the identification of the origin band difficult at this point.

The isotopic shifts of the vibronic bands should help in assignment of the origin band. It has been estimated the Ti isotopic shifts for ν_1 mode are between 1.8-2.1 cm^{-1}, smaller than for ν_3, 2.8-3.1 cm^{-1} which has less oxygen character in the vibrational motion. Due to the fact that the laser employed in the low-resolution scans has a bandwidth of ~5 cm^{-1}, such shifts can not observed, ruling out the possibility of assigning the origin band.

The vibronic bands marked with stars in the low resolution spectrum have been partially rotationally resolved. In Figure 8.3 the high resolution spectrum of the 19615 cm^{-1} vibronic band, one of the strong band in the low resolution spectrum, is presented. The experimental spectrum is accompanied by a spectral simulation. A rotational analysis using the PGOPHER program[26] was performed with a conventional Hamiltonian for an asymmetric top assuming an *a*-type transition in a C_{2v} molecule. Two other bands are presented in Figure 8.4 and 8.5 together with a spectral simulation of an a-type transition.

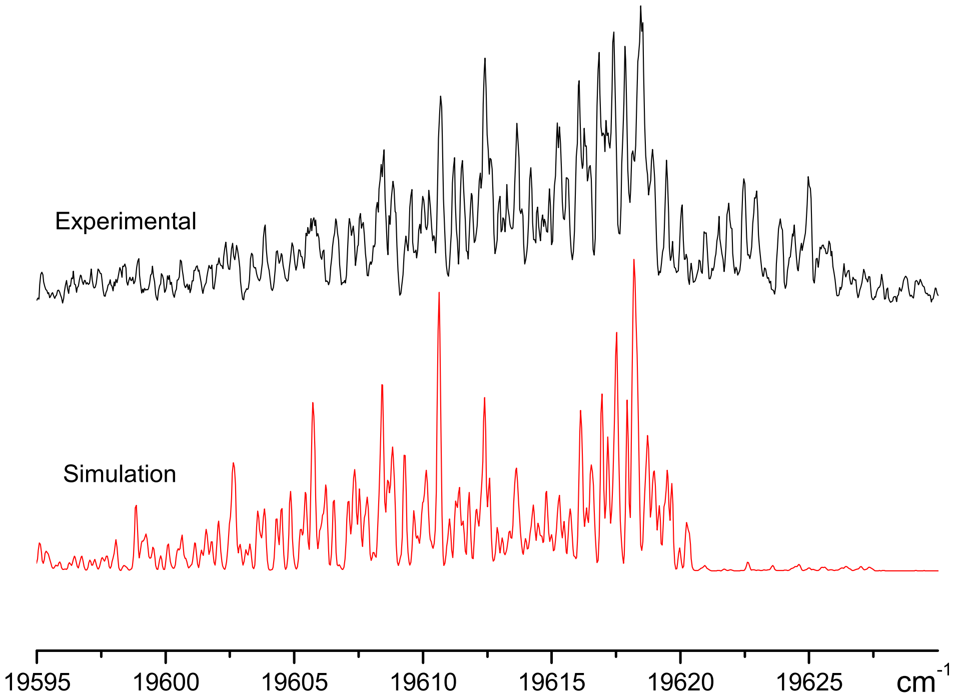

Figure 8.3: High resolution REMPI electronic spectrum of the 19615 cm^{-1} band in the $\tilde{A}\ ^1B_2 \leftarrow \tilde{X}\ ^1A_1$ electronic transition of titanium dioxide. Below the experimental spectrum the rotational simulation obtained by varying the following parameters ν_0, A',B',C',D$_J$',D$_{JK}$', D$_K$', Δ_J', Δ_K' is presented.

Based on the symmetry selection rules, only the bands due to the excitation of a totally symmetric mode would have such a profile. The rotational constants and the centrifugal distortion parameters for the ground state are well determined through the means of microwave spectroscopy and were kept constant during the simulation. A good agreement between the experiment and simulation was achieved by varying the excited state rotational constant, centrifugal distortion parameters and for a temperature of 45 K. Based on the selection rules for an a-type parallel transition rotational lines with ΔK_a=0 and ΔK_c=±1 would be present in the experimental spectrum. Due to the nuclear spin statistics only half of the levels are present. Specifically, only those levels that have electronic-

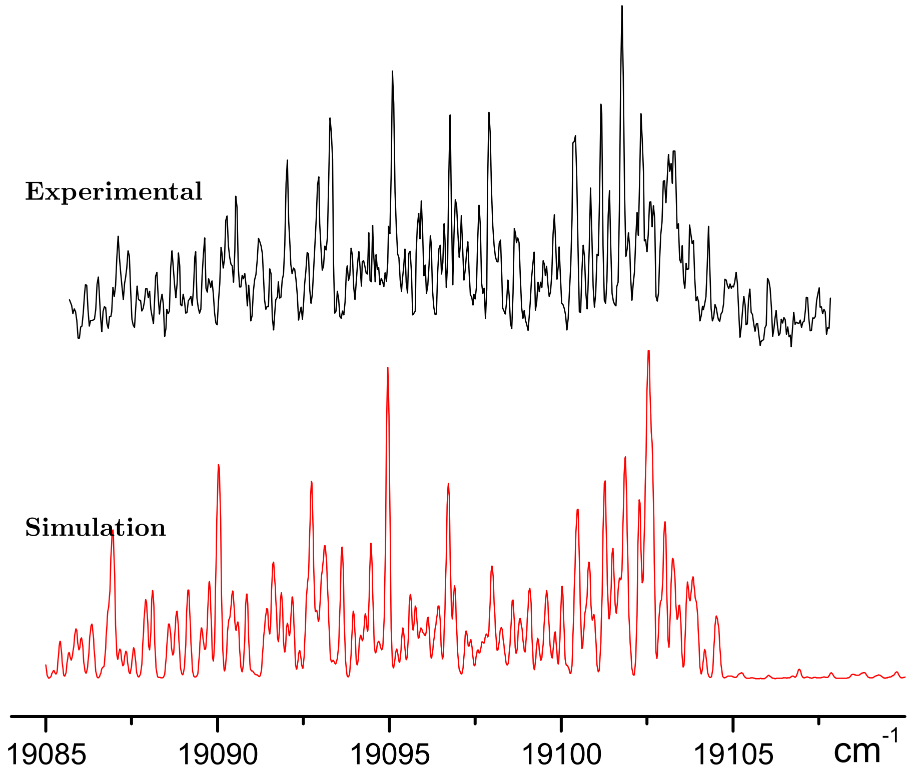

Figure 8.4: High resolution REMPI electronic spectrum of the 19097 cm^{-1} band in the $\tilde{A}\ ^1B_2 \leftarrow \tilde{X}\ ^1A_1$ electronic transition of titanium dioxide.

vibrational-rotational species A_1 and A_2 in C_{2v} symmetry are allowed due to the equivalent $^{16}O(I=0)$.[27]

The rotational spectrum is in qualitative agreement with the expectations that the P, Q, and R branches will have an open structure because of the predicted large change in geometry upon excitation. Due to the modest resolution of the excitation laser individual rotational lines under the P, Q and R branches could not be resolved. However, few R and Q-lines could be identified in the rotational spectrum. The reason for the imperfect fit may arise from the fact that the $\tilde{A}^1B_2$ rovibronic levels are perturbed as a result of rovibronic coupling with higher lying electronic states. The molecular constants obtained are given in Table 8.1 together with the calculated values. Geometric structures can be estimated from the rotational constants derived in the spectroscopic fit, with the Ti-O bond length of 1.711Å and the O=Ti=O angle of 102.5°.

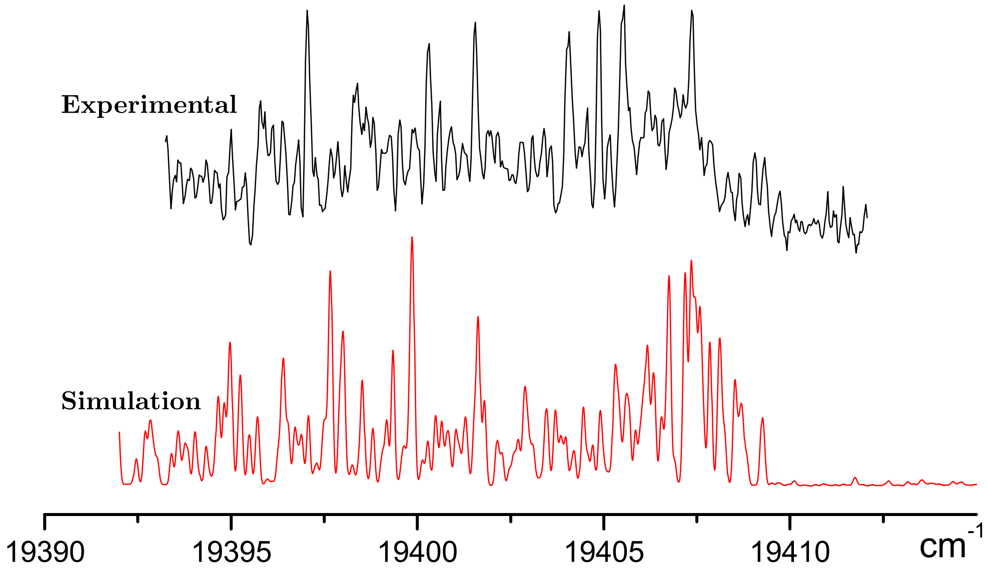

Figure 8.5: High resolution REMPI electronic spectrum of the 19404 cm^{-1} band in the $\tilde{A}\ ^1B_2 \leftarrow \tilde{X}\ ^1A_1$ electronic transition of titanium dioxide.

Another vibronic band marked with star, located at 18659 cm^{-1}, was partially rotationally resolved using the REMPI technique. Based on the REMPI modest resolution spectrum, a high resolution spectrum (0.001 cm^{-1}) was measured using the laser induced fluorescence (LIF) technique.[25] Very precise molecular parameters have been obtained and the TiO_2 excited state geometry has been inferred. The bond length and O=Ti=O angle values are in a good agreement with the ones obtained by fitting the REMPI spectrum of the 19615 cm^{-1} band.

8.4 Conclusions

The gas-phase electronic spectrum of titanium dioxide has been recorded for the first time. The spectrum reveals a very complicated structure with no clear origin band making the assignment of the vibronic bands difficult. The preliminary analysis of the vibrational spectrum indicates progressions in the ν_1 and ν_2 modes and combination of the two. The simulation does not fit well in the higher frequency region of the spectrum. The $\tilde{a}\ ^3B_2$ triplet state is predicted to lie only 0.05 eV higher in energy than the singlet state which may complicate the spectrum. Another reason for an imperfect fit is that the vibronic coupling of the ν_3

	A	B	C	r_{Ti-O}	∠ OTiO	Electronic configuration
$\tilde{X}^1A_1$	1.0180	0.2826	0.2260	1.651^a	111.5^a	$1a_2^2 3b_1^2 9a_1^2 6b_2^2$
				1.651^b	110.7^b	
$\tilde{A}^1B_2$	0.7653	0.2957	0.2166	1.711^c	102.5^c	$1a_2^2 3b_1^2 9a_1^2 6b_2^1 10a_1^1$
				1.703^b	96.3^b	

Table 8.1: Molecular parameters for the 19615 cm^{-1} band obtained through a spectral fit of the high resolution spectrum. [a]Reference 23. [b]Reference 17. [c]This work.

mode (asymmetric mode) with higher lying electronic states could not be introduced in the simulation. Dispersed fluorescence measurement of the bands to the red of 18659 cm^{-1} band would help in assigning the origin band. The rotational profile of the rotational resolved bands indicate an *a*-type parallel profile leading to the conclusion that the observed bands are due to the excitation of totally symmetric modes. The obtained rotational parameters agree well with the constants obtained from the spectral fit of the 18659 cm^{-1} band rotationally resolved with a resolution of 0.001 cm^{-1}. The vibrational analysis awaits for more dispersed fluorescence measurements and elaborated excited state theoretical calculations.

Bibliography

[1] M. Kitano, M. Matsuoka, M. Ueshima, and M. Anpo, Appl. Catal. A. Gen. **325**, 1 (2007).

[2] C. Aprile, A. Corma, and H. Garcia, Phys. Chem. Chem. Phys. **10**, 769 (2008).

[3] H. J. Zhai and L. S. Wang, J. Am. Chem. Soc. **129**, 3022 (2007).

[4] K. Demyk, D. van Heijnsbergen, G. von Helden, and G. Meijer, Astron. Astrophys. **420**, 547 (2004).

[5] B. E. Turner, Astrophys. J. **376**, 573 (1991).

[6] P. J. G. and S. P. Davis, PASP **99**, 839 (1987).

[7] K. S. Jeong, J. M. Winters, I. Le Bertre, and E. Sedlmayr, Astron. Astrophys. **407**, 191 (2003).

[8] M. V. Ramana and D. H. Phillips, J. Chem. Phys. **88**, 2637 (1988).

[9] A. Hagfeldt, R. Bergstrom, H. O. G. Siegbahn, and S. Lunell, J. Phys. Chem. **97**, 12725 (1993).

[10] G. V. Chertihin and L. Andrews, J. Phys. Chem. **99**, 6356 (1995).

[11] M. B. Walsh, R. A. King, and H. F. Schaefer, J. Chem. Phys. **110**, 5224 (1999).

[12] K. S. Jeong, C. Chang, E. Sedlmayr, and D. Sulzle, J. Phys. B: At. Mol. Opt. Phys. **33**, 3417 (2000).

[13] T. Albaret, F. Finocchi, and C. Noguera, J. Chem. Phys. **113**, 2238 (2000).

[14] G. Gutsev, B. Rao, and P. Jena, J. Phys. Chem. A **104**, 5374 (2000).

[15] K. H. Kim, Y. S. Lee, J. H. Moon, Y. Kim, and G. H. Jeung, J. Chem. Phys. **117**, 8385 (2002).

[16] Z. W. Qu and G. J. Kroes, J. Phys. Chem. B **110**, 23306 (2006).

[17] F. Grein, J. Chem. Phys. **126**, 034313 (2007).

[18] E. L. Uzunova, H. Mikosch, and G. S. Nikolov, J. Chem. Phys. **128**, 094307 (2008).

[19] S. Li and D. A. Dixon, J. Phys. Chem. A **112**, 6646 (2008).

[20] N. S. McIntyre, K. R. Thompson, and J. Weltner, W., J. Phys. Chem. **75**, 3243 (1971).

[21] I. Garkusha, A. Nagy, Z. Guennoun, and J. P. Maier, Chem. Phys. **353**, 115 (2008).

[22] M. Kaufman, J. Muenter, and W. Klemperer, J. Chem. Phys. **47**, 3365 (1967).

[23] H. B. Wu and L. S. Wang, J. Chem. Phys. **107**, 8221 (1997).

[24] S. Bruenken, H. S. P. Mueller, K. M. Menten, M. C. McCarthy, and P. Thaddeus, Astrophys. J. **676**, 1367 (2008).

[25] H. Wang, T. C. Steimle, C. Apetrei, and J. P. Maier, Phys. Chem. Chem. Phys. **11**, 2649 (2009).

[26] C. M. Western, *PGOPHER a Program for Simulating Rotational Structure*, University of Bristol, http://pgopher.chm.bris.ac.uk, 2007.

[27] G. Herzberg, *Molecular Spectra and Molecular Structure. III. Electronic Spectra and Electronic Structure of Polyatomic Molecules*, D. van Nostrand, New York, 1966.

9 Concluding remarks

This thesis describes the experimental measurements and spectral analysis of large polyacetylenic chains and metal-capped carbon chains. The experimental method employed is a resonance enhanced multiphoton ionization technique (REMPI). The transient species were produced in a discharge or laser vaporization source. The main advantage of the REMPI technique is its mass selectivity making the assignment of the spectral carriers unambiguous.

The $^1\Sigma_u^+ \leftarrow X^1\Sigma_g^+$ electronic transitions of the $HC_{2n}H$ (n=5-7) chains have been measured for the first time in the gas phase. The origin band shifts to the red with the increase in the chain size. The spectrum is dominated by a progression in the acetylenic stretching mode. It is the only progression and therefore the only signature of a change in geometry for all these chains. The ground state is characterized by a bond alternation between the single and triple bonds. Bond lengths in the excited state have not been calculated. The trend can however be derived from the vibrational pattern of the electronic spectra. Because the $C \equiv C$ bond length increases in the excited state, the single bonds must be shorter. Thus bond alternation in the excited state is less pronounced and the π^* orbital is more delocalized. The individual vibronic bands can not be rotationally resolved due to the lifetime broadening. Internal conversion is responsible for the subpicosecond lifetime of the $^1\Sigma_u^+$ excited state.

In order to understand the effect of a metal atom attached to the carbon chains, an appropriate system to study is the metal-capped acetylene. In this direction, the electronic spectrum of the AlCCH molecule has been measured in the gas phase for the first time. The complicated vibronic structure is due to the Renner-Teller effect involving two vibrational modes. The origin band has been rotationally resolved and the linear structure of the molecule has been confirmed. The $\mathrm{Al}-\mathrm{C}$ bond length decreases in the excited state leading to the conclusion that the electronic transition is dominated by the promotion of a σ-electron localized on the Al atom to a π orbital with bonding character.

For studying the chain size effect on these metal-capped chains, the increase in the number of carbon atoms is important. Therefore, the properties of longer metal-capped chains have been studied by measuring the electronic spectra of the MgC_2H, MgC_4H and MgC_6H molecules. It has been observed that the oscillator strength of the allowed electronic transitions decreases with the increase in the chain size while the dipole moment increases. Therefore, the longer the chain the more difficult it is to record their electronic spectrum and the easier to measure their microwave spectrum. In comparison to the bare carbon chains, the nature of the electronic transition in the metal-capped chains is different. The latter involves excitation of an electron localized on the metal atom in contrast to the carbon chains where the delocalized π-electron is excited.

When the shortest metal-capped chain looses the other hydrogen atom the deviation from the linear structure of the molecule is observed. Thus, the T-shaped structure of the AlC_2 molecule has been confirmed by measuring its electronic spectrum in the gas phase. Two electronic systems have been recorded and analyzed. Changes in the excited state geometries relative to the ground state have been noticed and the molecular parameters for both ground and excited states have been determined. It is to be noted that the electronic transition shifts to the visible region of the electromagnetic spectrum with the loss of the hydrogen atom.

Another molecule of interest, based on its astrophysical relevance and also technological applications is titanium dioxide, TiO_2. The most adequate way to investigate the structure of such a molecule is to measure its electronic spectrum in the gas-phase, free of any interactions with the surrounding host lattice. The electronic spectrum of titanium dioxide has been measured for the first time in the gas phase and reveals a complicated vibronic pattern. The preliminary analysis indicates that few vibronic bands can be assigned to the excitation of totally symmetric modes (ν_1 and ν_2). From the rotational analysis of two vibronic bands the excited state geometry could be inferred, indicating a lengthening of the Ti-O bond and a decrease in the O=Ti=O angle. A complete analysis of the vibronic spectrum awaits dispersed fluorescence measurements of more of the vibronic bands in the lower frequency region of the spectrum and elaborated calculations to take into account perturbations due to other electronic states.

The purpose of measuring the electronic spectra of these species is not only the fundamental understanding of their electronic properties but also their astrophysical relevance. The carbon chains have been proposed for a long time as carriers of the diffuse interstellar bands and have also been detected in different environments such as circumstellar shells of the carbon-rich stars. Metals and metal-containing species have been observed in the same environments based on their sub-millimeter/millimeter spectrum. As the species mentioned in this thesis have been measured for the first time in the gas phase, the molecular parameters deduced here provide the basis for the search of their millimeter spectra in the laboratory leading to searches for their detection in space.

A Appendix 1

A.1 Further spectral simulation with higher resolution for AlCCH

Given the fact that dye laser employed in the measurement of the origin band of the $A\ ^1\Pi \leftarrow X\ ^1\Sigma^+$ transition has a modest resolution of $0.15\,\mathrm{cm}^{-1}$ the rotational structure has been partially resolved. As shown in Figure 5.5 of the chapter 2 individual overlapping lines of P and Q branches can not be distinguished easily at this modest resolution due to the high density of lines.

In order to resolve the rotational structure of the origin band two simulations have been carried out considering the laser resolution available in the laboratory. First, of $0.05\,\mathrm{cm}^{-1}$ that would be achievable with a dye laser equipped with an intra-cavity étalon. Taken into consideration that the origin band of the AlCCH lies in the UV region of the electromagnetic spectrum the adjustment of an intra-cavity étalon it is very difficult. The simulation with such a resolution is showed in the Figure A.1. With this resolution the P and Q branches are better resolved and more accurate rotational parameters can be obtained.

To obtain narrow-band radiation for high resolution spectroscopy a pulsed-amplification system has been developed in the laboratory to be coupled with the pulsed cavity ring-down spectrometer. The Doppler-free line-width that can be achieved with this system is $0.001\,\mathrm{cm}^{-1}$. The Doppler broadening for AlCCH has been estimated using the following equation:

$$\Delta\tilde{\nu}_{\mathrm{D}} = 7.2 \times 10^{-7} \cdot \tilde{\nu}_0 \cdot \sqrt{\frac{T}{M}} \tag{A.1}$$

in which T is in K, M in atomic mass units u, $\tilde{\nu}_0$ in cm^{-1}, and $\Delta\tilde{\nu}_{\mathrm{D}}$ in cm^{-1}. An R-line at $28\,764.1526\,\mathrm{cm}^{-1}$was taken as $\tilde{\nu}_0$ and temperature T of 30 K. The

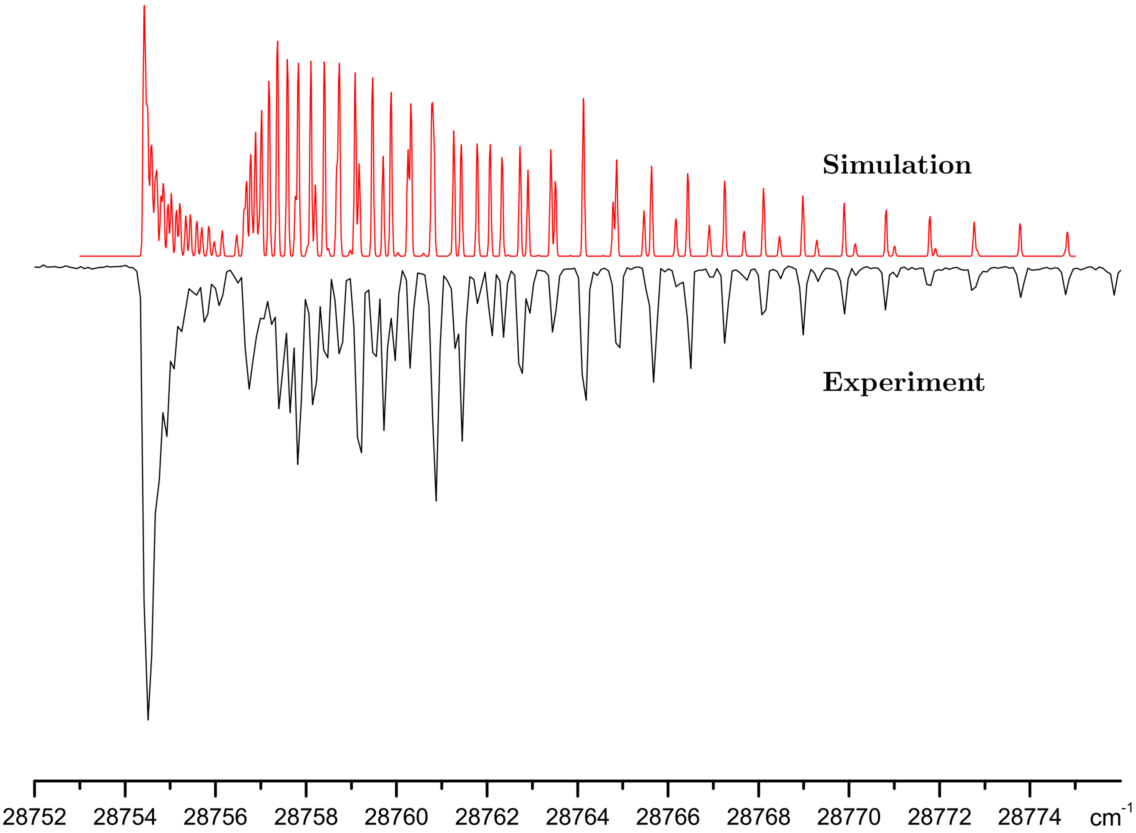

Figure A.1: Simulation with $0.05\,\mathrm{cm}^{-1}$ resolution of the origin band of the $A\ ^1\Pi \leftarrow X\ ^1\Sigma^+$ electronic transition for AlCCH.

Doppler broadening of $0.0157\,\mathrm{cm}^{-1}$was obtained, thus the maximum resolution achievable. A simulation at this spectral resolution is displayed in the Figure A.2.

Due to the fact that P and Q branches are better resolved, higher order terms, such as centrifugal distortion and Λ-doubling constant, q, can be included in the model and more precise rotational constants would be obtained.

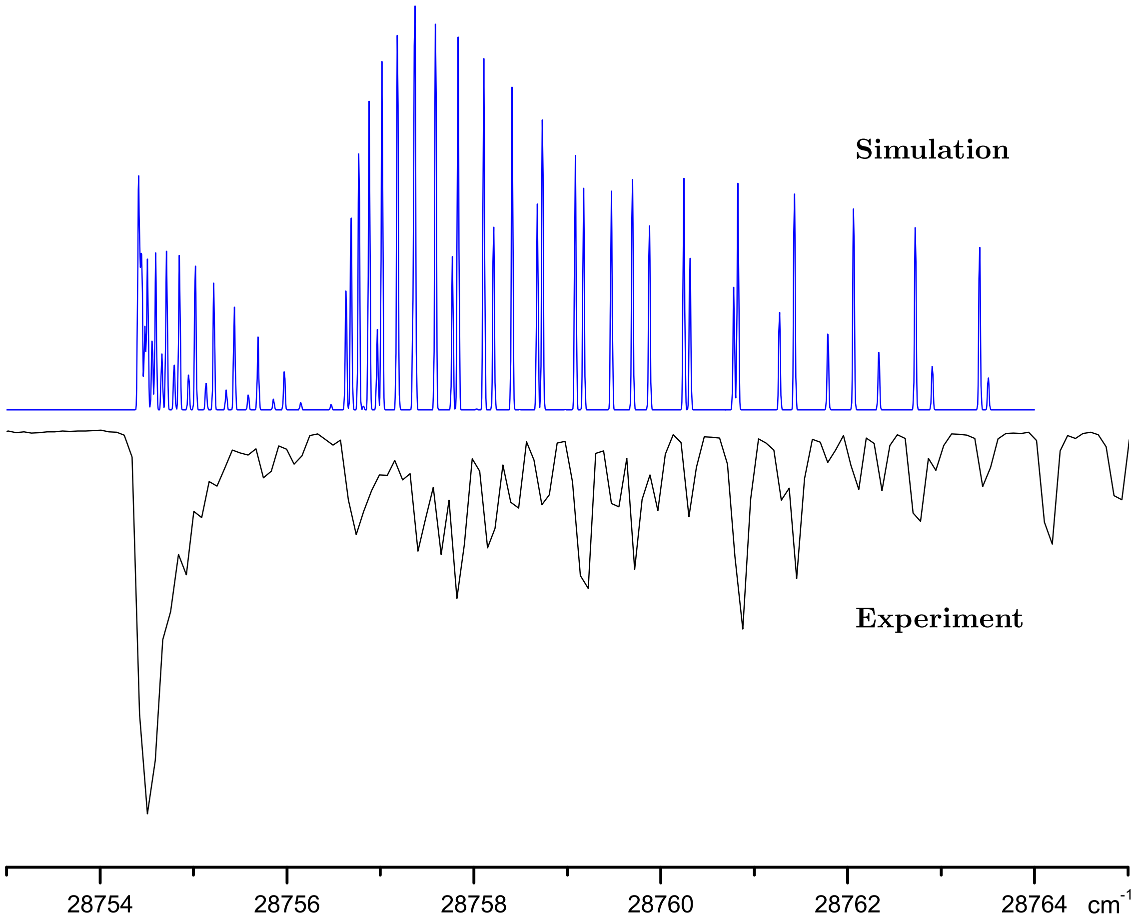

Figure A.2: Simulation with $0.016\,\mathrm{cm}^{-1}$ resolution of the origin band of the $A\ {}^1\Pi \leftarrow X\ {}^1\Sigma^+$ electronic transition for AlCCH.

Curriculum Vitae and list of publications

Name: Cristina Apetrei Birza
Born: October 5, 1978, Tg. Ocna, Romania
Nationality: Romanian
Contact: apetrei.cristina@gmail.com

EDUCATION

06/2005 – 09/2009	Ph.D. Student - Marie Curie Fellowship University of Basel, Switzerland, Chemistry Department *Thesis:* **Characterization of metal-carbon species a mass-selective multiphoton ionization technique** Supervisor: **John P. Maier**
03/2003 – 04/2005	Master Studies in Chemistry Transilvania University of Brasov, Romania Design and Management of Renewable Energy Systems *Master Thesis:* **Bioethanol production from biomass**
10/1997 – 02/2002	B. Sc. in Chemistry Transilvania University of Brasov, Romania *Diploma thesis:* **Stability studies and storage conditions of metabolites**

WORK EXPERIENCE

09/2004 – 05/2005	Chemist – Quality Assurance GlaxoSmithKline, Brasov, Romania
07/2002 - 09/2004	Chemist – Quality Control Waters Romania, subsidiary of Waters Corporation, Brasov, Romania
09/2001 - 12/2001	Analytical Chemist Kluyver Laboratory for Biotechnology, Netherlands

FELLOWSHIPS

2005-2008	Ph.D. Marie Curie Fellowship – Molecular Universe Research Training Network
02/2008 – 03/2008	Research stay – University of Arizona, Tucson and Arizona State University, Phoenix, USA
03/2001 – 09/2001	Socrates - Erasmus Scholarship – Kluyver Laboratory for Biotechnology, Delft, The Netherlands

ORAL PRESENTATIONS AND POSTERS

Oral presentations

2008	- Department Seminar – University of Utah, Salt-Lake City, USA
	- Marie Curie – Final Annual Network Meeting, Boppard, Germany
2007	- Marie Curie – 2nd year and Mid-Term Review Meeting, Perugia, Italy
2005	- Marie Curie – Annual Workshop, Leiden, Netherlands

Posters

2008	International Meeting on the Physics and Chemistry of the Interstellar Medium, Arcachon, France
	Latsis - Symposium “Intramolecular Dynamics, Symmetry and Spectroscopy”, ETH Zürich, Switzerland
2007	Molecular Universe 2nd year and Mid–Term Review Meeting, Perugia, Italy

PEER REVIEWED PUBLICATIONS

- **Gas phase electronic spectrum of T-shaped AlC_2 radical**, C. Apetrei, A. E. Knight, E. Chasovskih, E. B. Jochnowitz, H. Ding, and J.P. Maier, *Journal of Chemical Physics*, 2009, 131, 064305.

- **Gas phase $1^1\Sigma_u^+ \leftarrow {}^1\Sigma_g^+$ optical spectra of large polyacetylenes $HC_{2n}H$, n=5-7**, C. Apetrei, R. Nagarajan and J. P. Maier, *Journal of Physical Chemistry A*, 2009, **DOI:** 10.1021/jp902141n

- **Characterization of the X $^1A_1$ and A $^1B_2$ electronic states of titanium dioxide, TiO_2**, H. Wang and T. Steimle and C. Apetrei, J. P. Maier, *Physical Chemistry Chemical Physics*, 2009, 11(15),2649.

- **Electronic Spectra of $MgC_{2n}H$ (n = 1–3) Chains in the Gas Phase,** H. Ding, C. Apetrei, Ł. Chacaga, and J. P. Maier, *Astrophysical Journal, (*2008), 677.

- **Gas phase electronic spectrum of linear AlCCH,** C. Apetrei, H. Ding, J.P. Maier, *Physical Chemistry Chemical Physics* (2007), 9(29) – Cover article

- **Resonant two-photon ionization spectroscopy of BNB,** H. Ding, M. D. Morse, C. Apetrei, Ł. Chacaga, and J. P. Maier, *Journal of Chemical Physics* (2006), 125(19)

- **Quantitative analysis in nanoliter wells by prefilling of wells using electrospray deposition followed by sample introduction with a coverslip method.** R. Moerman, J. Knoll, C. Apetrei, L. R. Van den Doel, G. W. K Van Dedem, *Analytical Chemistry* (2005), 77(1)